Novel Photonic Band Gap Structures for Accelerator Applications

by

Evgenya I. Smirnova

M.S. Physics, Nizhny Novgorod State University, Russia, 2002

Submitted to the Department of Physics
in partial fulfillment of the requirements for the degree of

Doctor of Philosophy in Physics

at the

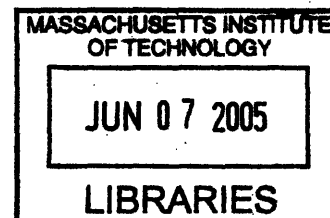MASSACHUSETTS INSTITUTE OF TECHNOLOGY

June 2005

© Evgenya I. Smirnova
M.S. Physics, Nizhny Novgorod State University, Russia, 2002, MMV.
All rights reserved.

The author hereby grants to MIT permission to reproduce and
distribute publicly paper and electronic copies of this thesis document
in whole or in part.

Author . . . .
- Department of Physics
February 23, 2005

Certified by . . . .
Richard J. Temkin
Senior Scientist, Department of Physics
Thesis Supervisor

Accepted by . . . . ,
Thomas J. Greytak
Professor, Associate Department Head for Education

Science

Novel Photonic Band Gap Structures for Accelerator Applications

by

Evgenya I. Smirnova

M.S. Physics, Nizhny Novgorod State University, Russia, 2002

Submitted to the Department of Physics
on February 23, 2005, in partial fulfillment of the
requirements for the degree of
Doctor of Philosophy in Physics

Abstract

In this thesis I present the design and experimental demonstration of the first photonic band gap (PBG) accelerator at 17.140 GHz. A photonic band gap structure is a one-, two- or three-dimensional periodic metallic and/or dielectric system (for example, of rods), which acts like a filter, reflecting rf fields in some frequency range and allowing rf fields at other frequencies to transmit through. Metal PBG structures are attractive for the Ku-band accelerators, because they can be employed to suppress wakefields. Wakefields are unwanted modes affecting the beam propagation or even destroying the beam. Suppression of wakefields is important. In this thesis, the theory of metallic PBG structures is explained and the Photonic Band Gap Structure Simulator (PBGSS) code is presented. PBGSS code was well benchmarked and the ways to benchmark the code are described. Next, the concept of a PBG resonator is introduced. PBG resonators were modelled with Ansoft HFSS code, and a single-mode PBG resonator was designed. The HFSS design of a travelling-wave multi-cell PBG structure was performed. The multi-cell structure was built, cold-tested and tuned. Finally, the hot-test PBG accelerator demonstration was performed at the accelerator laboratory. The PBG accelerating structure was installed inside a vacuum chamber on the Haimson Research Corporation (HRC) accelerator beam line and powered with 2 MW from the HRC klystron. The electron bunches were produced by the HRC accelerator. The electron beam was accelerated by 1.4 MeV inside the PBG structure.

Thesis Supervisor: Richard J. Temkin
Title: Senior Scientist, Department of Physics

Acknowledgments

Contents

List of Figures

9

11

12

13

14

List of Tables

Chapter 1

Introduction

1.1 Photonic band gap structures

A *Photonic band gap* (PBG) structure [1, 2] or simply, photonic crystal, represents a periodic lattice of macroscopic pieces (for example, rods) of dielectric or metal. Photonic band gap structures can be one-, two- or three-dimensional (see examples in figure 1-1). A good example of a one-dimensional (1D) PBG structure is a well-known in optics Bragg filter [3], which is a periodic system of dielectric plates. Two-dimensional (2D) PBG structures, namely systems of rods, were found to be the most attractive for accelerator applications. Two types of 2D lattices are the most common: square lattice and triangular lattice (figure 1-2). Scattering of the electromagnetic waves at the interfaces of a periodic structure can produce many of the same phenomena for photons (light modes) as the atomic potential does for the electrons. In particular, one can design and construct photonic crystals with photonic band gaps, preventing light of certain frequencies from propagating in certain directions. For example, the dependence of the reflection coefficient on the wave's frequency for an electromagnetic wave incident on a Bragg filter is shown in figure 1-3. The wave is totally reflected not just for a single frequency but in whole frequency bands. This property allows optical scientists to control incident waves and filter unwanted frequencies. The range of frequencies which does not propagate through the periodic structure is called a *band gap*.
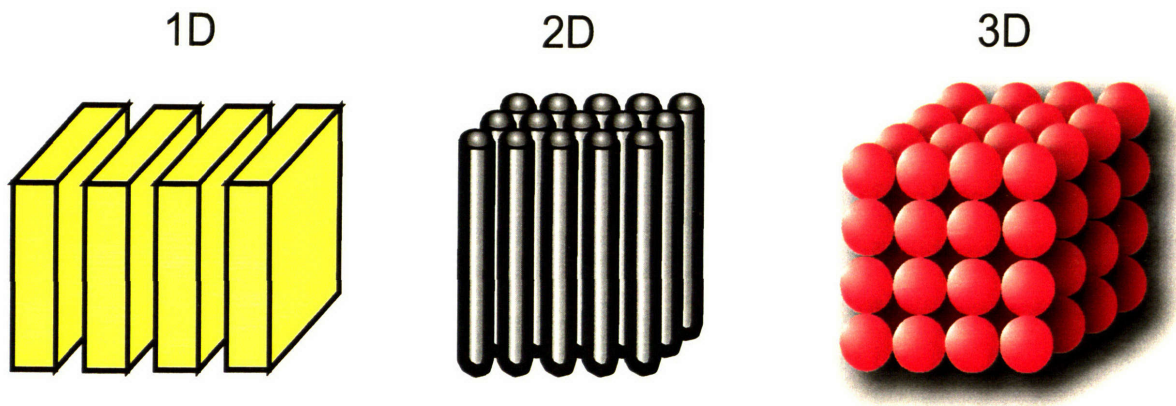
Figure 1-1: Examples of one-, two- and three-dimensional photonic band gap structures.

Similar phenomena are observed in more complicated two- and three-dimensional (3D) periodic structures. The waves of some frequencies cannot propagate and are reflected. Moreover, some frequencies are reflected independently of the angle of incidence. The bands of frequencies reflected independently of the angle of incidence are called *global band gaps*. The phenomena of global band gap can afford us a complete control over the electromagnetic waves propagation in PBG media. In accelerator physics, the photonic band gap resonators can be employed to achieve the mode selectivity. A simple PBG resonator schematic is shown in figure 1-4. The metal rods form a triangular lattice. A single rod is withdrawn from the lattice at the center. The wave with a frequency inside the band gap will be reflected from a "PBG wall" and a mode can be confined around the defect. An example of such a mode is shown in figure 1-5. However only the modes with the frequencies inside the band gaps can be confined in a PBG resonator.

1.2   Microwave linear accelerators and wakefields

In microwave accelerators, energy is delivered to the beam from an radio-frequency (rf) electric field. The accelerating mode is characterized by a longitudinal electric field on beam axis. An example of a resonator mode with the longitudinal electric
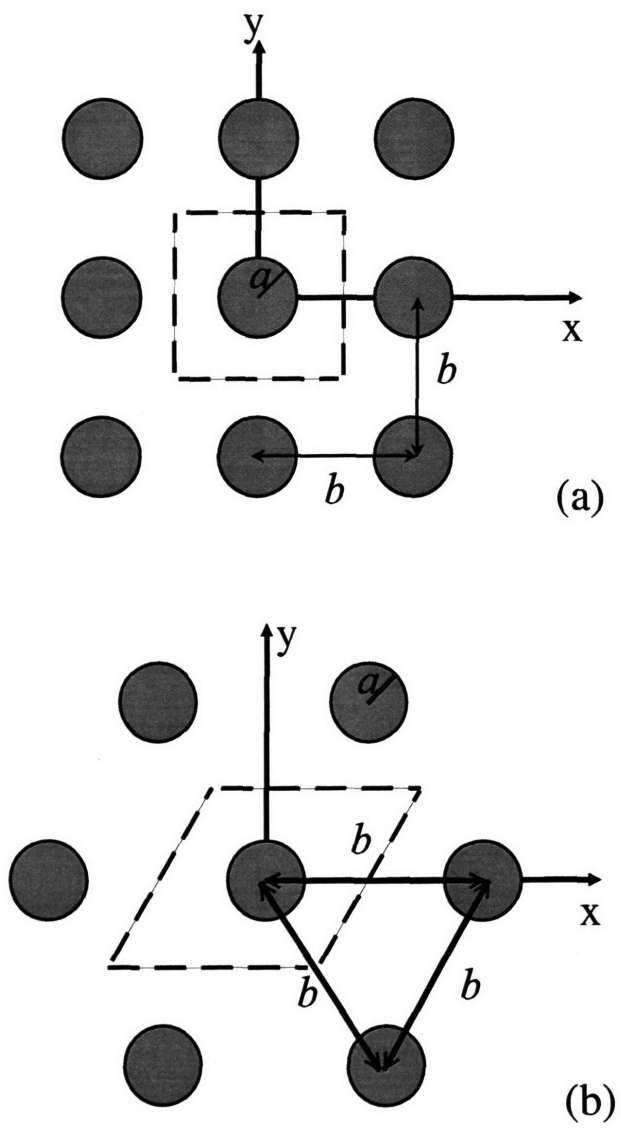
Figure 1-2: Two types of two-dimensional lattices of metal rods: (a) square lattice, (b) triangular lattice.
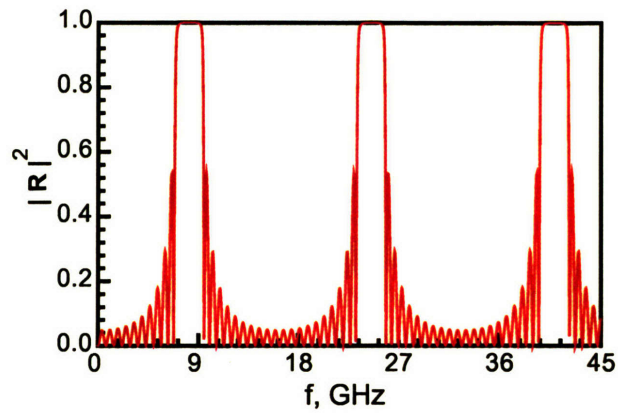
Figure 1-3: The reflection from a Bragg filter as a function of wave frequency. The wave is incident perpendicular to the plates.
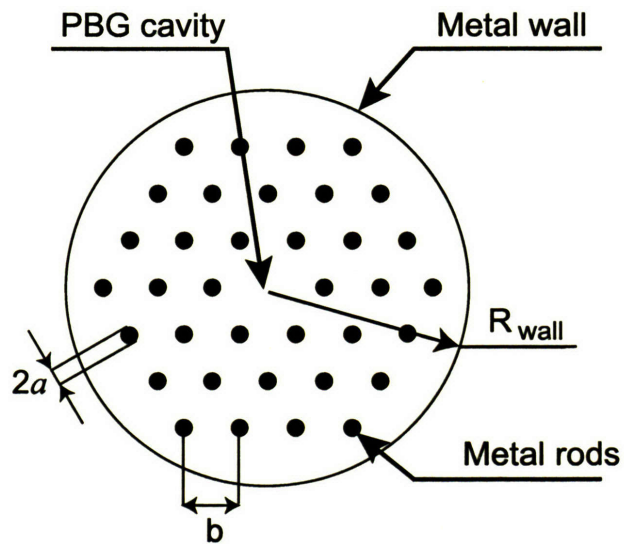
Figure 1-4: The schematic of a 2D PBG resonator.
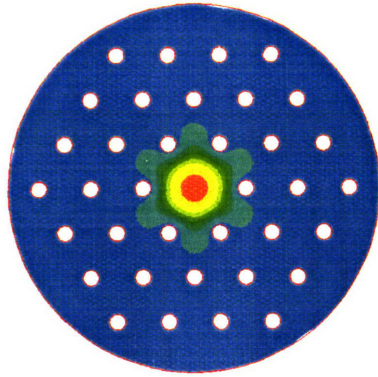
Figure 1-5: Electric field pattern of a mode confined in a PBG resonator.

field is the TM_{01} (transverse-magnetic) mode. The field profile in the TM_{01} mode is shown in figure 1-6. The linac uses a sinusoidally varying electric field for acceleration, which must be synchronous with the beam for sustained energy transfer. This is the reason why a uniform cylindrical waveguide cannot provide continuous acceleration of electrons: the phase velocity of an electromagnetic wave in a uniform waveguide always exceeds the velocity of light, so the synchronism with the beam is not possible. A structure with more complicated geometry is required to lower the phase velocity to that of the beam. It was proposed to construct a linac structure of an array of cylindrical cavities of figure 1-6 with axial beam holes. It can be shown that for this so-called disk-loaded waveguide structure the phase velocity can be reduced below the speed of light as required for particle acceleration. The schematic of a disk-loaded waveguide is shown in figure 1-7.

Acceleration in disk-loaded waveguides works well. However due to the electro-magnetic interaction of electron bunches with periodic structure new problems arise. The beam starts to radiate and produce wakefields. These wakefields are unwanted modes, they give rise to a parasitic energy loss and energy spread in the bunch and introduce transverse forces that tend to increase the effective beam emittance [4]. The problem of wakefields was first recognized in Stanford Linear Collider (SLC) [5] and became a serious issue for the Next Linear Collider (NLC) [6]. It appears that if we

Figure 3-2: Illustration of the near- and far-field regions in the quasistatic approximation.

$f(\vec{x}_\perp)$ can be self-consistently related to the wave function $\psi(\vec{x}_\perp)$.

Assume that the center of the rod (m, n) is located at $\vec{x}_\perp = \vec{T}_{m,n}$. We introduce the notation $\vec{r} = \vec{x}_\perp - \vec{T}_{m,n}$. There are two regions surrounding the rod (m, n), where the behavior of $\psi^{(m,n)}(\vec{x}_\perp)$ is qualitatively different [23]: *near-field* region and *far-field* region, as shown in figure 3-2. In the *near-field* region where $\kappa r \ll 1$, the wave function $\psi^{(m,n)}$ changes rapidly, i.e.,

$$\left| \vec{\nabla}^2 \psi_{near}^{(m,n)} \right| \sim \psi_{near}^{(m,n)}/a^2 \gg \kappa^2 \psi_{near}^{(m,n)}. \tag{3.8}$$

In the far-field region where $\kappa r \gtrsim 1$, the wave-function $\psi^{(m,n)}$ changes slowly, i.e.,

$$\left| \vec{\nabla}^2 \psi_{far}^{(m,n)} \right| \sim \kappa^2 \psi_{far}^{(m,n)}. \tag{3.9}$$

The near- and the far-field solutions must match at the boundary of the two regions,

$$\left. \psi_{near}^{(m,n)} \right|_{r \sim 1/\kappa} \sim \left. \psi_{far}^{(m,n)} \right|_{r \sim 1/\kappa}. \tag{3.10}$$

In the remainder of this section, we use the near- and the far-field solutions to derive approximate self-consistent expressions for the sources $f(\vec{x}_\perp)$ and solve the system of Eqs. (3.6). We now consider the TM and TE modes separately.

want to contemplate seriously the design of any future collider, we need to understand the nature of wakefields and find the ways to suppress them efficiently.

1.3 Motivation of the photonic band gap research for accelerators

For many years accelerator facilities with colliding beams have been the forefront instruments used to study elementary particle physics at high energies. Both hadron-hadron and electron-positron colliders have been used to make important observations and discoveries. The Stanford Linear Collider was conceived and built to study particle physics at the 100 GeV energy scale and to develop the accelerator physics and technology necessary for the realization of future high-energy colliders. The next generation of colliders must open the frontier from multi-hundred GeV to TeV energies - ten times that of the present generation. More powerful collider facilities will be required to fully explore this new territory. It is very attractive for accelerator engineers to improve the energy efficiency of future linear accelerators via increasing the accelerator frequency and going from an S-band (SLC, 2.856 GHz) to an X-band (NLC, 11.424 GHz) accelerator. To obtain high-efficiency acceleration and high luminosity of the beam, new accelerating cavities must be invented which will be selective with respect to the operating mode, and will suppress wakefields. PBG structures provide us with a simple design of an accelerator cavity that would selectively support the accelerating TM_{01} mode. Other modes (with different frequencies) will not be supported and this way the wakefields are efficiently damped. Compared to such complicated damped-detuned structures as [7], PBG structures may be easier to design and manufacture. The demonstration of a PBG accelerator is necessary.

1.4 Advances in photonic band gap research

First advances in photonic band gap research date back to 1987 when the pioneering paper of Yablonovitch [1] was published. The intensive PBG structure research origi-

nated in studying of dielectric lattices [2, 8, 9]. The dispersion properties of 2D lattices of dielectric rods were studied and the global photonic band gaps were determined. The handbooks on the lattices made of the most popular dielectric materials were published. However, considerable interest in metallic PBG structures has been expressed due to their applications at microwaves [10, 11, 12]. For studies of wave propagation in the bulk of metallic PBG structures, the plane wave expansion method [13] generalized Rayleigh expansion method [14], finite-difference time-domain scheme [15] and the coordinate-space finite-difference method [10] have been used. An attempt to study global photonic band gaps in metallic lattices was made in [14]. However, it was discovered [13] that due to a convergence problem, the plane wave expansion method is applicable only to the lattices with the size of conductors small compared to the lattice period. At microwave frequencies the lattices with a large ratio of rod radius to the lattice constant are of the main interest [10, 11, 12]. So the elaboration of the coordinate-space finite-difference calculations was necessary. Only the first-order band gap of a square lattice of metallic rods was calculated in [14]. More extensive computations of band gaps were needed.

Dielectric PBG resonators were extensively studied in [16]. An idea to construct a dielectric and later a metallic PBG resonator and use it as an accelerator cell originated with the authors of Refs.[17, 10]. Dispersion properties of a square lattice of alumina ceramics and metal rods were studied in [17, 10]. PBG resonators were modelled and the accelerating mode was discovered. Single mode confinement was not proven. However the wakefields excitation was modelled and the wakefield spectrum was found rare compared to pillbox resonators [18]. Single-cell superconductive PBG resonators were constructed and successfully cold-tested [19]. In spite of the impressive work performed by the authors of [19, 10, 17, 18] there are certain drawbacks in their research. First, they focused on studying and manufacturing the resonators based on the square lattice of rods. Square lattice has quadrupole symmetry. We have shown that it introduces a significant transverse energy gradient in the beam. We proposed to use the triangular lattice [11], which has a higher sextuple symmetry and provides acceptable transverse uniformity in the accelerator.

Second, the complete band gap picture for the square lattice of metal rods was never derived in [19, 10, 17, 18], therefore the authors were unable to prove a single-mode confinement in their PBG resonators. Third, a real multi-cell PBG accelerator was never constructed and the acceleration in PBG structures was never demonstrated. The biggest achievement of the research of [19, 10, 17, 18] is the construction of a superconductive PBG cell at 2.858 GHz. The construction of PBG resonators at this low frequency is mechanically easy and the demonstration of a superconductive PBG accelerator is important, since the wakefields present a serious issue for the superconductive accelerators.

1.5 Thesis outline

The PBG accelerator design and testing presented in this thesis can be logically divided into several steps. First, metallic 2D PBG structures must be studied and the global band gap diagrams must be derived. Next, based on the global band gap diagrams a single-mode PBG resonator must be designed, fabricated and tested. The higher-order modes (HOM) suppression must be experimentally demonstrated. Finally, a disk-loaded PBG waveguide structure must be designed, built, tuned and tested.

The theory of metal PBG structures and computation of band gaps is presented in Chapter 2 of this thesis. The Photonic Band Gap Structure Simulator (PBGSS) code was developed by this author for computing of global band gaps. Chapter 3 deals with the theoretical benchmarking of the PBGSS code. Chapter 4 describes the design of a single-mode PBG resonator and the cold-tests demonstrating the HOM suppression. In Chapter 5 the design of a disk-loaded PBG accelerator is presented and extensive computer simulations leading to the design are described. Chapter 6 explains the fabrication and cold-testing of a PBG accelerator: the tuning algorithms and the results. In Chapter 7 the hot test demonstration of the PBG accelerator is described. In Chapter 8, the conclusion, I will discuss the possible improvements to the PBG accelerator design and additional tests needed to demonstrate that a PBG

accelerator is a serious candidate for the future high-energy collider structure.

Chapter 2

Numerical simulation of dispersion properties of PBG structures

2.1 Introduction

In this Chapter I will address an important and computationally challenging problem of computation of the global photonic band gaps in 2D metallic PBG structures. First, I will describe the general theory of 2D metallic PBG structures representing square and triangular lattices of metal rods. Then, I will introduce a coordinate-space finite-difference code called Photonic Band Gap Structure Simulator (PBGSS). The PBGSS code was developed by this author and was specially aimed at calculation of the global band gaps. First, Brillouin diagrams for the TM and the TE waves in square and triangular lattices were calculated. Next, an extensive calculation was performed to calculate the global band gaps for the lattices with different radii of the rods. Examples of Brillouin diagrams and computed global band gap diagrams are presented in the thesis. The operating frequencies of pre-existing PBG resonators [11, 12] are plotted over the newly computed band gap pictures.

2.2 Formulation of the Eigenvalue Problem

Two types of lattices of metal rods are considered in this thesis, namely the square lattice (figure 1-2(a)) and the triangular lattice (figure 1-2 (b)).

The conductivity profile in the system of a 2D periodic array of metal rods satisfies the periodic condition

$$\sigma \left(\vec{x}_\perp + \vec{T}_{mn} \right) = \sigma \left(\vec{x}_\perp \right) \tag{2.1}$$

with the set of periodicity vectors defined as

$$\vec{T}_{mn} = \begin{cases} mb\hat{e}_x + nb\hat{e}_y, & \text{square lattice} \\ \\ \left(m + \frac{n}{2} \right) b\hat{e}_x + \frac{\sqrt{3}}{2}nb\hat{e}_y, & \text{triangular lattice} \end{cases}, \tag{2.2}$$

where $\vec{x}_\perp = x\hat{e}_x + y\hat{e}_y$ is the transverse coordinate, b is the lattice spacing, m and n and are integers.

It is readily shown from Maxwell's equations that the wave field in the two-dimensional PBG structures can be decomposed into two independent classes of modes: the transverse electric (TE) modes and the transverse magnetic (TM) modes. In a TE mode the electric field vector is perpendicular to the rod axis and in a TM mode the magnetic field vector is perpendicular to the rod axis. All the field components in the TM (TE) modes can be expressed through the axial component of the electric (magnetic) field, which we will further denote by ψ. Since the system is homogeneous along the z-axis, we can Fourier transform ψ in axial coordinate z and time t and consider

$$\psi \left(\vec{x}_\perp, k_z, \omega \right) = \iint \psi \left(\vec{x}_\perp, z, t \right) e^{i(k_z z - \omega t)} dz dt, \tag{2.3}$$

which we will denote hereafter by $\psi \left(\vec{x}_\perp \right)$ assuming that the frequency and the longitudinal wave number are fixed. The Helmholtz equation for $\psi \left(\vec{x}_\perp \right)$ follows from Maxwell's equations,

$$\vec{\nabla}_\perp^2 \psi \left(\vec{x}_\perp \right) = \left(k_z^2 - \frac{\omega^2}{c^2} \right) \psi \left(\vec{x}_\perp \right). \tag{2.4}$$

27

The boundary conditions on the surfaces S of the conducting posts are

$$\psi|_S = 0, \quad \text{(TM mode)}, \tag{2.5}$$

$$\left.\frac{\partial \psi}{\partial \vec{n}}\right|_S = 0, \quad \text{(TE mode)}, \tag{2.6}$$

where $\vec{n}$ is the normal vector to the post surface.

The discrete translational symmetry of the conductivity profile allows us to write the fundamental solution of the Helmholtz equation in the Bloch form,

$$\psi\left(\vec{x}_\perp + \vec{T}\right) = \psi\left(\vec{x}_\perp\right) e^{i\vec{k}_\perp \cdot \vec{T}}, \tag{2.7}$$

where $\vec{T}$ is any vector of $\vec{T}_{mn}$, $\vec{k}_\perp = k_x \hat{e}_x + k_y \hat{e}_y$ is an arbitrary transverse wave number. Thus we need only solve Eq. (2.4) inside the fundamental unit cell defined by

$$|x| \leq b/2, \quad |y| \leq b/2, \quad \text{(square lattice)},$$
$$\tag{2.8}$$
$$\left|x - \frac{y}{\sqrt{3}}\right| \leq b/2, \quad |y| \leq \frac{\sqrt{3}}{4}b, \quad \text{(triangular lattice)}.$$

The following periodic boundary conditions are deduced from Eq. (2.7)

$$\begin{cases} \psi\left(\frac{b}{2}, y\right) = e^{ik_x b}\psi\left(-\frac{b}{2}, y\right) \\ \\ \psi\left(x, \frac{b}{2}\right) = e^{ik_y b}\psi\left(x, -\frac{b}{2}\right) \end{cases}, \quad \text{(square lattice)}, \tag{2.9}$$

$$\begin{cases} \psi\left(\frac{b}{2} + \frac{\sqrt{3}}{3}y, y\right) = e^{ik_x b}\psi\left(-\frac{b}{2} + \frac{\sqrt{3}}{3}y, y\right) \\ \\ \psi\left(x, \frac{\sqrt{3}b}{4}\right) = e^{ik_x b/2 + ik_y\sqrt{3}b/2}\psi\left(x - \frac{b}{2}, -\frac{\sqrt{3}b}{4}\right) \end{cases}, \quad \text{(triangular lattice)}. \tag{2.10}$$

Equation (2.4) together with boundary conditions (2.5) or (2.6) and (2.9) or (2.10) define the eigenvalue problem of finding $\kappa^2 = \omega^2/c^2 - k_z^2$ for each given perpendicular wave vector $\vec{k}_\perp$.
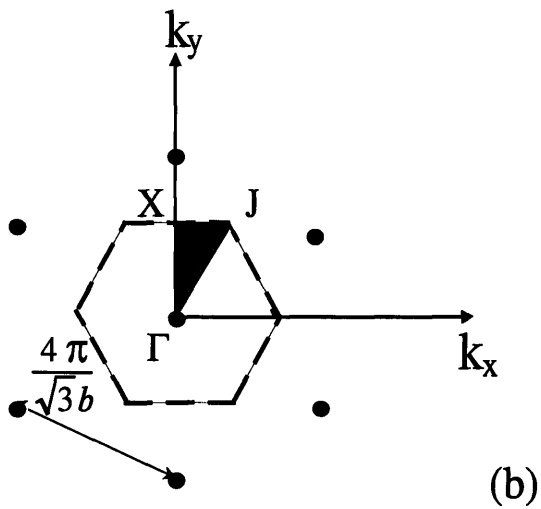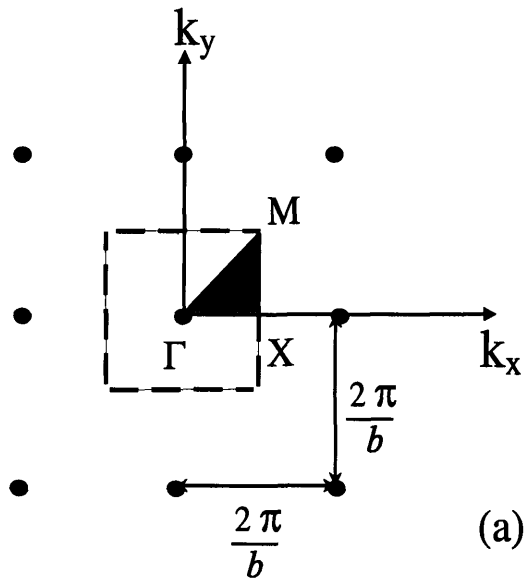
Figure 2-1: Reciprocal lattices and Brillouin zones for (a) square lattice and (b) triangular lattice (irreducible Brillouin zones for each type of lattice are shaded).

The periodicity of the exponent in Eq. (2.7) means that the possible values $\vec{k}_\perp$ can be restricted to the irreducible Brillouin zones of the reciprocal lattices, which for the cases of square and triangular lattices are illustrated in figure 2-1. The three special points in figure 2-1(a) Γ , X and M correspond respectively to $\vec{k}_\perp = 0$, $\vec{k}_\perp = (\pi/b)\, \vec{e}_x$ and $\vec{k}_\perp = (\pi/b)\,(\hat{e}_x + \hat{e}_y)$. The three special points in figure 2-1(b) Γ, X and J correspond to $\vec{k}_\perp = 0$, $\vec{k}_\perp = (2\pi/\sqrt{3}b)\, \hat{e}_x$ and $\vec{k}_\perp = (2\pi/3b)\,(\hat{e}_x + \sqrt{3}\hat{e}_y)$.

2.3 Numerical Scheme of the Eigenvalue Computation

To compute the eigenmodes for rf wave propagation in the two-dimensional PBG structures, we have developed the PBGSS code [20]. The PBGSS code is based on a real-space finite difference method. We cover the fundamental unit cell of the square (triangular) lattice by square (triangular) mesh with $(2N + 1) \times (2N + 1)$ mesh points. Outside the conducting posts, the Helmholtz equation (2.4) is approximated by a set of linear relations between the values $\psi_{i,j}$ of the function $\psi(\vec{x}_\perp)$ at the point (i,j) of the mesh (the mesh point $i = j = 0$ corresponds to the origin of the fundamental cell). We will refer to the equation

$$\psi_{i+1,j} + \psi_{i-1,j} + \psi_{i,j+1} + \psi_{i,j-1} - 4\psi_{i,j} = -\kappa^2 h^2 \psi_{i,j} \tag{2.11}$$

for the square lattice, and

$$4\left(\psi_{i+1,j} + \psi_{i-1,j} + \psi_{i,j+1} + \psi_{i,j-1}\right)$$
$$- \left(\psi_{i+1,j+1} - \psi_{i+1,j-1} - \psi_{i-1,j+1} + \psi_{i-1,j-1}\right) - 16\psi_{i,j} = -3\kappa^2 h^2 \psi_{i,j} \tag{2.12}$$

for the triangular lattice, as "equation (i, j)". Here, $h = b/(2N + 1)$ is the mesh step. The periodic boundary conditions (2.9) and (2.10) are expressed explicitly as

$$\begin{cases} \psi_{N+1,j} = e^{ik_x b}\psi_{-N,j} \\ \\ \psi_{i,N+1} = e^{ik_y b}\psi_{i,-N} \end{cases} \text{, (square lattice),} \qquad (2.13)$$

$$\begin{cases} \psi_{N+1,j} = e^{ik_x b}\psi_{-N,j} \\ \\ \psi_{i,N+1} = e^{ik_x b/2 + ik_y \sqrt{3}b/2}\psi_{i,-N} \end{cases} \text{, (triangular lattice).} \qquad (2.14)$$

The mesh points, which fall inside the conducting posts, are excluded from the system of linear equations (2.11) or (2.12) by using boundary conditions (2.5) or (2.6). The boundary condition (2.5) is implemented by setting the value of $\psi_{i,j} = 0$ for the grid point (i, j) inside of the conducting cylinder. The boundary condition (2.6) is implemented in the following way: if some point entering the linear equation (i, j) falls inside the post we put the value of ψ in this point equal to $\psi_{i,j}$. We have chosen the simplest implementation of the boundary conditions in Eq. (2.6) in order to preserve the Hermitian nature of the matrix of linear equations (2.11) or (2.12). Since we do not take into account the losses in electrodynamic system, the initial eigenvalue problem is Hermitian, and we have found empirically that the preservation of the Hermitian nature improved the convergence of the algorithm. Thus we obtain a closed set of $(2N + 1)^2 - M$ linear equations, where M is the number of the mesh points that fall inside the conducting cylinder. The matrix of this system is Hermitian and we compute its eigenvalues κ using a standard Fortran subroutine.

2.4 Results of eigenmodes and band gaps calculations

In this section, the results of the PBGSS calculations of the eigenfrequencies for the TE and the TM modes in the two-dimensional square and triangular lattices are

31

presented. For all the plots we set $k_z = 0$, i.e., $\kappa = \omega/c$, which obviously does not affect the generality of the results. In all the PBGSS calculations, we use the value of $N = 20$. Our experience shows that the results are nearly identical as N is further increased.

2.4.1   The TM modes

Figure 2-2 shows the dispersion characteristics (Brillouin diagrams) for the TM modes as the wave vector $\vec{k}_\perp$ varies from the center of the Brillouin zone (Γ point in figure 2-1), to the nearest edge of the Brillouin zone (X point in figure 2-1), and to the far edge of the Brillouin zone (M point for the square lattice and J point for the triangular lattice). Two cases correspond to different types of lattices. In figure 2-2, $a/b = 0.2$ and for the square lattice a global band gap between the first and second modes can be seen. For the triangular lattice the first and the second mode are intersecting and there is no band gap between them. For the TM modes, there is a cut-off frequency that is the zeroth-order band gap.

To determine the global TM band gaps, we perform more extensive computations. It is important to perform simulations with small grid step to assure the accuracy of the simulation results. For each value of a/b, we search through all $\vec{k}_\perp$ on the boundary of the Brillouin zone and find the minimum and maximum of each dispersion curve. Then we check if there is a gap between any two adjacent modes, i.e., if the minimum of the higher order mode is above the maximum of the lower order mode. The results are shown in figure 2-3. Shown in figure 2-3(a) are the five lowest-order global TM band gaps for the square lattice. The zeroth-order global TM band gap exists below the first mode, that is, there is a cutoff frequency for the TM modes. The cutoff frequency exists even for very small conducting cylinders and goes to zero logarithmically as $a/b \rightarrow 0$ (which is illustrated in figure 2-3 with a dashed curve continuation of the calculated cutoff curve). The first-order global TM band gap occurs between the first and second lowest modes. There is a threshold for first-order global TM band gap opening at $a/b \cong 0.1$. Higher-order global TM band gaps occur between the third and fourth, fourth and fifth, and fifth and sixth modes. There is
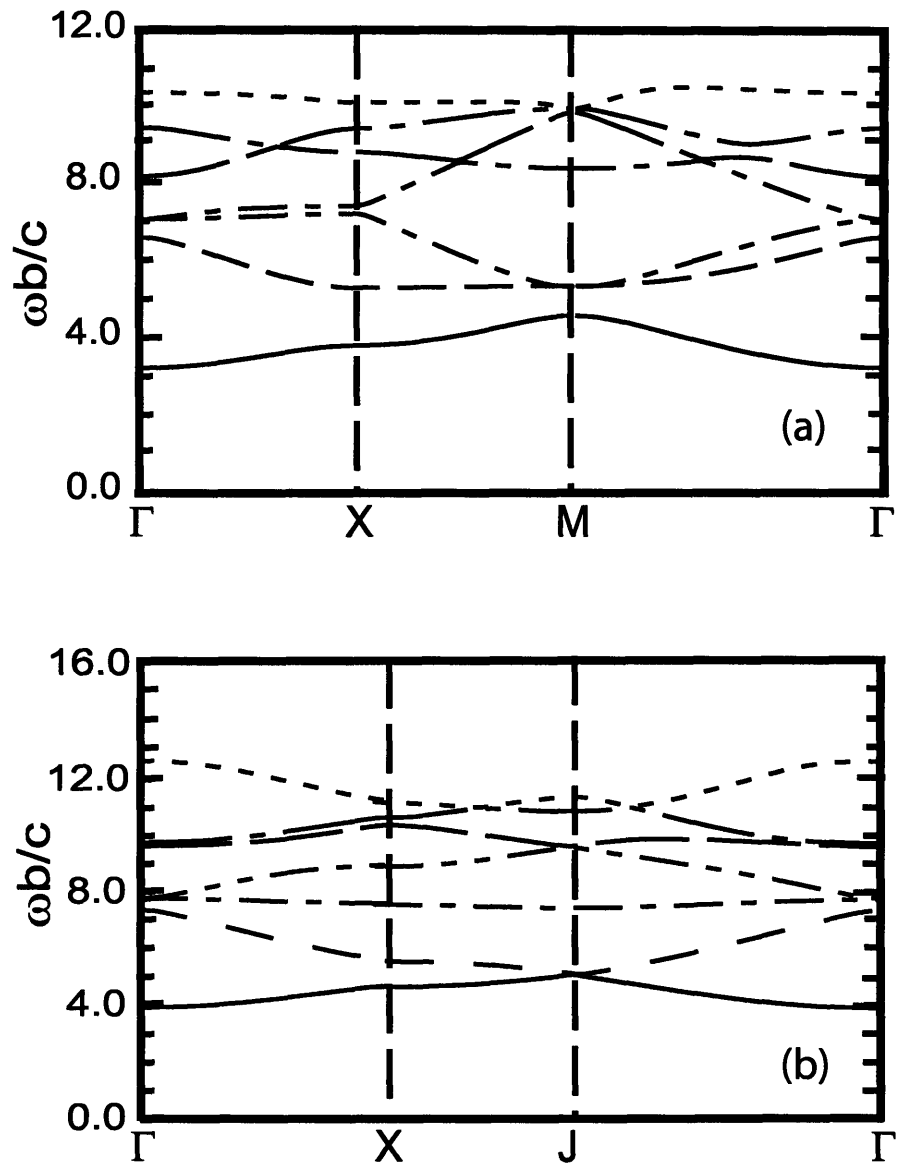
Figure 2-2: Plot of the several lowest normalized eigenmodes versus the wave vector $\vec{k}_\perp$ for the TM modes as $\vec{k}_\perp$ varies from the center of the Brillouin zone (Γ point in figure 2-1), to the nearest edge of the Brillouin zone (X point in figure 2-1), and to the far edge of the Brillouin zone (M or J point). Here $a/b = 0.2$ and two cases correspond to (a) square lattice and (b) triangular lattice.
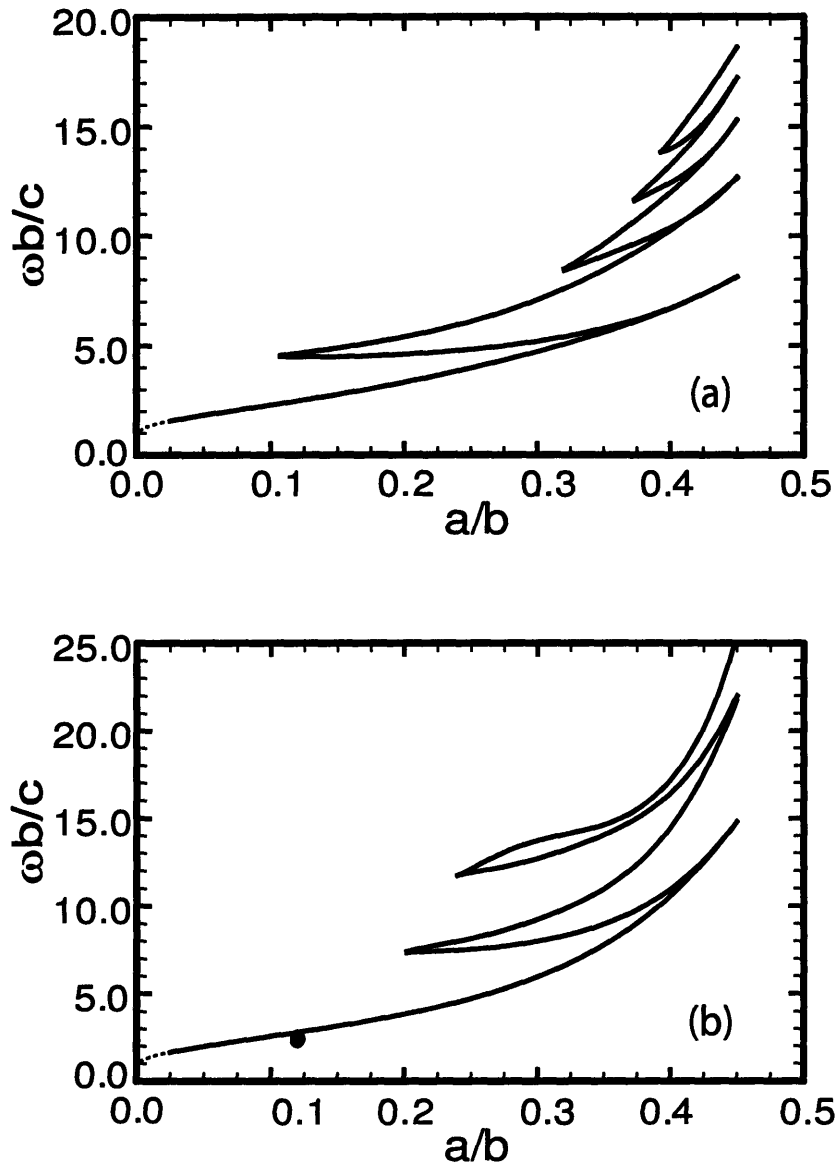
Figure 2-3: Plots of global band gaps for the TM mode as functions of a/b as obtained from PBGSS calculations for (a) square lattice and (b) triangular lattice. The solid dot represents the operating point of the 17 GHz MIT accelerator cavity.

no global band gap between the second and third modes.

Shown in figure 2-3(b) there are three lowest-order global TM band gaps for the triangular lattice. In figure 2-3(b), the zeroth-order global TM band gap exists below the first mode, which is similar to the case of the square lattice. Though there is a local band gap at X point between the first and second modes, these modes are intersecting at J point and the global band gap does not occur between them. The threshold for the occurrence of the first-order global TM band gap, which is between the second and third modes, is $a/b \cong 0.2$ The second-order global TM band gap occurs between the sixth and seventh modes. We find that the width of each global TM band gap increases as the ratio a/b increases. The solid dot in this figure represents the operating point of the 17 GHz MIT accelerator cavity (see [11]).

2.4.2   The TE modes

Figure 2-4 shows the Brillouin diagrams for the TE modes as the wave vector $\vec{k}_\perp$ varies from the center of the Brillouin zone (Γ point in figure 2-1), to the nearest edge of the Brillouin zone (X point in figure 2-1), and to the far edge of the Brillouin zone (M point for the square lattice and J point for the triangular lattice). Two cases correspond to the square and triangular lattices. In figure 2-4 $a/b = 0.2$, and there are no global TE band gaps for either square or triangular lattices. This is different from the TM case where the first band gap occurs between the first and second modes for $a/b \geq 0.1$. In contrast to the TM mode, there is no cutoff in the case of a TE mode. The first mode goes to zero at the Γ point for both square and triangular lattices. The first mode at the Γ point degenerates into the electrostatic solution (with zero frequency), which satisfies the boundary conditions (2.6).

We have also calculated the global TE band gaps in both types of lattices. The results are shown in figure 2-5. For the square lattice (figure 2-5(a)), we found that the first global TE band gap occurs when $a/b > 0.3$. This is the band gap between the first and second modes, which are tangent at the M point for lower ratios of a/b. Unlike the first global TM band gap, the lower boundary of this band gap decreases with increasing a/b. The higher order band gap opens and then closes for even lower

35
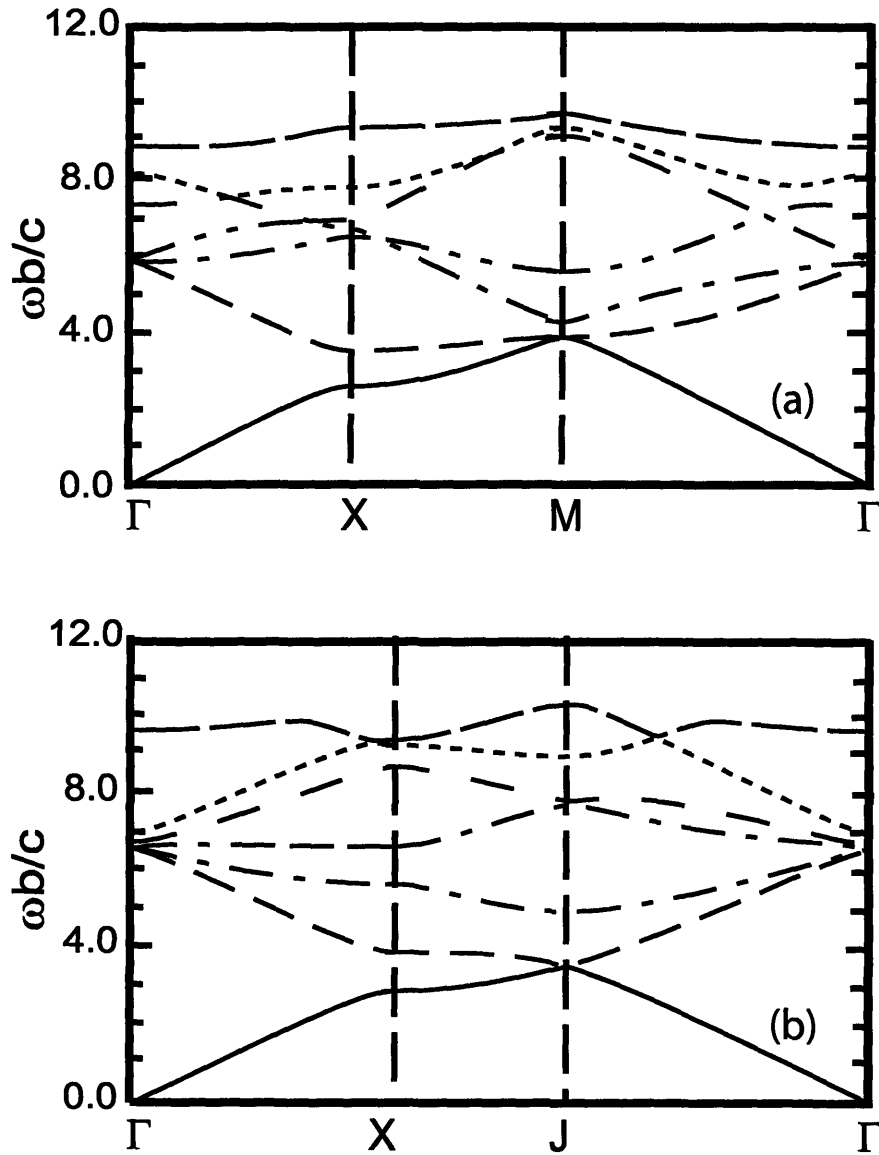
Figure 2-4: Plots of the several lowest normalized eigenmodes versus the wave vector $\vec{k}_\perp$ for the TE modes as $\vec{k}_\perp$ varies from the center of the Brillouin zone (Γ point in figure 2-1), to the nearest edge of the Brillouin zone (X point in figure 2-1), and to the far edge of the Brillouin zone (M or J point). Here $a/b = 0.2$ and two cases correspond to (a) square lattice and (b) triangular lattice.
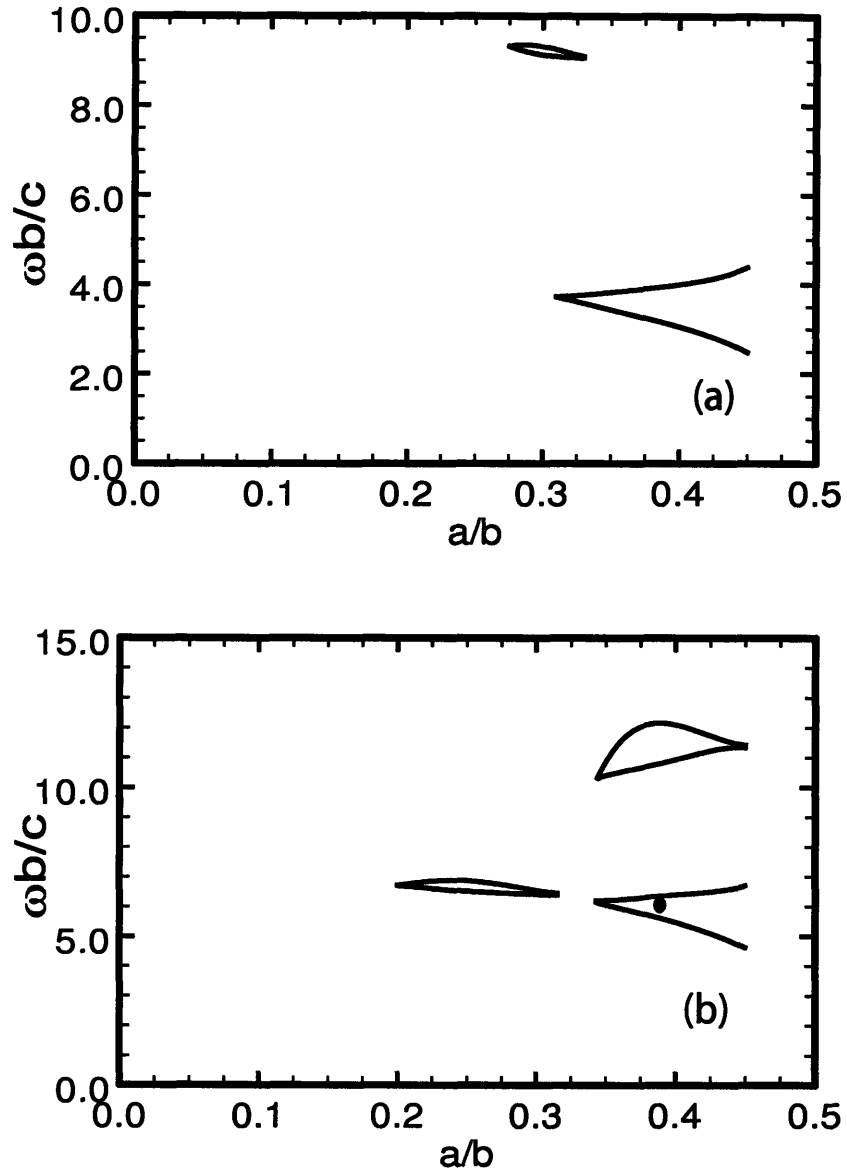
Figure 2-5: Plots of global band gaps for the TE mode as functions of a/b as obtained from PBGSS calculations for (a) square lattice and (b) triangular lattice. The solid dot represents the operating point of the 140 GHz MIT gyrotron cavity.

ratio of a/b, this gap is between the sixth and the seventh modes.

For the triangular lattice three lowest global TE band gaps are shown in figure 2-5(b). All of these gaps tend to close with increasing a/b except for the lowest one, which occurs between the second and third modes for $a/b > 0.35$. The second global TE band gap, which is between the third and fourth modes, appears for lower ratios of a/b than those for the lowest global TE band gap. The third global TE band gap is between the sixth and seventh modes. The solid dot in this figure represents the operating point of the 140 GHz MIT gyrotron cavity (see [12]).

The global TE band gaps in the metallic lattice resemble qualitatively the previously reported global TE and TM band gaps in dielectric lattices [8, 2], which typically close with increasing a/b. But there are two striking differences between the metal band gaps and dielectric band gaps. First, there is a zeroth-order global TM band gap in metallic lattices, which is a cutoff analogous to that in a conventional waveguide and exists for all values of a/b, whereas there is no such cutoff in dielectric lattices for either TE or TM modes. Second, the width of the global TM band gap in the metallic lattice increases with increasing a/b, whereas the global TE and TM band gaps in dielectric lattices typically close as the ratio a/b increases.

Chapter 3

Asymptotic analysis of dispersion characteristics in metallic PBG structures

3.1 Introduction

The PBGSS code [20] calculates the Brillouin diagrams and global band gaps in 2D metal PBG structures. It is important to ensure the validity of the PBGSS calculations, because the whole design of the PBG resonators in the following chapters relies on the PBGSS results. That is why we developed an asymptotic analysis, which allows us to derive the Brillouin diagrams theoretically in quasistatic limit, benchmarks the PBGSS code and also improves our understanding of the physics. The asymptotic analysis of the TM and TE modes propagating in square and triangular lattices of metal rods is presented in this chapter. The limit is considered when the rod radius, a, is much smaller than the wavelength, λ, and the distance between the rods, b (quasistatic limit). In this approximation, we can separate two regions in the 2D lattice with the qualitatively different behavior of electromagnetic waves. The near-field region is the one that immediately surrounds the rod. In this region the field changes at the scale of the rod radius and we can apply an approximate (quasistatic

39

[14]) approach to calculate self-consistently the sources (charges and currents) in the metallic rods due to the electromagnetic waves in the lattice. The region beyond the near-field region is the far-field region, where the field changes at the scale of the wavelength. According to Bloch's theorem, the electromagnetic field in the lattice can be decomposed into a set of plane waves with the wave vectors equal to multiples of the reciprocal lattice vectors. The currents, calculated self-consistently in the near-field region, are shown to produce the coupling of several plane waves at the metal rods. The coupling perturbs the plane-wave dispersion relations in the lattice and produces the dispersion characteristics, which are different for the TM and TE waves. Thus, the form of the dispersion curves is determined by both, the lattice symmetries, and the plane-wave coupling at the metal rods.

In this Chapter the results of the quasistatic calculation of the TM and TE dispersion characteristics are presented. The quasistatic results are compared to those obtained previously using the PBGSS code [20]and a good agreement is found.

3.2 Electromagnetic wave propagation in PBG structures

Similarly to Chapter 2, two lattices of long, perfectly conducting rods are considered, namely, the square lattice and the triangular lattice. The Helmholtz equation (2.4) for the wave function follows from the Maxwell equations and is valid for every unit cell of the lattice. Now let $\rho(\vec{x}_\perp, k_z, \omega)$ and $\vec{J}(\vec{x}_\perp, k_z, \omega)$ be the charge and current densities induced by the field at the surfaces of the conducting rods. The Helmholtz equation (A.4) can be generalized for the entire space (vacuum and conducting rods), if the charges and currents are included. The generalized Helmholtz equation is

$$\vec{\nabla}_\perp^2 \psi(\vec{x}_\perp) + \kappa^2 \psi(\vec{x}_\perp) = f(\vec{x}_\perp), \tag{3.1}$$

where $\kappa^2 = \omega^2/c^2 - k_z^2$, and $f(\vec{x}_\perp)$ is a function, related to the currents and charges

$$f(\vec{x}_\perp) = \begin{cases} 4\pi i k_z \rho(\vec{x}_\perp) - \frac{4\pi i \omega}{c^2} J_z(\vec{x}_\perp) & \text{(TM case)}, \\ -4\pi \left(\frac{1}{c}\vec{\nabla} \times \vec{J}\right)_z & \text{(TE case)}. \end{cases} \tag{3.2}$$

Bloch's theorem allows us to expand $\psi(\vec{x}_\perp)$ in a Fourier series,

$$\psi(\vec{x}_\perp) = e^{i\vec{k}_\perp \cdot \vec{x}_\perp} \sum_{m,n} \psi_{m,n} e^{i\vec{G}_{m,n} \cdot \vec{x}_\perp} \tag{3.3}$$

with $\vec{k}_\perp$ being an arbitrary wave vector perpendicular to the rods and $\vec{G}_{m,n}$ being vectors of the reciprocal lattice[21]:

$$\vec{G}_{m,n} = \begin{cases} \frac{2\pi}{b}\hat{e}_x m + \frac{2\pi}{b}\hat{e}_y n, & \text{square lattice,} \\ \left(\frac{2\pi}{b}\hat{e}_x - \frac{2\pi}{\sqrt{3}b}\hat{e}_y\right) m + \frac{4\pi}{\sqrt{3}b}\hat{e}_y n, & \text{triangular lattice.} \end{cases} \tag{3.4}$$

Physically, the Fourier series in Eq. (3.3) corresponds to an expansion of the electromagnetic field into a set of orthogonal plane waves. Only the plane waves with certain wave numbers can exist in the periodic lattice. With the aid of Eq. (3.3), Eq. (3.1) can be rewritten as

$$\sum_{m,n} \left(\kappa^2 - \left(\vec{k}_\perp + \vec{G}_{m,n}\right)^2\right) \psi_{m,n} e^{i\vec{k}_\perp \cdot \vec{x}_\perp + i\vec{G}_{m,n} \cdot \vec{x}_\perp} = f(\vec{x}_\perp). \tag{3.5}$$

Multiplying Eq. (3.5) by $e^{-i\vec{k}_\perp \cdot \vec{x}_\perp - i\vec{G}_{m,n} \cdot \vec{x}_\perp}$ and integrating over the elementary cell area, A, yields

$$\left(\kappa^2 - \left(\vec{k}_\perp + \vec{G}_{m,n}\right)^2\right) \psi_{m,n} = \frac{1}{A} \int_{elementary\,cell} f(\vec{x}_\perp) e^{-i\vec{G}_{m,n} \cdot \vec{x}_\perp - i\vec{k}_\perp \cdot \vec{x}_\perp} d^2\vec{x}_\perp. \tag{3.6}$$

3.3 Plain wave approximation

The simplest approximation to solve the system of equations (3.6) can be made using the assumption that there is no interaction between the rods and the electromagnetic

waves, i.e., $f(\vec{x}_\perp) = 0$. This is called the "plane-wave approximation" [2, 22]. The eigenfrequencies obtained in the framework of this approximation are simply

$$\left(\frac{\omega}{c}\right)_{m,n} = \left|\vec{k}_\perp + \vec{G}_{m,n}\right|.$$ (3.7)

The sets of reciprocal lattice eigenvectors $\vec{G}_{m,n}$ corresponding to the several lowest $\left|\vec{k}_\perp + \vec{G}_{m,n}\right|'$s is shown in Tables 3.1 and 3.2 for square and triangular lattices and different $\vec{k}_\perp$ on the edge of the Brillouin zone.

The plots of four lowest eigenfrequencies in square and triangular lattices obtained in the framework of plane wave approximations are shown in Figures 3-1(a) and 3-1(b) with dashed lines. For comparison the calculated dispersion curves for TE modes in square and triangular lattices for $a/b = 0.1$ are shown with solid lines. The strong resemblance between the two sets of dispersion curves can be seen. However, the dispersion curves given by plane wave approximation (Eq. (3.7)) are the consequence of the crystal symmetries only. They are independent of the nature of the interactions in the periodic structure and are the same for all photonic crystals with the same geometry. There is also the resemblance between the plane wave approximation curves and those for the TM modes for small ratios of a/b. But the comparison with the TE mode dispersion curves is more impressive, since, as it will be shown below, the interaction of the plane waves on metal posts in TE mode is smaller than in TM mode for the same ratio of a/b.

The dispersion curves in the plane-wave approximation for both the square and triangular lattices are also plotted in Ref. [22].

Table 3.1: The plane waves in square lattice listed according to their $\left|\vec{k}_\perp + \vec{G}_{-m,-n}\right|$ for the $\vec{k}_\perp$ on the edge of the Brillouin zone.

$\Gamma-$ point, $\vec{k}_\perp = 0$		
$\frac{b}{2\pi}\left|\vec{k}_\perp + \vec{G}_{-m,-n}\right|$	0	1
		$(0,1)$
		$(1,0)$
(m,n)	$(0,0)$	$(-1,0)$
		$(0,-1)$

$\Delta-$ point, $\vec{k}_\perp = \frac{2\pi}{b}\left(\delta,0\right),\ 0 < \delta < 1/2$			
$\frac{b}{2\pi}\left|\vec{k}_\perp + \vec{G}_{-m,-n}\right|$	δ	$1-\delta$	$\sqrt{\delta^2+1}$
			$(0,1)$
(m,n)	$(0,0)$	$(1,0)$	$(0,-1)$

$X-$ point, $\vec{k}_\perp = \frac{\pi}{b}\left(1,0\right)$		
$\frac{b}{2\pi}\left|\vec{k}_\perp + \vec{G}_{-m,-n}\right|$	$1/2$	$\sqrt{5}/2$
		$(0,1)$
	$(0,0)$	$(0,-1)$
(m,n)	$(1,0)$	$(1,1)$
		$(1,-1)$

$Z-$ point, $\vec{k}_\perp = \frac{2\pi}{b}\left(1/2,\delta\right),\ 0 < \delta < 1/2$

43

$\frac{b}{2\pi}\left|\vec{k}_\perp + \vec{G}_{-m,-n}\right|$	$\sqrt{\delta^2 + 1/4}$	$\sqrt{(1-\delta)^2 + 1/4}$
(m,n)	$(0,0)$	$(0,1)$
	$(1,0)$	$(1,1)$

$M-$ point, $\vec{k}_\perp = \frac{\pi}{b}\,(1,1)$

$\frac{b}{2\pi}\left|\vec{k}_\perp + \vec{G}_{-m,-n}\right|$	$\sqrt{2}/2$
	$(0,0)$
	$(1,0)$
(m,n)	$(0,1)$
	$(1,1)$

$\Sigma-$ point, $\vec{k}_\perp = \frac{2\pi}{b}\,(\delta,\delta)\,,\ 0 < \delta < 1/2$

$\frac{b}{2\pi}\left|\vec{k}_\perp + \vec{G}_{-m,-n}\right|$	$\sqrt{2}\delta$	$\sqrt{(1-\delta)^2 + \delta^2}$	$\sqrt{(1+\delta)^2 + \delta^2}$
(m,n)	$(0,0)$	$(0,1)$	$(0,-1)$
		$(1,0)$	$(-1,0)$

Table 3.2: The plane waves in triangular lattice listed according to their $\left|\vec{k}_\perp + \vec{G}_{-m,-n}\right|$ for the $\vec{k}_\perp$ on the edge of the Brillouin zone.

$\Gamma-$ point, $\vec{k}_\perp = 0$		
$\frac{b}{2\pi}\left|\vec{k}_\perp + \vec{G}_{-m,-n}\right|$	0	$2/\sqrt{3}$
		$(1,0)$
		$(1,1)$
		$(0,1)$
(m,n)	$(0,0)$	$(0,-1)$
		$(-1,-1)$
		$(-1,0)$

$\Sigma-$ point, $\vec{k}_\perp = \frac{2\pi}{b}\left(0,\delta\right),\ 0 < \delta < 1/\sqrt{3}$			
$\frac{b}{2\pi}\left|\vec{k}_\perp + \vec{G}_{-m,-n}\right|$	δ	$\left(2/\sqrt{3}-\delta\right)$	$\sqrt{\frac{\left(1-\sqrt{3}\delta\right)^2}{3}+1}$
			$(1,1)$
(m,n)	$(0,0)$	$(0,1)$	$(-1,0)$

$X-$ point, $\vec{k}_\perp = \frac{2\pi}{b}\left(0,1/\sqrt{3}\right)$	
$\frac{b}{2\pi}\left|\vec{k}_\perp + \vec{G}_{-m,-n}\right|$	$1/\sqrt{3}$ $\qquad$ 1
(m,n)	$(0,0)$ $\qquad$ $(1,1)$
	$(0,1)$ $\qquad$ $(-1,0)$

$T'-$ point, $\vec{k}_\perp = \frac{2\pi}{b}\left(\delta,1/\sqrt{3}\right),\ 0 < \delta < 1/3$

$\frac{b}{2\pi}\left|\vec{k}_\perp + \vec{G}_{-m,-n}\right|$	$\sqrt{\frac{1}{3}+\delta^2}$	$(1-\delta)$	$(1+\delta)$
(m,n)	$(0,0)$ $(0,1)$	$(1,1)$	$(-1,0)$

$$J-\text{ point, } \vec{k}_\perp = \tfrac{2\pi}{b}\left(1/3, 1/\sqrt{3}\right)$$

$\frac{b}{2\pi}\left|\vec{k}_\perp + \vec{G}_{-m,-n}\right|$	2/3	4/3
(m,n)	$(0,0)$ $(1,1)$ $(0,1)$	$(-1,0)$ $(1,0)$ $(1,2)$

$$T-\text{ point, } \vec{k}_\perp = \tfrac{2\pi}{b}\left(\delta, \sqrt{3}\delta\right),\ 0 < \delta < 1/3$$

$\frac{b}{2\pi}\left|\vec{k}_\perp + \vec{G}_{-m,-n}\right|$	2δ	$\sqrt{\frac{(2-3\delta)^2}{3}+\delta^2}$	$\sqrt{(1-\delta)^2 + \frac{(1+3\delta)^2}{3}}$
(m,n)	$(0,0)$	$(0,1)$ $(1,1)$	$(1,0)$ $(-1,0)$

3.4 Quasistatic approximation for thin conducting rods

The plane-wave approximation is a zeroth-order analysis. In this section, we consider a first-order approximation for $f(\vec{x}_\perp)$, which describes the interactions between the electromagnetic waves and conducting rods in Eqs. (3.6). The first-order approximation holds in the limit when the rods are small compared to the wavelength, i.e., $\kappa a \ll 1$ (quasistatic limit) and to the distance between the rods, i.e., $a/b \ll 1$. In this limit, approximations can be made to the wave equation (3.1), and the source
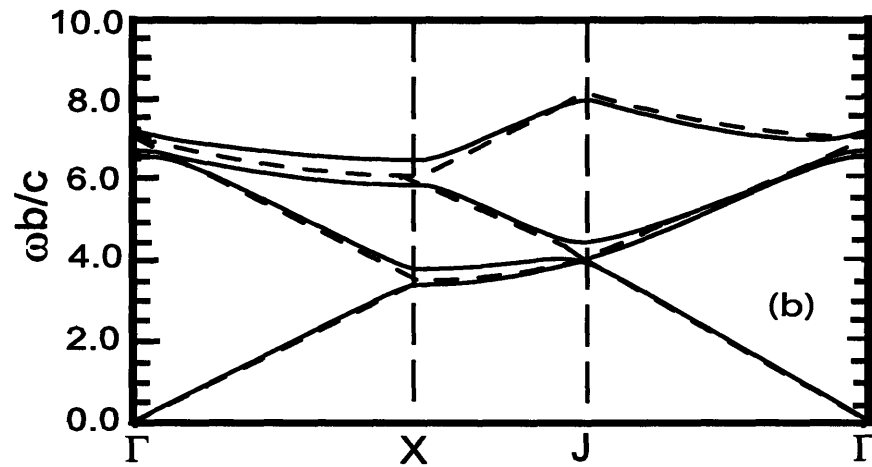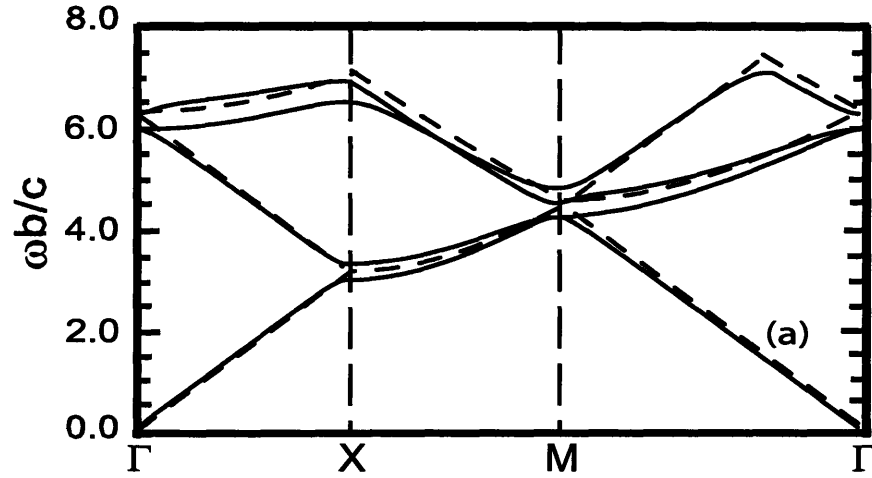
Figure 3-1: Dispersion curves as obtained in the framework of plane waves approximation (dashed lines) and for the TE modes in a lattice with $a/b = 0.1$ (solid lines): (a) square lattice, and (b) triangular lattice.

Figure 3-2: Illustration of the near- and far-field regions in the quasistatic approximation.

$f(\vec{x}_\perp)$ can be self-consistently related to the wave function $\psi(\vec{x}_\perp)$.

Assume that the center of the rod (m, n) is located at $\vec{x}_\perp = \vec{T}_{m,n}$. We introduce the notation $\vec{r} = \vec{x}_\perp - \vec{T}_{m,n}$. There are two regions surrounding the rod (m, n), where the behavior of $\psi^{(m,n)}(\vec{x}_\perp)$ is qualitatively different [23]: near-field region and far-field region, as shown in figure 3-2. In the near-field region where $\kappa r \ll 1$, the wave function $\psi^{(m,n)}$ changes rapidly, i.e.,

$$\left| \vec{\nabla}^2 \psi_{near}^{(m,n)} \right| \sim \psi_{near}^{(m,n)}/a^2 \gg \kappa^2 \psi_{near}^{(m,n)}. \tag{3.8}$$

In the far-field region where $\kappa r \gtrsim 1$, the wave-function $\psi^{(m,n)}$ changes slowly, i.e.,

$$\left| \vec{\nabla}^2 \psi_{far}^{(m,n)} \right| \sim \kappa^2 \psi_{far}^{(m,n)}. \tag{3.9}$$

The near- and the far-field solutions must match at the boundary of the two regions,

$$\psi_{near}^{(m,n)} \Big|_{r \sim 1/\kappa} \sim \psi_{far}^{(m,n)} \Big|_{r \sim 1/\kappa}. \tag{3.10}$$

In the remainder of this section, we use the near- and the far-field solutions to derive approximate self-consistent expressions for the sources $f(\vec{x}_\perp)$ and solve the system of Eqs. (3.6). We now consider the TM and TE modes separately.

3.4.1 The TM case

Outside the conducting rods we have $f(\vec{x}_\perp) = 0$. Taking into account Eq. (3.8), we write Eq. (3.1) in the near-field region in the electrostatic approximation as

$$\vec{\nabla}_\perp^2 \psi_{near}^{(m,n)} = 0. \tag{3.11}$$

For the TM case the boundary condition at the rod is given by

$$\left. \psi_{near}^{(m,n)} \right|_{r=a} = 0. \tag{3.12}$$

The general solution of the Laplace Eq. (3.11) in 2D is given by

$$\psi_{near}^{(m,n)} = u_0 + v_0 \ln r + \sum_{l=1}^{\infty} \left(u_l r^l + \frac{v_l}{r^l} \right) \left(p_l \cos l\theta + q_l \sin l\theta \right). \tag{3.13}$$

Here u_l, v_l, p_l, q_l are arbitrary constants. It is sufficient to keep only the first two terms in Eq. (3.13) to be able to satisfy the boundary conditions in Eqs. (3.10) and (3.12). The solution satisfying the boundary conditions is

$$\psi_{near}^{(m,n)} = \psi_{far}^{(m,n)} \left(1 - \frac{\ln \kappa r}{\ln \kappa a} \right). \tag{3.14}$$

Using the solution in Eq. (3.14) we can calculate the source in the rod (m,n) creating this field. We obtain

$$
\begin{aligned}
f^{(m,n)}(\vec{r}) &= \vec{\nabla}_\perp^2 \psi_{near}^{(m,n)} \cong -\frac{\psi_{far}^{(m,n)}}{\ln \kappa a} \vec{\nabla}_\perp^2 \ln \kappa r \\
&= -\frac{2\pi}{\ln \kappa a} \psi_{far}^{(m,n)} \delta(\vec{r}).
\end{aligned} \tag{3.15}
$$

Here $f^{(m,n)}(\vec{r})$ is the source in the rod (m,n). In the vicinity of the rod (m,n) with the source in a single rod included the equation for ψ becomes

$$\vec{\nabla}_\perp^2 \psi + \kappa^2 \psi = -\frac{2\pi}{\ln \kappa a} \psi_{far}^{(m,n)} \delta(\vec{r}). \tag{3.16}$$

The far-field solutions of different rods must match: $\psi_{far}^{(m,n)} \equiv \psi(\vec{x}_\perp)$. For a periodic system of conducting rods, we must sum over all the rods to calculate the total sources and obtain the following wave equation:

$$
\begin{aligned}
\vec{\nabla}_\perp^2 \psi(\vec{x}_\perp) + \kappa^2 \psi(\vec{x}_\perp) &= f(\vec{x}_\perp) \\
&= -\frac{2\pi}{\ln \kappa a} \sum_{m,n} \psi_{far}^{(m,n)} \delta\left(\vec{x}_\perp - \vec{T}_{m,n}\right) \qquad (3.17) \\
&= -\frac{2\pi}{\ln \kappa a} \sum_{m,n} \psi(\vec{x}_\perp) \delta\left(\vec{x}_\perp - \vec{T}_{m,n}\right).
\end{aligned}
$$

Equation (3.6) along with from Eq. (3.17) becomes

$$
\left(\kappa^2 - \left(\vec{k}_\perp + \vec{G}_{m,n}\right)^2\right) \psi_{m,n} = -\frac{2\pi}{A \ln \kappa a} \sum_{m',n'} \psi_{m',n'}. \qquad (3.18)
$$

The eigenvalues of the linear system in Eqs. (3.18) can now be found by diagonalizing the infinite matrix

$$
M = \left\| \begin{array}{ccccc}
\vec{k}_\perp^2 - \frac{\alpha}{A} & -\frac{\alpha}{A} & \cdots & -\frac{\alpha}{A} & \cdots \\
-\frac{\alpha}{A} & \left(\vec{k}_\perp + \vec{G}_{0,1}\right)^2 - \frac{\alpha}{A} & \cdots & -\frac{\alpha}{A} & \cdots \\
\cdots & \cdots & \cdots & \cdots & \cdots \\
-\frac{\alpha}{A} & -\frac{\alpha}{A} & \cdots & \left(\vec{k}_\perp + \vec{G}_{m,n}\right)^2 - \frac{\alpha}{A} & \cdots \\
\cdots & \cdots & \cdots & \cdots & \cdots
\end{array} \right\|, \qquad (3.19)
$$

where $\alpha = 2\pi / \ln \kappa a$. Because the coefficient α depends on the eigenfrequency κ, the matrix M must be diagonalized iteratively for each eigenvalue.

The eigenvalues of the infinite matrix M can be calculated approximately as the eigenvalues of a truncated matrix with a finite rank. This corresponds to approximating ψ with a finite number of lowest terms of the Fourier representation in Eq. (3.3). The number of Fourier harmonics in the representation needed to achieve the desired accuracy increases with increasing a/b.

For small a/b the truncation of the Fourier representation in Eq. (3.3) gives a simple physical picture of the interactions of a finite number of plane waves at the

conducting rods of the lattice. For $a/b \to 0$ the interactions basically become binary, that is, each plane wave interacts primarily with another plane wave, which has the wave vector of the same magnitude. For example, the binary interaction of plane waves can explain the behavior of the lowest local band gap width at the X points of the square and triangular lattices. We consider the X point ($\vec{k}_\perp = (\pi/b)\,\hat{e}_x$) of the square lattice and restrict ourselves to the interaction of the two plane waves with the lowest values of $\left| \vec{k}_\perp + \vec{G}_{m,n} \right|$. These waves correspond to $(m_1,n_1) = (0,0)$ and $(m_2,n_2) = (-1,0)$ with $\left| \vec{k}_\perp + \vec{G}_{m,n} \right| = \pi/b$ for both. The truncated matrix $\widetilde{M}$, describing the interaction of the two waves at the X point, is simply

$$
\widetilde{M} = \left\| \begin{array}{cc} \frac{\pi^2}{b^2} - \frac{\alpha}{b^2} & -\frac{\alpha}{b^2} \\[2em] -\frac{\alpha}{b^2} & \frac{\pi^2}{b^2} - \frac{\alpha}{b^2} \end{array} \right\| .
\tag{3.20}
$$

The eigenvalues of $\widetilde{M}$ in Eq. (3.20) are

$$
\begin{aligned}
\kappa_1^2 &= \frac{\pi^2}{b^2}\left(1 - \frac{2\alpha}{\pi^2}\right), \\
\kappa_2^2 &= \frac{\pi^2}{b^2}.
\end{aligned}
\tag{3.21}
$$

Recall that α is a function of κ itself, so the equation for κ_1 must be solved iteratively. To the lowest order, $\alpha = \alpha_0 = 2\pi/\ln(\pi a/b)$, and the full width of the local band gap at the X point is given by

$$
\Delta\left(\frac{\omega b}{c}\right) = b\left(\kappa_1 - \kappa_2\right) = \frac{\alpha_0}{\pi} = \frac{2}{\ln(\pi a/b)}
\tag{3.22}
$$

for small a/b. This logarithmic dependence agrees well with the numerical calculations using the PBGSS code [20].

Similarly, considering the interaction of two lowest plane waves at the X point of the triangular lattice ($\vec{k}_\perp = \left(2\pi/\sqrt{3}b\right)\hat{e}_y$), we find that the full width of the local

band gap at the X point of the triangular lattice is given by

$$\Delta\left(\frac{\omega b}{c}\right) = \frac{\alpha_0}{\pi} = \frac{2}{\ln\left(2\pi a/\sqrt{3}b\right)} \tag{3.23}$$

for small a/b.

In the same manner, we numerically calculate the entire dispersion characteristics in the square and triangular lattices by including many plane-wave interactions. For $a/b \to 0$ only a limited number of the plane waves is needed to achieve a good approximation of ψ. It is reasonable to start the iterative process of solving the matrix M with the initial value for κ being its plane-wave value κ_0 in a given point of the $\vec{k}_\perp$ space. As the eigenvalues of $M\left[\alpha\left(\kappa_0\right)\right]$ are found, the initial guesses for κ are corrected and new α's are calculated. Then, the matrix M is diagonalized again with new α's. The iterative process has been performed using a computer. Results of these calculations are summarized in figure 3-3(a) and figure 3-4(a). In figure 3-3(a) the results are shown for the TM mode in a square lattice with $a/b = 0.05$. The quasistatically calculated eigenvalues are plotted with dots. Solid curves show the dispersion characteristics obtained from the PBGSS calculations. Five to twelve lowest vectors of the reciprocal lattice, depending on the symmetry of the particular $\overrightarrow{k}_\perp$ point, are taken into account, and the four lowest eigenmodes are plotted. Similarly, in figure 3-4(a), the results are shown for the TM mode in a triangular lattice with $a/b = 0.05$. As in figure 3-3(a), the eigenvalues calculated with the quasistatic approximation are plotted with dots, whereas the solid curves show the dispersion characteristics obtained from the PBGSS calculations. Six to twelve of the lowest vectors of the reciprocal lattice are taken into account, and the four lowest eigenfrequencies are plotted. The three special points in figure 3-3(a), Γ, X, and M, correspond to $\vec{k}_\perp = 0$, $\vec{k}_\perp = (\pi/b)\hat{e}_x$, and $\vec{k}_\perp = (\pi/b)(\hat{e}_x + \hat{e}_y)$, respectively. The three special points in figure 3-4(a), Γ, X, and J, correspond to $\vec{k}_\perp = 0$, $\vec{k}_\perp = (2\pi/\sqrt{3}b)\hat{e}_x$, and $\vec{k}_\perp = (2\pi/3b)(\hat{e}_x + \sqrt{3}\hat{e}_y)$. As seen in both figure 3-3(a) and figure 3-4(a), there is a good agreement between the PBGSS calculations and the quasistatic approximation.
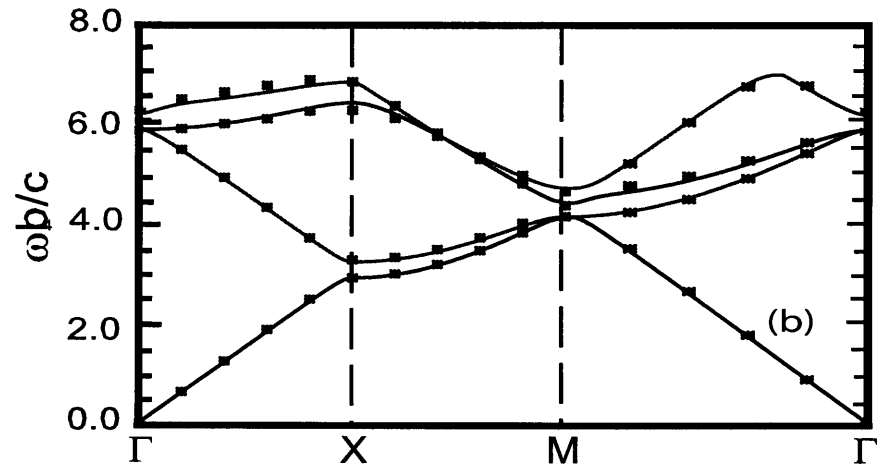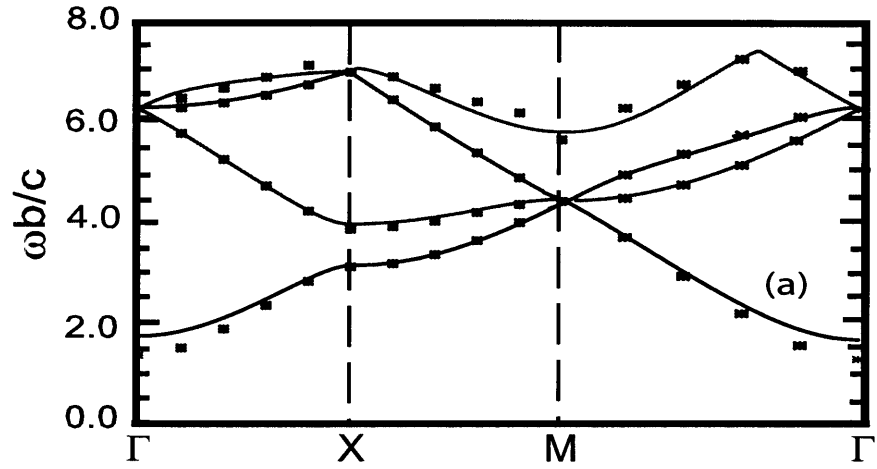
Figure 3-3: Dispersion characteristics in the triangular lattice as calculated with the PBGSS code (solid curves) and the quasistatic approximation (dots) for (a) the TM modes with $a/b = 0.05$ and (b) the TE modes with $a/b = 0.1$.
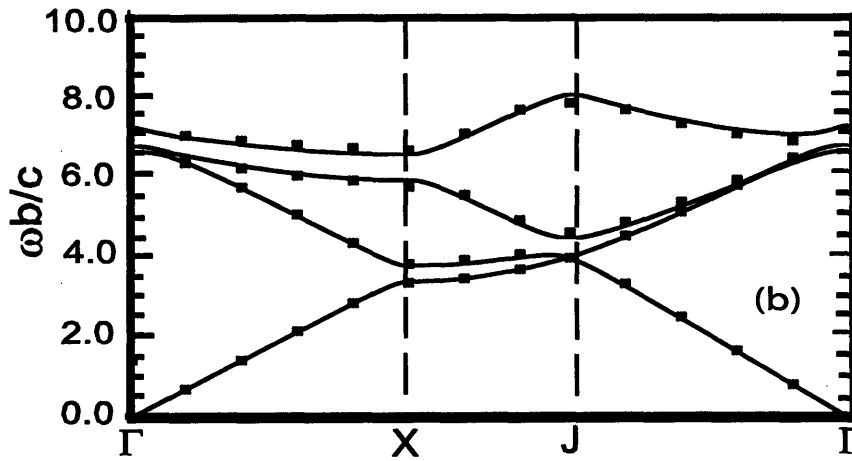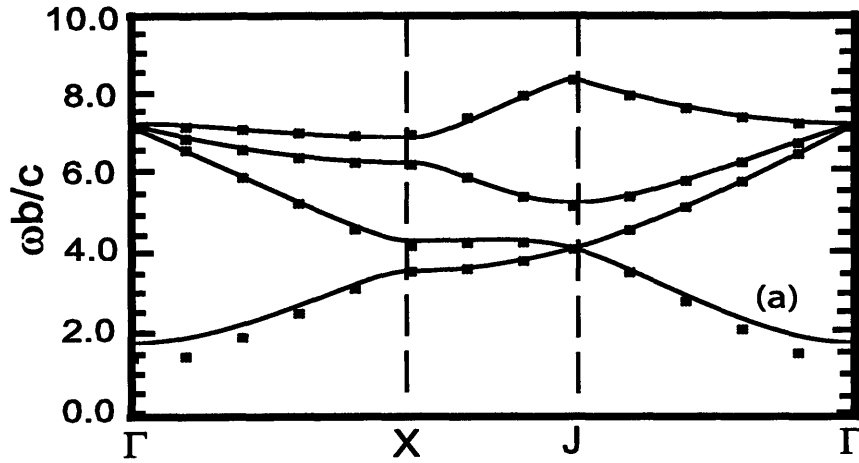
Figure 3-4: Dispersion characteristics in the triangular lattice as calculated with the PBGSS code (solid curves) and the quasistatic approximation (dots) for (a) the TM modes with $a/b = 0.05$ and (b) the TE modes with $a/b = 0.1$.

3.4.2 The TE case

As in the TM case, the Laplace equation is valid for ψ in a near-field field region around the rod (m, n) for the TE wave, i.e.,

$$\vec{\nabla}_{\perp}^2 \psi_{near}^{(m,n)} = 0. \tag{3.24}$$

For the TE case ψ stands for the longitudinal component of the magnetic field. The boundary condition for ψ at $r = a$ is

$$\left. \frac{\partial \psi_{near}^{(m,n)}}{\partial r} \right|_{r=a} = 0. \tag{3.25}$$

It is convenient to rewrite the boundary condition at $\kappa r \sim 1$ given by Eq. (3.10) in the form

$$\left. \left(\vec{r} \cdot \vec{\nabla}_{\perp} \psi_{near}^{(m,n)} \right) \right|_{r \sim 1/\kappa} \sim \left. \left(\vec{r} \cdot \vec{\nabla}_{\perp} \psi_{far}^{(m,n)} \right) \right|_{r \sim 1/\kappa}. \tag{3.26}$$

It is sufficient to keep only three terms in the general solution of Laplace's equation given by Eq. (3.13) in order to satisfy the boundary conditions in Eqs. (3.25) and (3.26). The solution satisfying the boundary conditions is

$$\psi_{near}^{(m,n)} = u_0 + \left(\vec{r} \cdot \vec{\nabla}_{\perp} \psi_{far}^{(m,n)} \right) \left(1 + \frac{a^2}{r^2} \right), \tag{3.27}$$

where u_0 is a constant, and use was made of the relation

$$\left| \vec{\nabla}_{\perp} \psi_{far}^{(m,n)} \right| \left(r + \frac{a^2}{r} \right) \cos \theta = \left(\vec{r} \cdot \vec{\nabla}_{\perp} \psi_{far}^{(m,n)} \right) \left(1 + \frac{a^2}{r^2} \right). \tag{3.28}$$

Using the solution in Eq. (3.27), we can find that the source in the rod (m, n) creating this field is

$$\begin{aligned} f^{(m,n)}(\vec{r}) &= \vec{\nabla}_{\perp}^2 \psi_{near}^{(m,n)} \cong \left(\vec{r} \cdot \vec{\nabla}_{\perp} \psi_{far}^{(m,n)} \right) \vec{\nabla}_{\perp}^2 \frac{a^2}{r^2} \\ &= 2\pi a^2 \vec{\nabla}_{\perp} \psi_{far}^{(m,n)} \cdot \vec{\nabla}_{\perp} \delta(\vec{r}). \end{aligned} \tag{3.29}$$

The equation for ψ in the vicinity of the rod (m, n) with the source in a single rod included is

$$\vec{\nabla}_{\perp}^2 \psi + \kappa^2 \psi = 2\pi a_{\perp}^2 \vec{\nabla} \psi_{far}^{(m,n)} \cdot \vec{\nabla}_{\perp} \delta\left(\vec{r}\right). \tag{3.30}$$

For a periodic system of conducting rods the far-field solutions of different rods must match: $\psi_{far}^{(m,n)} \equiv \psi\left(\vec{x}_{\perp}\right)$. In equation for $\psi\left(\vec{x}_{\perp}\right)$ we sum over the contributions from all the rods to calculate the total sources. This yields

$$
\begin{aligned}
\vec{\nabla}_{\perp}^2 \psi\left(\vec{x}_{\perp}\right) + \kappa^2 \psi\left(\vec{x}_{\perp}\right) &= f\left(\vec{x}_{\perp}\right) \\
&= 2\pi a^2 \sum_{m,n} \vec{\nabla}_{\perp} \psi_{far}^{(m,n)} \cdot \vec{\nabla}_{\perp} \delta\left(\vec{x}_{\perp} - \vec{T}_{m,n}\right) \\
&= 2\pi a^2 \sum_{m,n} \vec{\nabla}_{\perp} \psi\left(\vec{x}_{\perp}\right) \cdot \vec{\nabla}_{\perp} \delta\left(\vec{x}_{\perp} - \vec{T}_{m,n}\right).
\end{aligned}
\tag{3.31}
$$

Equation (3.6) with $f\left(\vec{x}_{\perp}\right)$ as in Eq. (3.31) becomes

$$\left(\kappa^2 - \left(\vec{k}_{\perp} + \vec{G}_{m,n}\right)^2\right) \psi_{m,n} = -\frac{2\pi a^2}{A} \sum_{m',n'} \psi_{m',n'} \left(\vec{k}_{\perp} + \vec{G}_{m',n'}\right) \cdot \left(\vec{k}_{\perp} + \vec{G}_{m,n}\right). \tag{3.32}$$

The eigenvalues of the system can now be found by diagonalizing the infinite matrix

$$M = \left\| \begin{array}{cccc}
\vec{k}_{\perp}^2 & \cdots & -\alpha\left(\vec{k}_{\perp} + \vec{G}_{m,n}\right) \cdot \vec{k}_{\perp} & \cdots \\
-\alpha \vec{k}_{\perp} \cdot \left(\vec{k}_{\perp} + \vec{G}_{0,1}\right) & \cdots & -\alpha\left(\vec{k}_{\perp} + \vec{G}_{m,n}\right) \cdot \left(\vec{k}_{\perp} + \vec{G}_{0,1}\right) & \cdots \\
\cdots & \cdots & \cdots & \cdots \\
-\alpha \vec{k}_{\perp} \cdot \left(\vec{k}_{\perp} + \vec{G}_{m,n}\right) & \cdots & \left(\vec{k}_{\perp} + \vec{G}_{m,n}\right)^2 & \cdots \\
\cdots & \cdots & \cdots & \cdots
\end{array} \right\|, \tag{3.33}$$

where $\alpha = 2\pi a^2/A$. Note that unlike in the TM case, the coefficient is independent of the eigenvalues κ.

The eigenvalues of the infinite matrix M can be calculated approximately as the eigenvalues of a truncated matrix with a finite rank. Thus, for $a/b \to 0$, we can explain the behavior of the lowest local band gap width for the TE modes at the X points of square and triangular lattices. Consider the lowest binary interaction of

plane waves at the X point. For the square lattice, the X point corresponds to $\vec{k}_\perp = (\pi/b)\,\hat{e}_x$. The two plane waves with the lowest $\left|\vec{k}_\perp + \vec{G}_{m,n}\right|$'s have $(m_1,n_1) = (0,0)$ and $(m_2,n_2) = (-1,0)$ and $\left|\vec{k}_\perp + \vec{G}_{m,n}\right| = \pi/b$. The truncated matrix $\widetilde{M}$, describing the interaction of the two waves at the X point is

$$\widetilde{M} = \left\| \begin{array}{cc} \left(\frac{\pi}{b}\right)^2 & \alpha\left(\frac{\pi}{b}\right)^2 \\[3mm] \alpha\left(\frac{\pi}{b}\right)^2 & \left(\frac{\pi}{b}\right)^2 \end{array} \right\|. \tag{3.34}$$

The eigenvalues of $\widetilde{M}$ are

$$\kappa_{1,2}^2 = \left(\frac{\pi}{b}\right)^2 (1 \pm \alpha). \tag{3.35}$$

For small a/b, the full width of the local band gap at the X point scales as

$$\Delta\left(\frac{\omega b}{c}\right) = b\left(\kappa_1 - \kappa_2\right) = \pi\alpha = 2\left(\frac{\pi a}{b}\right)^2. \tag{3.36}$$

This agrees well with the numerical calculations using the PBGSS code. Similarly, considering the interaction of the two lowest plane waves at the X point of the triangular lattice $(\vec{k}_\perp = \left(2\pi/\sqrt{3}b\right)\hat{e}_y)$, we find that the full width of the local band gap at the X point of the triangular lattice is given by

$$\Delta\left(\frac{\omega b}{c}\right) = \frac{2}{\sqrt{3}}\pi\alpha = \frac{8}{3}\left(\frac{\pi a}{b}\right)^2. \tag{3.37}$$

We calculate numerically the entire TE dispersion characteristics in both square and triangular lattices by including multiple plane-wave interactions at the metal rods. As illustrated in Figs. 3-3(b) and 3-4(b) for $a/b \to 0$, the approximation is good even for a small number of Fourier components. In figure 3-3(b), the results of the quasistatic calculations are shown with dots for the TE mode in a square lattice of rods with $a/b = 0.1$. Solid curves show the dispersion characteristics obtained from the PBGSS calculations. Five to twelve of the lowest vectors in the reciprocal lattice (depending on the symmetry of the particular $\vec{k}_\perp$ point) are taken into account, and four lowest eigenmodes are plotted. Similarly, in figure 3-4(b) the results of the

quasistatic calculations are shown with dots for the TE mode in a triangular lattice of rods with $a/b = 0.1$. Solid curves show the dispersion characteristics obtained from the PBGSS calculations. Six to twelve of the lowest vectors of the reciprocal lattice were taken into account, and the four lowest eigenmodes are plotted. The three special points in figure 3-3(b), Γ, X, and M, correspond to $\vec{k}_\perp = 0$, $\vec{k}_\perp = (\pi/b)\,\hat{e}_x$, and $\vec{k}_\perp = (\pi/b)\,(\hat{e}_x + \hat{e}_y)$ respectively. The three special points in figure 3-4(b), Γ, X, and J, correspond to $\vec{k}_\perp = 0$, $\vec{k}_\perp = \left(2\pi/\sqrt{3}b\right)\hat{e}_x$, and $\vec{k}_\perp = (2\pi/3b)\left(\hat{e}_x + \sqrt{3}\hat{e}_y\right)$.

For the TE case, the agreement between the quasistatic and the PBGSS calculations is even better than for the TM case. This is because the interactions of the waves are determined by the small parameters $\alpha_{TE} = 2\pi a^2/A$ (with $A \sim b^2$) for the TE case and $\alpha_{TM} = 2\pi/\ln \kappa a$ (with $\kappa \sim 1/b$) for the TM case. For the same value of a/b, α_{TE} is much smaller than α_{TM}. Thus the quasistatic theory approximates the dispersion characteristics for the TE case much better than those for the TM case with the same value of a/b.

Chapter 4

Study of two-dimensional PBG resonators

4.1 Introduction

Up to now we were only dealing with infinite periodic systems of rods. We found the global band gaps for the triangular lattice of metal rods. No modes were allowed with frequencies inside the band gaps. However, by perturbing a single or several lattice sites we can permit a single or a set of closely spaced modes that have frequencies in the gap. The perturbation in two dimensions can be created by removing a single rod or replacing it with another one which has a size or shape different from the original. The wave with a frequency inside the band gap cannot propagate into the bulk of the PBG structure, so, if conditions for the resonance are satisfied, then the mode of this frequency can be localized around the defect.

Unlike in a traditional pillbox resonator only the modes with frequencies inside the band gap can be confined in a PBG cavity. Other frequencies will leak out through the PBG wall. Consequently the spectrum of eigenmodes in a PBG resonator is quite rare. If a PBG resonator could be designed that would selectively confine an accelerating ($TM_{01}-$like) mode, this resonator would be a good candidate for an accelerator cell [11, 10]. Recall that in a traditional accelerator cell (e.g. a pillbox cavity) in addition to the accelerating mode, there exist many HOM, which can be excited by a beam

passing through the cavity. The excited modes, called "wakefields" induce unwanted transverse motion of electrons and emittance growth in consequent bunches. The advantage of the PBG accelerating cavity would be in efficient suppression of the higher-frequency, higher-order mode wakefields.

The main object of our investigation will be the simplest possible two-dimensional metallic PBG resonator, which is formed by one missing rod in a triangular lattice (figure 1-4). We assume that the rods are sandwiched between metal plates, which are so closely spaced that we have $k_z = 0$ propagation for the range of frequencies of the interest and only TM modes can exist in such structure. In the past, many codes were developed for calculating the modes confined in defects in dielectric lattices [2]. However, for analysis of metallic PBG cavities formed by single or multiple defects in the PBG structure, finite-element codes such as SUPERFISH [24] and High Frequency Structure Simulator (HFSS) [25] are ideally suited. So we did not have to develop a separate code to study metal PBG cavities. Although both, SUPERFISH and HFSS codes, can only calculate the eigenmodes of finite electromagnetic structures, these are actually the only possible structures to be built. We restricted ourselves to considering only three rows of metal rods surrounded by a cylindrical metal wall. The wall radius R_{wall} is of the order of 3.5 b, where b is the lattice spacing. This PBG resonator geometry is shown in figure 1-4. We found that the mode with a frequency in the band gap was very well confined in a PBG structure with only three rows of rods.

This chapter will deal with the design of a single-mode PBG resonator, the construction of PBG resonators and the proof-of-principle cold tests. In cold tests, we demonstrated the TM_{01}−like mode mode confinement in a PBG resonator and the suppression of the HOM. Also we demonstrated a high Q PBG resonator at 11 GHz.

4.2   Eigenmodes of a PBG resonator

The SUPERFISH and the HFSS codes were applied to compute the eigenmodes of a PBG resonator shown in figure 1-4. The resonators with different ratios of the
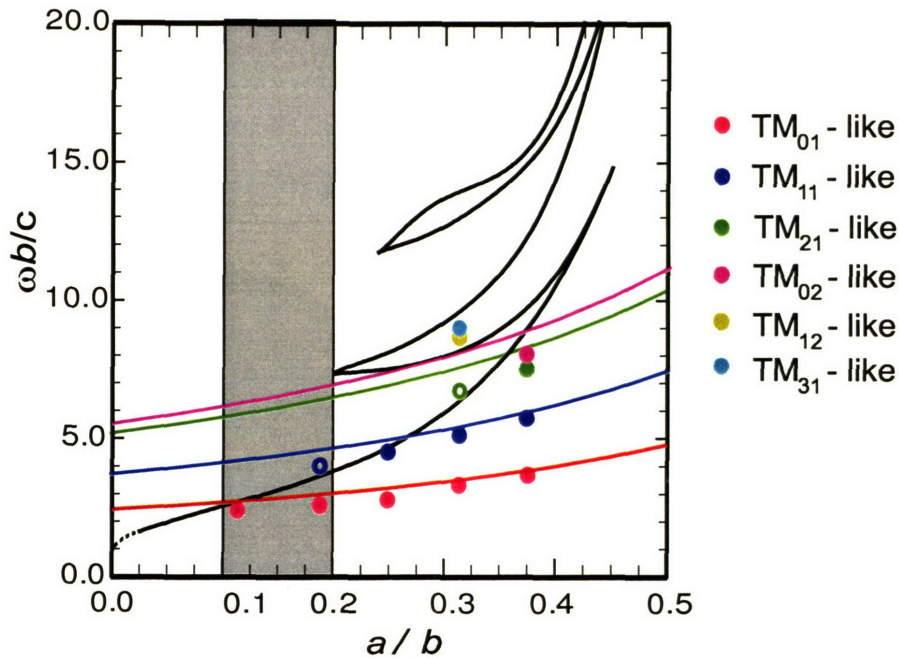
Figure 4-1: The eigenfrequencies of the TM modes in PBG cavity formed by one rod removed from the triangular lattice. The eigenfrequencies are plotted versus the ratio of a/b. Black solid lines show the band gap boundaries. Color solid lines represent the frequencies of modes of a pillbox cavity with the radius $R = b - a$.

rod's radii, a, to the spacing between the rods, b, were modelled. The computed eigenfrequencies for the TM modes are plotted in figure 4-1. The same band gap picture as in figure 2-3(b) is shown on the $\omega b/c$ versus a/b diagram. The frequencies of the defect modes are plotted over the band gap picture with color hollow and filled circles. Because of the presence of the metal wall behind the rows of rods, the appearance of the mode can actually be predicted for the smaller ratios of a/b than when the mode is confined by the lattice. Hollow circles in the figure represent the frequencies of the modes until they are really confined and filled circles show the frequencies of the confined modes. The solid color lines on the picture show the eigenfrequencies of the pillbox cavity with the radius $R = b - a$. As the radius of the rods increases the effective radius of the PBG cavity goes down and the frequencies of the eigenmodes increase.

We noted from the Figure 4-1 that for some values of the rod's radii ($0.1 < a/b <$

PBG cavity,
TM_{01}- like mode

Pillbox cavity,
TM_{01} mode
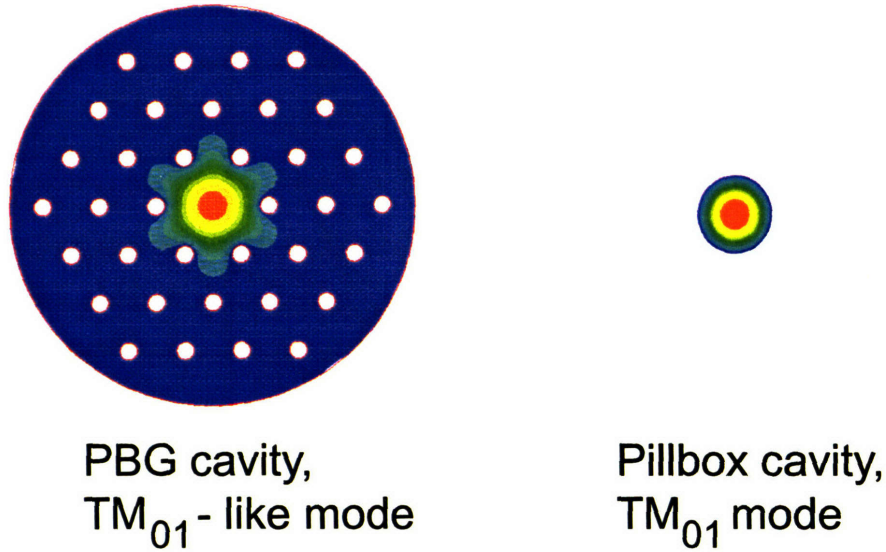
Figure 4-2: A comparison of the electric field patterns in the $TM_{01}-$like mode in a PBG resonator and the TM_{01} mode in a pillbox resonator

0.2) only a single lowest order mode is confined by a PBG structure. This frequency range is shaded in figure 4-1. The structure of the confined mode resembles the structure of the TM_{01} mode in a pillbox resonator (figure 4-2), thus we named it the $TM_{01}-$ like mode. The $TM_{01}-$ like mode can be employed as an accelerating mode in a PBG accelerator cell. A metal wall placed at the periphery can however confine higher-order modes with the dipole structure (figure 4-3(a)). For $a/b > 0.2$ the PBG structure confines higher-order the $TM_{11}-$ like mode (figure 4-3(b)), and is not anymore attractive for accelerators, because, the TM_{11} mode is a dangerous wake. Alongside with the longitudinal component, the electric field in the TM_{11} mode has the transverse component, and thus, the dipole mode is primarily responsible for kicking the electron beam off axis.

The question which still must be answered is if the dipole mode confined by the metal wall is a dangerous wake mode. The intuitive answer is "no" because this mode is spread over the big volume of the cavity. The quantitative answer can be given by employing the concept of "wake potential", which is the characteristic of the wakefield "danger" for a beam.

TM$_{01}$ TM$_{11}$

(a) a/b = 0.15

TM$_{01}$ TM$_{11}$
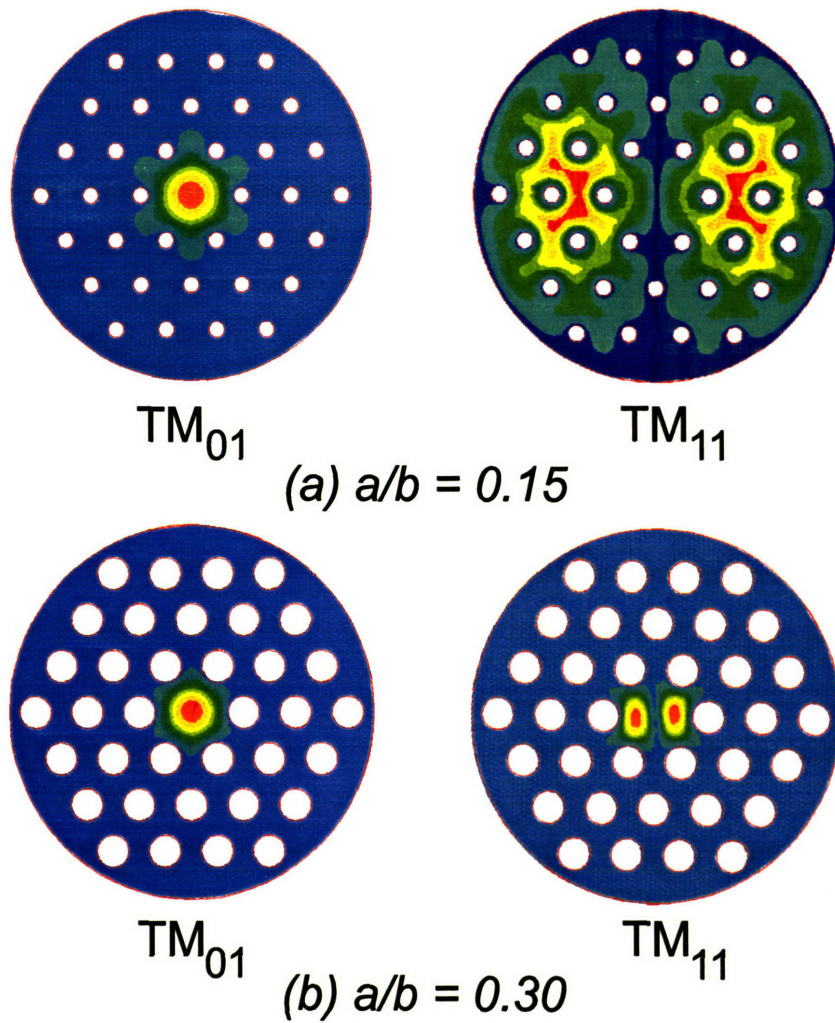
(b) a/b = 0.30

Figure 4-3: Modes of PBG resonators with different ratios of a/b: (a) $a/b = 0.15$, the TM$_{01}$ mode confined by PBG structure, the TM$_{11}$ mode confined by the outside wall; (b) $a/b = 0.30$, the TM$_{01}$ and the TM$_{11}$ modes confined by PBG structure.

63
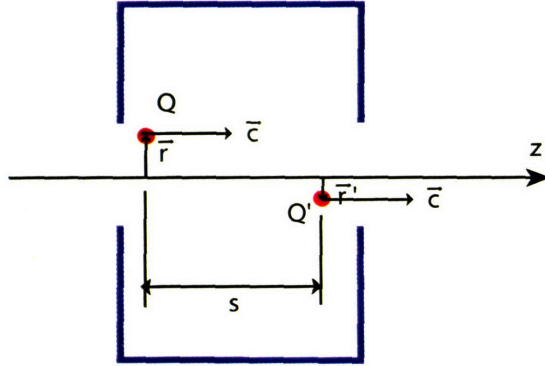
Figure 4-4: An exciting charge Q' moving parallel to the $z-$ axis at the transverse position $\vec{r'}$. A test charge Q moving parallel to the $z-$ axis at transverse position $\vec{r}$ and longitudinal position s behind Q'.

4.3 Wake potentials

There are two types of wake potentials, which scientists do define [4]. Both of them describe the effect of the field excited by one charge Q' moving through the cavity on the test charge Q entering the cavity and separated from the first charge by a distance s. The charges are moving along the parallel paths (take those paths to be parallel to the $\hat{z}$-axis). The transverse coordinate of the first charge is $\vec{r'}$ and of the second charge is $\vec{r}$ (see figure 4-4).

The delta-function longitudinal wake potential is defined as the total voltage, lost by a test charge following at $v = c$ at a distance s on the parallel path, divided by Q'. Thus

$$W_z\left(\vec{r'}, \vec{r}, s\right) = -\frac{1}{Q'} \int_0^L E_z^{r'}\left(\vec{r}, z, t = \left(s + z\right)/c\right) dz, \tag{4.1}$$

where $E_z^{r'}\left(\vec{r}, z, t\right)$ is the z-component of the electric field due to the exciting charge, L is the length of the cavity. Note, that since a signal cannot travel faster than the speed of light $W_z = 0$ for $s < 0$ (causality). The usefulness of this definition is that W_z can be used as a Green's function for computing the voltage loss within an ultrarelativistic bunch of arbitrary shape.

The delta-function transverse wake potential is defined as the transverse momentum kick experienced by a test charge Q following the first charge Q' at $v = c$ at a

distance s on the parallel path, divided by Q'. Thus

$$\vec{W}_\perp (\vec{r}', \vec{r}, s) = \frac{1}{Q'} \int_0^L \left[\vec{E}_\perp^{r'} (\vec{r}, z, t) + \left(\vec{v} \times \vec{B}^{r'} (\vec{r}, z, t) \right)_\perp \right]_{t=(z+s)/c} dz. \qquad (4.2)$$

where $\vec{E}_\perp + \left(\vec{v} \times \vec{B} \right)_\perp$ is the perpendicular component of the Lorenz force affecting the test charge due to the fields created by the first charge. Note, that $\vec{W}_\perp$ is a vector with both x and y components.

It is shown in [4] and also reproduced in Appendix A, that in the cavity with translational symmetry the following expressions are valid for W_z and $\vec{W}_\perp$:

$$W_z (\vec{r}', \vec{r}, s) = \sum_\lambda \frac{1}{2U_\lambda} V_\lambda (\vec{r}) V_\lambda^* (\vec{r}') \cos \frac{\omega_\lambda s}{c} \begin{cases} 0, & s < 0 \\ \frac{1}{2}, & s = 0 \\ 1, & s > 0 \end{cases}, \qquad (4.3)$$

$$\vec{W}_\perp (\vec{r}', \vec{r}, s) = \sum_\lambda \frac{c}{2U_\lambda \omega_\lambda} V_\lambda^* (\vec{r}') \left(\vec{\nabla}_\perp V_\lambda (\vec{r}) \right) \sin \left(\frac{\omega_\lambda s}{c} \right) \begin{cases} 0, & s \leq 0 \\ \\ 1, & s > 0 \end{cases}, \qquad (4.4)$$

where the sum is taken over all the eigenmodes of the cavity numbered with an index λ, and ω_λ is the frequency of mode λ, U_λ is the energy stored in the mode λ,

$$V_\lambda (\vec{r}) = \int_0^L dz \exp (-i\omega_\lambda z/c) E_{\lambda z} (\vec{r}, z), \qquad (4.5)$$

$\vec{E}_\lambda$ is the electric field in mode λ. For the short cavity $\omega_\lambda L/c \ll 1$ $V_\lambda (\vec{r}) \simeq E_{\lambda z} (\vec{r}) L$.

In case of a real accelerator cavity with finite conductivity the fields excited by the first charge decay with time. Thus the impact of these fields on the test charge will be smaller than that given by (4.3) and (4.4). The correction is introduced to the definition of wakefield potentials for the case of the cavity with finite conductivity [26]:

$$W_z (\vec{r}', \vec{r}, s > 0) = \sum_\lambda \frac{1}{2U_\lambda} V_\lambda (\vec{r}) V_\lambda^* (\vec{r}') \cos \frac{\omega_\lambda s}{c} e^{-\frac{\omega_\lambda s}{2cQ_\lambda}}, \qquad (4.6)$$

$$\vec{W}_\perp\left(\vec{r}', \vec{r}, s > 0\right) = \sum_\lambda \frac{c}{2U_\lambda \omega_\lambda} V_\lambda^*\left(\vec{r}'\right) \left(\vec{\nabla}_\perp V_\lambda\left(\vec{r}\right)\right) \sin\left(\frac{\omega_\lambda s}{c}\right) e^{-\frac{\omega_\lambda s}{2c Q_\lambda}}, \qquad (4.7)$$

where Q_λ is the quality factor of the mode λ.

4.4 The dipole mode suppression in a PBG cavity

Even if the PBG structure is finite and surrounded by a metal wall, the cavity still has lower wakefields, than the conventional pillbox cavity. The reason for this is that the HOMs of a PBG cavity are not confined inside of the lattice defect, but rather are be spread out over the volume. The number of these eigenmodes per some frequency interval is proportional to the square of the radius of the metal wall R_{wall}^2 and increases as we add the additional rows of rods. Meanwhile, the energy, stored in each mode is also proportional to R_{wall}^2 and the characteristic scale of a mode $|E_{z\lambda}| / \left|\vec{\nabla}_\perp E_{z\lambda}\right|$ is proportional to R_{wall}. Thus as long as only the accelerating mode is confined by the PBG structure, the overall transverse wake field potentials of the PBG cavity will scale as $W_\perp \propto 1/R_{wall}$. Among all the higher order modes, only the number proportional to R_{wall} will have zero angular field variation and non-zero electric field on the beam axis. Only this modes contribute to the longitudinal wake potential. Thus the longitudinal wake potential will also scale with the cavity radius as $W_z \propto 1/R_{wall}$.

However, when a higher order mode is nearly confined by PBG structure (as it happens for the $\text{TM}_{11}-$ like mode in a defect of a triangular lattice with $a/b \sim 0.2$) the above scaling is not correct at the presence of the wall at the periphery. And we cannot say that the PBG cavity with just three rows of rods will have low wakefields up to the the rods radii $a = 0.2b$. The figure 4-5 shows the TM_{11}-like mode in PBG cavities with different ratios of a/b. It can be seen from the picture, that though the TM_{11}-like mode is not confined by the PBG lattice for $a/b < 0.2$, the metal wall still pushes the mode inside the defect.

Meanwhile it is strongly desirable to have the biggest possible ratio of a/b. The bigger a/b is, the lower are the peak fields in the cavity and the lower are losses and
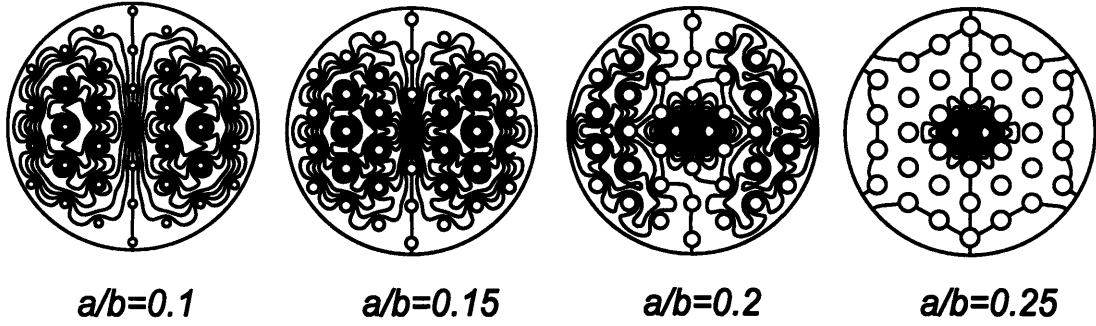
Figure 4-5: The TM_{11}-like mode with vertex polarization in PBG cavity with triangular lattice and three rows of rods for different ratios of a/b.
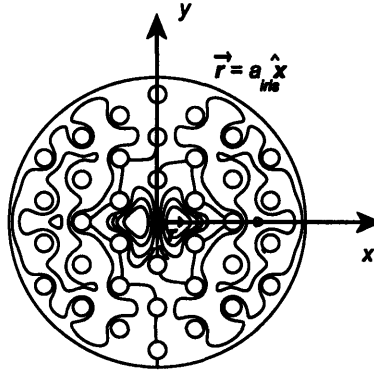
Figure 4-6: The direction of $\hat{x}-$ and $\hat{y}-$axes and characteristic $\vec{r}$ in evaluation of the wake potential for the TM_{11} mode.

the higher is the ohmic quality factor Q_w and the higher is the breakdown limit. So it is important to know how big can the rods be without having strong wakefields in the cavity. Consider the part of the perpendicular wake potential related to the TM_{11}-mode. The maximum wake potential due to the TM_{11} mode will be achieved for the distance between the charges $s = \frac{\pi c}{2\omega_{11}}$ and is equal to

$$\vec{W}_\perp^{11}(\vec{r}',\vec{r}) = \frac{c}{2U_{11}\omega_{11}} V_{11}^*(\vec{r}') \left(\vec{\nabla}_\perp V_{11}(\vec{r})\right). \tag{4.8}$$

To make an estimate for the value of $W_\perp^{11}$ we need to choose some characteristic values for the charge offsets from the axis. Recall, that a real accelerator structure
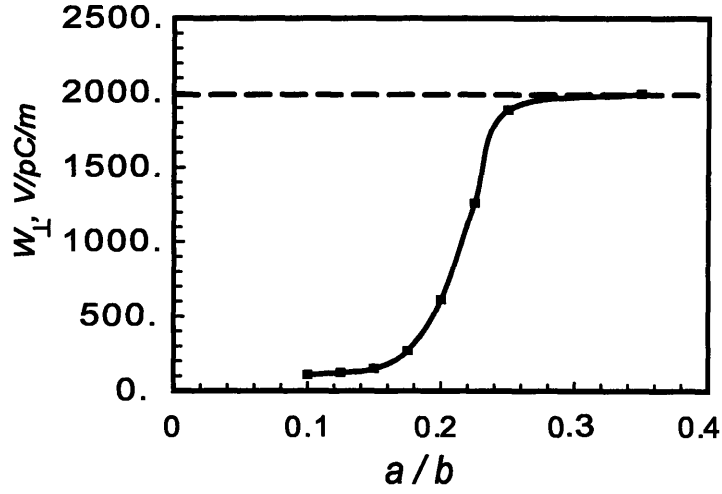
Figure 4-7: The wake potential per unit length $w_\perp^{11}$ due to the $TM_{11}-$ like mode in a PBG cavity with three rows of rods as a function of the ratio a/b. The straight line denotes the value of $w_\perp^{11}$ in a pillbox cavity.

consists of a stack of cavities set between the disks with the beam holes (irises), inserted on axis (see figure 1-7). The maximum possible offset of the beam from the axis is therefore the axis radius a_{iris}. So it looks reasonable to evaluate $\vec{W}_\perp^{11}$ at $|\vec{r}'| = |\vec{r}| = a_{iris}$. Consider a short cavity so that we can assume that $V_{11}(\vec{r}) \approx E_{z11}(\vec{r}) L$. The contours of the electric field in the TM_{11}-like mode are shown in figure 4-6, and the field grows the most quickly in direction of $\hat{x}-$ axis. So let evaluate $\vec{W}_\perp^{11}$ at $\vec{r}' = \vec{r} = \hat{x} a_{iris}$. The E_{z11} increases linearly from the center of the cavity in $\hat{x}-$direction, so we can write approximately that

$$\vec{\nabla}_\perp E_{z11}\left(\hat{x} a_{iris.}\right) \approx \frac{E_{z11}\left(\hat{x} a_{iris.}\right)}{a_{iris.}} \hat{x}, \tag{4.9}$$

and so the wake potential due to TM_{11} mode per unit length is equal to

$$\vec{w}_\perp^{11} = \frac{c E_{z11}^2 \left(\hat{x} a_{iris.}\right)}{2 u_{11} \omega_{11} a_{iris.}} \hat{x}, \tag{4.10}$$

where u_{11} is the energy stored in the $TM_{11}-$like mode per unit length of the cavity.

The figure 4-7 shows the results of SUPERFISH [24] calculations of $w_\perp^{11}$according

68

to the formula (4.10) for PBG cavities with three rows of rods and different ratios of a/b. The straight line in the picture shows the value of $w_\perp^{11}$ in a pillbox cavity. It can be seen, that $w_\perp^{11}$ in a PBG cavity is always smaller than $w_\perp^{11}$ in a pillbox cavity. But if we want to achieve a really good suppression of the wakefields, we need to keep the ratio of a/b as low as 0.15.

The wakefields in PBG cavity with $a/b = 0.15$ can be suppressed further, if a lossy material is placed at the periphery of the cavity or the metal wall is completely removed. Then the modes, which are not confined by the lattice, will have much lower $Q-$factors, than the accelerating mode. And the wake potentials given by (4.6) and (4.7) will be small. This will be realized in the experiment.

4.5 First PBG resonators fabrication and the proof-of-principal cold test

In order to verify experimentally the mode confinement and HOM suppression in PBG resonators, we constructed two PBG resonators for cold testing (figure 4-8). The resonators were fabricated using the brass cylinders closed at each end by brass circular plates. PBG structures were formed by brass rods fitted into arrays of holes at the endplates. A single rod was missing from the center of a PBG structure to form a PBG resonator. The parameters of resonators are summarized in Table 4.1. In Cavity 1, only the TM_{01} mode was confined by the PBG structure and in the Cavity 2 the TM_{01} and the TM_{11} modes were confined. Cavities 1 and 2 were designed so that the frequencies of the TM_{01} modes were the same. WR62 waveguides were employed to feed rf power into the cavities, and the same size waveguides were connected symmetrically on the opposite sides.

To couple the power into a PBG resonator several rods in front of the waveguides were removed. Several coupling schemes were tried. The coupling scheme finally used in the experiment is shown in figure 4-9. The removed rods are shown in figure 4-9 with hollow circles. PBG structure rods are shown with filled circles. We measured
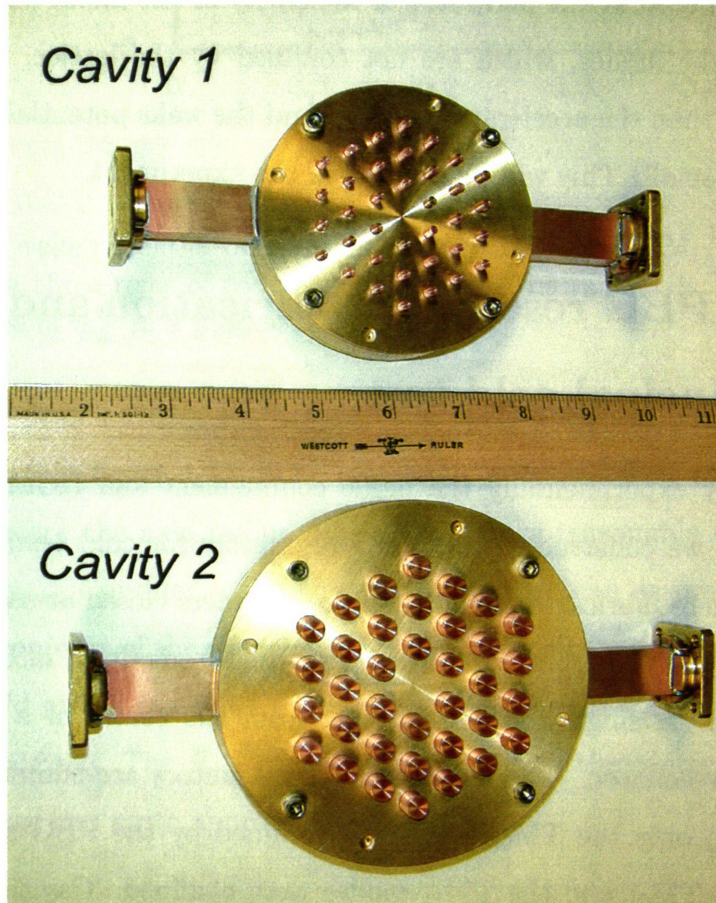
Figure 4-8: PBG resonators built for the cold test.

the S_{12} (transmission) elements of the scattering matrix using the HP8510 vector network analyzer. First, we did not place an absorber at the metal walls of the cavities and thus the eigenmodes of the PBG resonator as well as the eigenmodes of the metal wall resonator were confined. The coupling curves for two resonators are shown in figure 4-10 (higher graphs). Then we placed the eccosorb at the periphery of the cavities, which reduced by a factor of 10 the Q–factors of the modes not confined by the PBG structure as well as increased the frequencies of these modes (figure 4-10, lower graphs). Only the TM_{01} mode at 11 GHz survived in Cavity 1. Both, the TM_{01} mode at 11 GHz and the TM_{11} mode at 17 GHz, survived in Cavity 2 because of thicker rods and wider band gap. These results agree with the cavities design. We also measured the S_{11} (reflection) elements of the scattering matrices and derived from those that the ohmic Q–factors for the TM_{01} modes in both cavities were about 2000.

Table 4.1: The parameters of two PBG cavities constructed for the cold test.

Parameter	Cavity 1	Cavity 2
Lattice vector	1.06 cm	1.35 cm
Rod radius	0.16 cm	0.4 cm
a/b	0.15	0.3
Cavity radius	3.81 cm	4.83 cm
Eigenfrequency of the TM_{01} mode	11 GHz	11 GHz
Eigenfrequency of the TM_{11} mode	15.28 GHz	17.34 GHz
Cavity length	0.787 cm	0.787 cm

4.6 High Q PBG resonator fabrication and testing

Although the first cold tests successfully demonstrated the confinement of modes in PBG resonators, we observed a big discrepancy between the measured Q-factors of
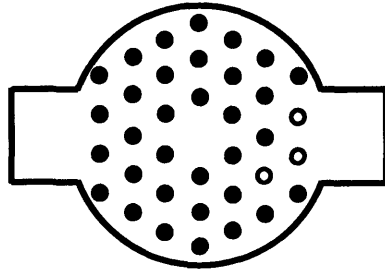
Figure 4-9: Coupling scheme for the PBG resonator. PBG structure rods are shown with filled circles. Missing rods are shown with hollow circles.
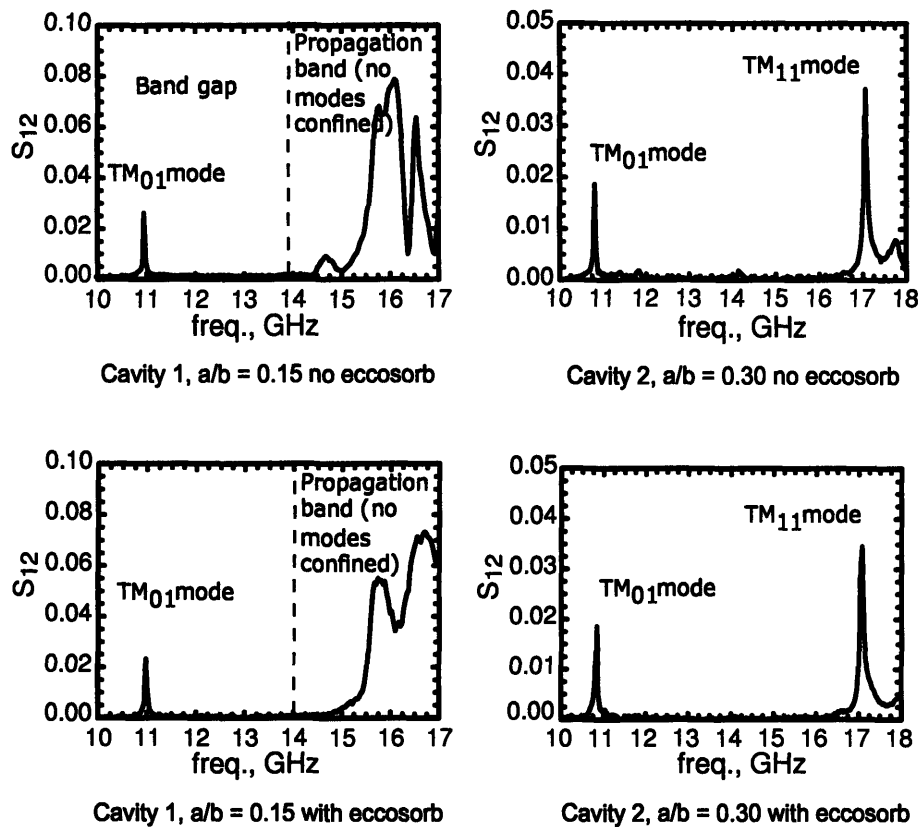
Figure 4-10: Cold test measurements of the transmission coefficient S_{12} for the brass resonators Cavity 1 and Cavity 2.
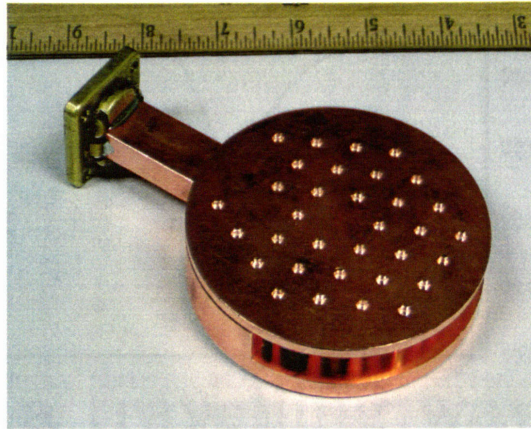
Figure 4-11: Brazed PBG resonator.

the resonators' modes and the theoretically calculated Q_w of 5500. We suggested that the reason for low Q_w was the poor contact between the rods and the end plates. The currents going from the rods onto the plates were broken at the gaps in between rods and plates and big losses occurred. To improve the connection between rods and plates and decrease losses the the rods were brazed into the plates. A new PBG resonator with the dimensions of Cavity 1 was fabricated. Brass is not suitable for brazing, thus the rods and the plates were now machined of high purity oxygen-free Class 1 copper. Communication Power Industries (CPI) [27] engineers put brazing material in the gaps between the rods and the plates and then heated the structure in a hydrogen furnace. The brazing material melted and good electrical connection was made. The brazed resonator (figure 4-11) was cold-tested. The reflection, S_{11}, curve for the brazed resonator is shown in Figure 4-12. The TM_{01}-mode $Q-$ factor of 5000 was calculated from the S_{11}-curve. This is in excellent agreement with theory.

In addition to brazing, one more improvement was made to the resonator design. Half of the outer wall was removed to obtain the HOM damping. The other half of the wall had to stay in place for the coupling. Since the measured Q was high we concluded that the removal of the wall did not affect the TM_{01} mode confinement. This is in agreement with theory. Removing a part of the wall also allowed us to tune the frequency of the the TM_{01} mode by deforming the rods of the inner row. A fishing
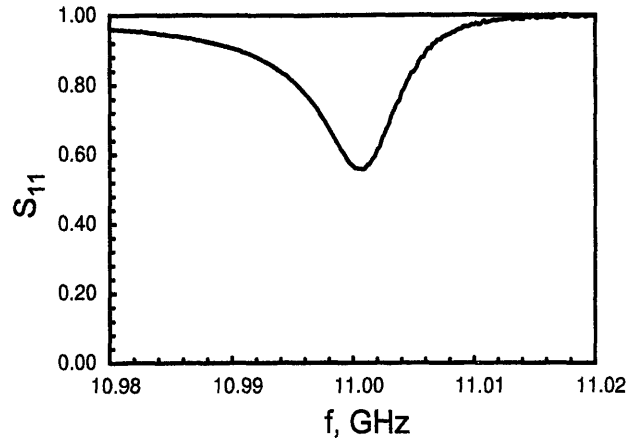
Figure 4-12: Cold test measurements of the reflection coefficient, S_{11}, for the brazed PBG resonator.

line was wrapped around the inner row rod and pulled, the rod was slightly bent. As a result of the deformation, the frequency of the TM_{01} mode was tuned from 11.010 GHz to 11.000 GHz.

Chapter 5

Design of a travelling wave PBG accelerator

5.1 Introduction

In the previous chapter we demonstrated several PBG resonators and proved the mode confinement in PBG structures and HOM damping. Next, we want to demonstrate the acceleration in a PBG structure. The accelerating structure will be a disk-loaded PBG waveguide of the form shown in figure 5-1. The six-cell structure consists of two coupling cells (with waveguides) and four travelling wave (TW) cells. We would like to construct a disk-loaded PBG waveguide, couple power into it and accelerate the electrons. The available power is at the frequency of 17.137 GHz and is produced by the Haimson Research Corporation (HRC) klystron [28]. The 10 MeV electron beam is produced by the HRC accelerator [29] and will enter the PBG accelerator at the speed of light c. The electromagnetic wave must be in resonance with the electron beam and thus must have the phase velocity equal to c. The complete design of the travelling wave PBG accelerator must determine the following parameters: the rod radii a, the spacing between the rods b, the cell length L, the optimal phase shift per cell φ, the iris thickness t, the iris opening diameter $2d$ (see figure 5-1). In addition, the coupler cell must be designed separately. The coupling scheme (number of removed rods) must be chosen first. Next, the radii of the rods and the spacing
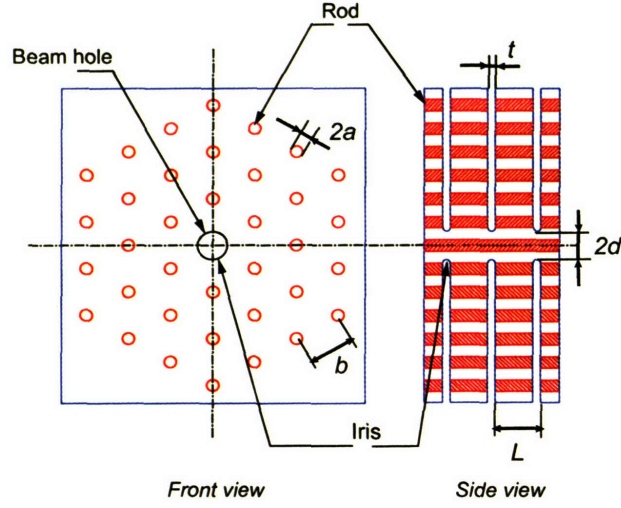
Figure 5-1: Disk-loaded PBG waveguide.

between the rods must be determined separately for the coupling cell.

The cell length L, the optimal phase shift per cell ϕ, the iris thickness t, and the iris opening diameter $2d$ are determined by the following designer's goal. One would like to have a structure with high shunt impedance, low losses, short filling time and the beam hole big enough to accept the beam and do not produce short-range wakefields [30]. *Short-range wakefields* are the terraherz radiation produced due to the beam interaction with the close metallic surface of the irises. Although the problem of short-range wakefields is crucial for real-world high brightness accelerator, in our experiment it would not arise due to low electron bunch charge in the HRC accelerator [29]. Thus the short-range wakefields are of no concern in our design. The *shunt impedance* is the measure of the efficiency of the accelerator structure. It is defined as the square of the energy gained by an electron for unit RF power dissipation in the structure:

$$R_s = \frac{\left(\int_0^L E_z\left(r=0,s\right)\cos\omega\frac{s}{c}\mathrm{d}s\right)^2}{P_w}, \tag{5.1}$$

where $E_z\left(r=0,s\right)$ is the $z-$ component of the on-axis electric field amplitude in accelerator at the longitudinal point s, ω is the accelerating wave frequency, and P_w

76

is the Ohmic loss power in the accelerator structure. The shunt impedance is usually normalized to the the structure quality factor $Q_w = \omega W / P_w$:

$$\left[\frac{R_s}{Q_w} \right] = \frac{\left(\int_0^L E_z \left(r = 0, s \right) \cos \omega \frac{s}{c} \mathrm{d}s \right)^2}{\omega W},$$ (5.2)

where W is the power stored in a single accelerator cell. $\left[\frac{R_s}{Q_w} \right]$ is a measure of geometric accelerating properties of the structure, independent of the cell's material properties and the frequency. The ratio of $\left[\frac{R_s}{Q_w} \right]$ is the best characteristics of the accelerating properties of the cavity.

First, let us choose the optimal phase shift per cell ϕ. The resonance condition for the electron and the wave requires that

$$\frac{\omega L}{c} = \phi.$$ (5.3)

To increase the efficiency of the acceleration, one must maximize the shunt impedance per unit length, R_s/L. The shunt impedance of the individual cavities is improved by increasing the length of the cavities, i.e. increasing ϕ (see [5]). However, the radio of R_s/L has an optimal value. For small iris thickness $t \ll L$, the value of ϕ maximizing the shunt impedance per unit length was found to be around $2\pi/3$ [5]. The cell's length is then determined by the relationship (5.3).

Next, let us determine the optimal iris thickness t and the iris opening diameter $2d$. Decreasing the iris opening increases the cell's shunt impedance. However in our case the dimension of the iris opening is limited from below by the radius of the electron beam which is about 1 mm. A thicker iris has higher mechanical strength and lower probability of breakdown, but decreases the shunt impedance. Increasing the iris thickness and decreasing the opening decreases the group velocity of the wave and increases filling time. Shorter portion of the klystron pulse is then available for the acceleration of electrons. We determined that the dimensions of the Stanford Linear Collider [5] scaled to 17.137 GHz will work well for our experiment. We chose $d = 2.16$ mm and $t = 1.14$ mm. We estimated that the structure with these

dimensions will accelerate the electron beam by approximately 1 MeV if fed by 2 MW of power available from the klystron. This energy increase in a 10 MeV electron beam is easy to measure with a spectrometer.

Finally, the rod radii a and the spacing between the rods b must be adjusted to bring the cell's frequency to 17.137 GHz. Each parameter can be varied to change the frequency. However, it is desirable to keep the ratio $a/b \approx 0.15$ for good HOM damping and higher Q_w. The exact values of a and b are different for the coupler cells and for the TW cells. First, a and b of the coupler cell were chosen through tuning the coupler cell's dimensions for the optimal coupling. Next, the spacing between the rods b was fixed the same for all the cells and the radii of the rods inside the TW cells were determined to tune the frequency.

5.2 Coupling into a travelling wave structure: properties and tuning algorithms

This section describes different algorithms of the coupler tuning and explains which tuning algorithm works the best in our case. Coupling into a travelling wave structure is more complicated than coupling into a resonator. A resonator confines a mode of a particular frequency. Only this frequency can be coupled into the resonator. The coupling iris diameter is varied to achieve zero reflection from the resonator. This is called "critical coupling". The travelling wave structure is different: it has a bandpass and resonates at the whole band of frequencies (see Appendix B). If a coupler is attached to the travelling wave structure, the coupling curve will have a minimum at some frequency $\omega = \omega_m$, which can be different from the desirable frequency ω_0. To achieve the critical coupling two conditions must be satisfied: the minimum of the reflection must be zero and must be achieved at $\omega = \omega_0$. These two conditions cannot be satisfied with varying just one parameter of the coupler. In addition to the coupling iris diameter the diameter of the coupling (first) cell must be modified to achieve the critical coupling. Thus, the tuning algorithm must be invented, which

will help us to choose the correct values for the coupling iris diameter and the size of the coupling cell.

The HFSS code was applied for the coupler design. The first computational algorithm, which we tried, was proposed by Ng and Ko [31]. This algorithm is described in details in Appendix C. The algorithm works well for the pillbox couplers. However the design of PBG coupler is more complicated and requires more computations. In PBG coupler design the drawbacks of the Ng and Ko methods start to arise. The drawbacks are the following:

- The reflection from Ng and Ko structure is not directly related to the reflection from the coupler (see figure C-4). The calculated reflection is a result of two coupler interference.

- There is no convergence criteria in the method.

- The convergence of HFSS computations slows as the reflection coefficient approaches zero.

An alternative algorithm was proposed by Kroll [32]. This algorithm allows to compute the reflection from a single coupler and thus does not have the above drawbacks. The idea of the method is the following. Assume we have an accelerator structure of $N \gg 1$ identical cells. At the end of the structure there is some reflection (from the coupler). The field profile in the structure then allows us to calculate the reflection from the coupler.

Away from the coupler all evanescent bands are absent. The Floquet theorem must be valid and the two travelling waves (the forward and the reverse) must exist

$$
\begin{aligned}
E\left(z\right) &= E_a\left(z\right)\left[e^{-j\varphi(z)} + R\,e^{j\varphi(z)}\right], & (5.4)\\
E_a\left(z \pm L\right) &= E_a\left(z\right),\; \varphi\left(z \pm L\right) = \varphi\left(z\right) \pm \phi,
\end{aligned}
$$

where R is the reflection from the coupler, ϕ is the phase advance per cell (in our

case $\phi = 120^0$), and z is the coordinate along the accelerator. Then

$$\begin{cases} E\left(z+L\right) = E_a\left(z\right)\left[e^{-j\varphi(z)-j\phi} + R\ e^{j\varphi(z)+j\phi}\right] \\ E\left(z-L\right) = E_a\left(z\right)\left[e^{-j\varphi(z)+j\phi} + R\ e^{j\varphi(z)-j\phi}\right] \end{cases}. \tag{5.5}$$

Introduce

$$\begin{cases} F^+\left(z\right) = \frac{E(z+L)}{E(z)} = \frac{e^{-j\varphi(z)-j\phi}+R\ e^{j\varphi(z)+j\phi}}{e^{-j\varphi(z)}+R\ e^{j\varphi(z)}} \\ F^-\left(z\right) = \frac{E(z-L)}{E(z)} = \frac{e^{-j\varphi(z)+j\phi}+R\ e^{j\varphi(z)-j\phi}}{e^{-j\varphi(z)}+R\ e^{j\varphi(z)}} \end{cases}, \tag{5.6}$$

$$\Sigma\left(z\right) = F^+\left(z\right) + F^-\left(z\right) = \frac{2e^{-j\varphi(z)}\cos\phi + 2R\ e^{j\varphi(z)}\cos\phi}{e^{-j\varphi(z)} + R\ e^{j\varphi(z)}} = 2\cos\phi,$$

$\phi = arc\cos\left(\Sigma/2\right)$, which means that Σ must be independent of z. Independence Σ of z yields the convergence criteria for the Kroll's method. The adaptive HFSS mesh must be refined until the solution has Σ, which independent of z, or $\phi \equiv 120^0$. Next introduce

$$\Delta\left(z\right) = F^+\left(z\right) - F^-\left(z\right) = \frac{-2je^{-j\varphi(z)}\sin\phi + 2jR\ e^{j\varphi(z)}\sin\phi}{e^{-j\varphi(z)} + R\ e^{j\varphi(z)}},$$

$$R\ e^{2j\varphi(z)} = \frac{2\sin\phi - j\Delta\left(z\right)}{2\sin\phi + j\Delta\left(z\right)}, \tag{5.7}$$

$$|R| = \left|\frac{2\sin\phi - j\Delta\left(z\right)}{2\sin\phi + j\Delta\left(z\right)}\right|.$$

The reflection from the coupler can be computed from the field profile, calculated with HFSS, using the equations 5.7.

The Kroll's algorithm was first tried for the pillbox coupler design (see Appendix D) and then employed for the PBG coupler design.

5.3 PBG coupler design with Kroll's method

I chose the geometry of figure 5-2 to start the HFSS simulations of the coupler. The goal of the simulation was to tune the PBG coupler, so that no reflection occurs from the structure consisting of PBG cells. To speed up the calculation, I tried to replace
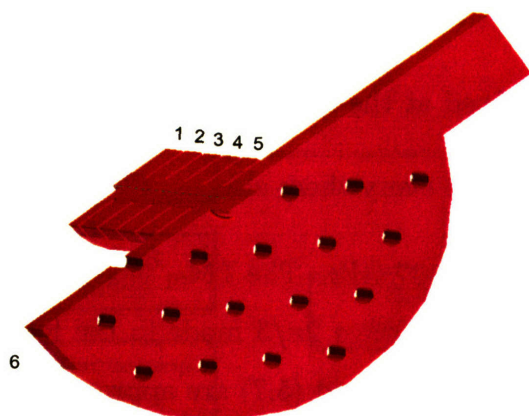
Figure 5-2: HFSS modelling geometry for the PBG coupler tuning with Kroll's method.
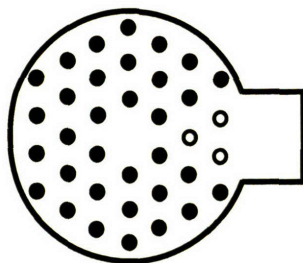
Figure 5-3: Coupling scheme for the PBG coupler of a travelling wave PBG accelerator.

the PBG TW cells with pillbox cells.

At first, I discovered that a pillbox cell has slightly higher group velocity than the PBG cell with the same irises. However, in simulations I needed a pillbox cell which would have the same dispersion as my PBG cell. To achieve this, I made the irises of a pillbox cell 0.04 mm thicker than the irises of my PBG cell. I chose the coupling scheme of figure 5-3 for my coupling PBG cell. Then I made the following definitions for the boundaries:

- A port was created at the cell #1. The TM_{01} mode of a cylindrical waveguide was excited through the port.

81

- The matching load was placed at the end of the waveguide of the coupler cell #6.

- H-boundary was defined at the symmetry plane.

- E-boundary was defined everywhere else.

The port was excited at 17.137 GHz. The TM_{01} mode at cell #1 would couple with some reflection into a travelling wave $2\pi/3$ mode in the following cells. In cells #3 and #4 the Kroll's formulaes (5.6) and (5.7) are approximately valid. The reflection coefficient was calculated from the field profile in cells #3 and #4 using the equations (5.7). The parameters of the coupler cell, the rod's radii a and the distance between the rods b, were then varied to minimize the reflection coefficient. A C++ subprogram was written for this optimization. The C++ subprogram followed the flow chart of figure 5-4.

The optimization program ran for approximately 24 hours. The coupler was tuned to the low reflection of $|R| = 0.012$. The coupler parameters were found as following: the rod radius $a = 1.05$ mm, the distance between the rods $b = 6.97$ mm.

The magnitude of the electric field in a tuned structure is shown in color in figure 5-5. Figure 5-6 shows the on-axis distribution of the electric field magnitude. The field profile looks flat, which means that the coupler is tuned. The reflection coefficient, calculated using the equations (5.7) in different points of the structure on-axis is shown in figure 5-7. The phase shift per cell, calculated using the equations (5.6) in different points of the structure on-axis is shown in figure 5-8. The calculated reflection is almost independent of the point, where it is calculated. The phase shift per cell is very close to 120^0 in all the points in cells #3 and #4. This means that the solution converged well and the calculation is correct.

Tolerances, that is, the dependence of $|R|$ on a and b, were also calculated. This dependence is shown in figure 5-9. It can be seen from the picture that the coupler, which has either rods dimensions or the spacing between the rods different from the original by $0.001''$ will have $|R| \sim 0.6$. This means that the tuning of the coupler will be needed after fabrication.
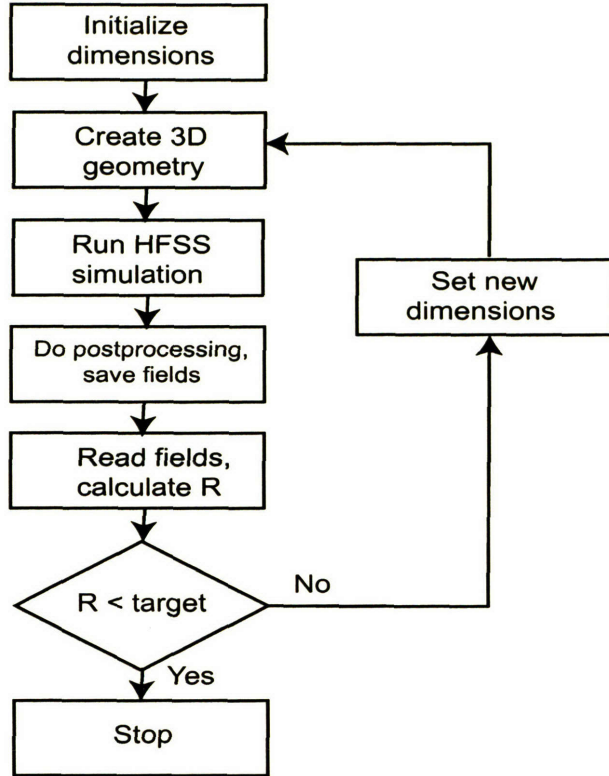
Figure 5-4: Flow chart for the C++ optimization subroutine for the PBG coupler design.
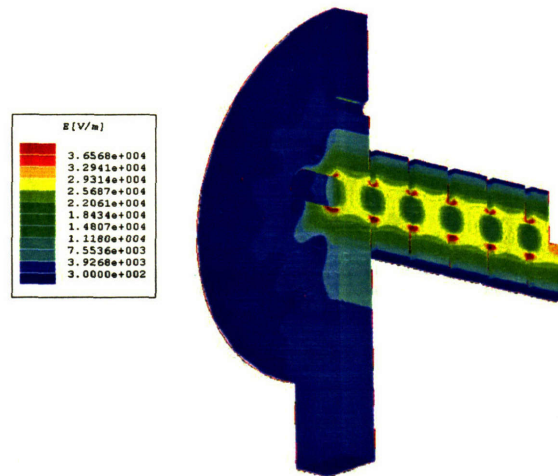
Figure 5-5: Electric field magnitude in a structure with a tuned PBG coupler.
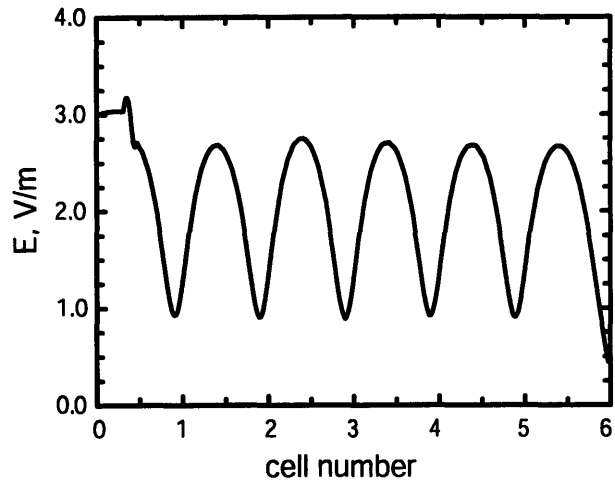
Figure 5-6: The magnitude of electric field on axis of the structure with a tuned PBG coupler.
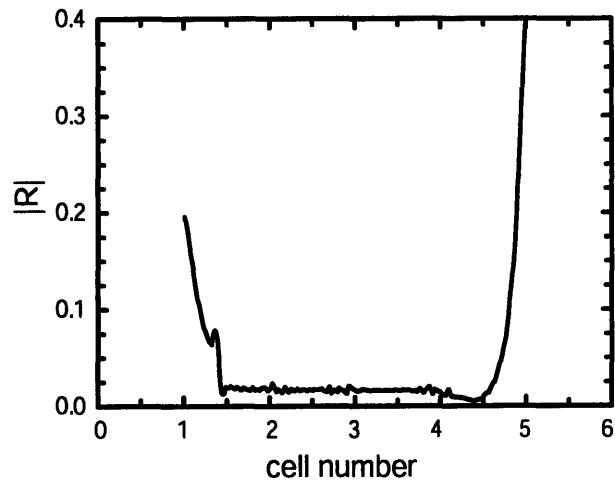
Figure 5-7: The reflection coefficient calculated according to (5.7) in different points of the TW structure.
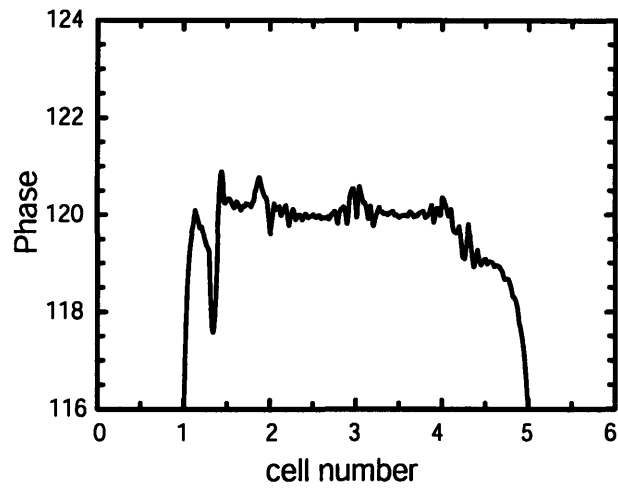
Figure 5-8: The phase shift per cell calculated according to (5.6) in different points of the TW structure.
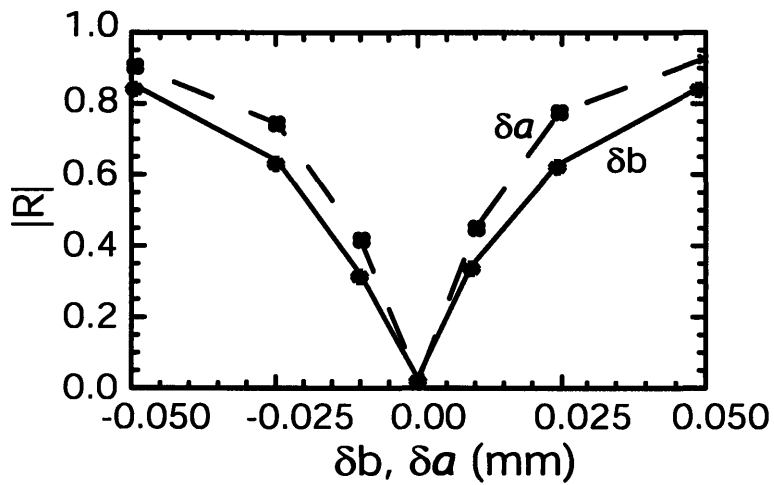
Figure 5-9: The dependence of the reflection from the coupler on the deviation of the rods radius a and the spacing between the rods b from the optimized dimensions.

E[V/m]
4.9000e+03
4.7636e+03
4.6273e+03
4.4909e+03
4.3545e+03
4.2182e+03
4.0818e+03
3.9455e+03
3.8091e+03
3.6727e+03
3.5364e+03
3.4000e+03

(a)   (b)
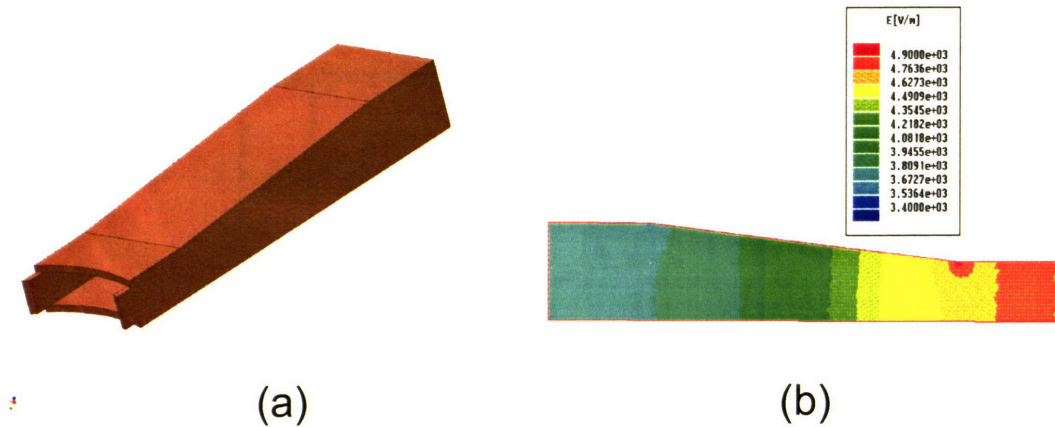
Figure 5-10: The WR62 waveguide to PBG coupler taper (a). Electric field profile in the taper (b).

To complete the design of the coupler, the taper must be made which would increase the size of the coupling waveguide to the size of a standard WR62 waveguide. Generally, each slow taper has low reflection. However, if the taper length is chosen resonant, then the reflection will be minimized. The taper was designed with HFSS. The resonant length of the taper was found to be 5.22 cm. The reflection from a resonant taper was less than 1%. The drawing of the taper and distribution of the electric field in the taper is shown in figure 5-10.

5.4 PBG TW cell design and summary of accelerator dimensions and characteristics

The complete design of a TW PBG accelerator is now lacking only the TW cell design. We have already determined the cell length and the iris dimensions. We choose the distance between the rods to be the same throughout the structure: in coupler cells and in TW cells. The radii of the rods had to be calculated in order to bring the TW cell's frequency to 17.137 GHz. A 30^0 slice of a single PBG cell was modelled with HFSS (figure 5-11). 120^0 phase shift was defined between the upper and the
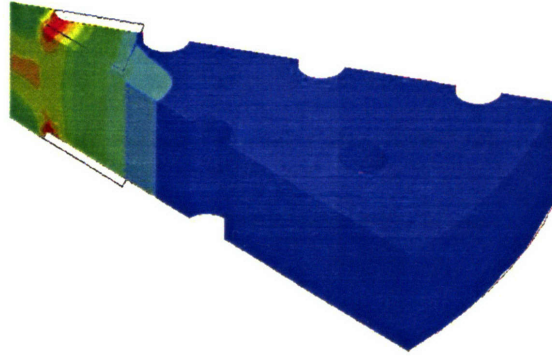
Figure 5-11: The magnitude of electric field for a $2\pi/3$ mode in a PBG cell.
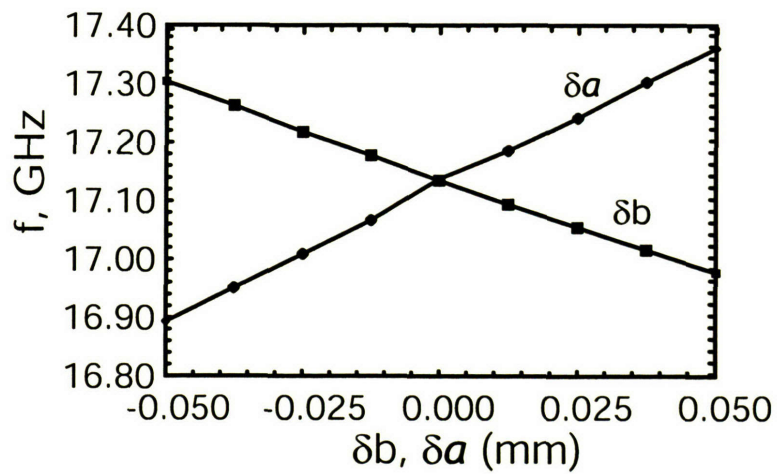
Figure 5-12: The dependence of the TW cell frequency on the deviation of the rods radius a and the spacing between the rods b from the optimized dimensions.
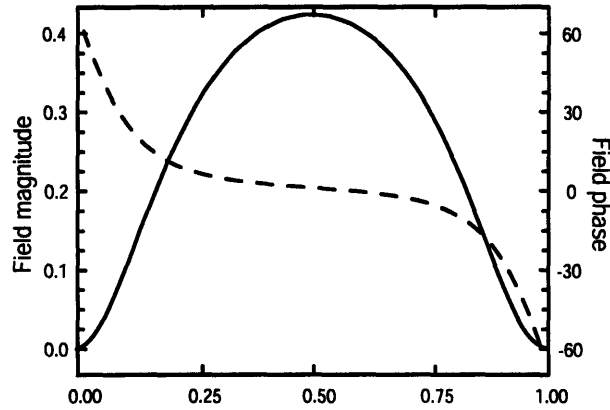
Figure 5-13: The electric field magnitude and phase distribution on axis of a $2\pi/3$ PBG cell.

lower surfaces of the cell. It was found that for the rods radii $a = 1.04$ mm, the cell's frequency was correct. The ratio of a/b in the newly designed cell was found to be 0.155. This means that the wakefields in this cell are suppressed. The electric field profile for the $2\pi/3$ mode in a 30^0 PBG slice is shown in figure 5-11. Figure 5-13 shows the electric field magnitude and phase for the $2\pi/3$ mode on axis of the TW cell. The tolerances were also calculated. The cell's frequency changes as the cell's dimensions vary from the optimized values. The dependence of the cell's frequency on the dimensional variance is shown in figure 5-12. It can be seen from the graph that $0.001''$ deviation in rod radius or in the spacing produces almost 100 MHz frequency shift. Thus, the cell tuning will be required after fabrication.

The dimensions of the travelling wave PBG accelerator are summarized in table 5.1. Table 5.2 summarizes the accelerator characteristics of a disk-loaded PBG waveguide and compares them to the characteristics of a disk-loaded cylindrical waveguide. In table 5.2, r_s is the shunt impedance normalized to the cell length, $r_s = R_s/L$ and gradient is the measure of the effective electric field for given power

$$G = \frac{\int_0^L E_z\,(r = 0, s)\cos\omega\frac{s}{c}\mathrm{d}s}{L}, \tag{5.8}$$

$G \propto \sqrt{P}$, where P is the input power coming from the klystron. Although the

88

PBG disk-loaded structure has lower ohmic Q-factor and consequently, lower shunt impedance, the ratio of $[r_s/Q_w]$ is the same for the PBG and cylindrical disk-loaded waveguides. This means that the accelerating characteristics of the PBG waveguide are similar to those of a cylindrical waveguide. Also, since the PBG disk-loaded waveguide has slightly lower group velocity for the $2\pi/3$ mode than the cylindrical disk-loaded waveguide, the gradient for the PBG structure will be slightly higher for the same input power.

Table 5.1: The dimensions of TW PBG accelerator at 17.137 GHz.

Rod radius (TW cell / coupler cell), a	1.04 mm/ 1.05 mm
Spacing between the rods, b	6.97 mm
a/b	0.155
Cavity length, L	5.83 mm
Phase advance per cell	$2\pi/3$
Iris radius, d	2.16 mm
Iris thickness, t	1.14 mm
Frequency (TM_{01} mode)	17.137 GHz

Table 5.2: Accelerator characteristics: PBG disk-loaded structure vs. disk-loaded cylindrical waveguide.

	PBG disk-loaded structure	Disk-loaded cylindrical waveguide
Frequency	17.137 GHz	17.137 GHz
Q_w	4188	5618
r_s	98 MΩ/m	139 MΩ/m
$[r_s/Q_w]$	23.4 kΩ/m	24.7 kΩ/m
Group velocity	0.013c	0.014c
Gradient	25.2$\sqrt{P\,[\text{MW}]}$ MV/m	25.1$\sqrt{P\,[\text{MW}]}$ MV/m

Chapter 6

Cold test of a TW PBG accelerator

6.1 Introduction

When we had a complete design of a TW PBG accelerator, it was time to proceed with the PBG accelerator construction and testing. The drawings of the structure parts were made by this author with the Autodesk Inventor (figure 6-1) and submitted to the machine shop. We needed to construct a high Q structure with the correct frequency of the $2\pi/3$ mode, correct coupling curve and correct field profile. Although we found that brazing was a successful method of fabrication for a high Q single-cell PBG resonator, it turned out to be a technical challenge to braze a multicell structure. Alternative methods had to be considered. Next, it was expected that the conventional machining with the tolerance of $0.001''$ would not be able to produce the structure with the correct frequency, and consequently, correct coupling and correct field profiles. Tuning was needed. Conventional process of tuning an accelerator section consists of applying an external mechanical pressure which imparts a permanent deformation to the inside wall of the cavity with a frequency different from the design value. For a PBG structure, only the deformation of the inner rods could produce significant frequency shift. However, the inner rods were hard to reach for applying significant mechanical pressure. Also, the diameter of a rod was comparable to the distance between the iris plates. Thus, the deformation of rods without braking the structure was complicated. We had to develop a new tuning method for
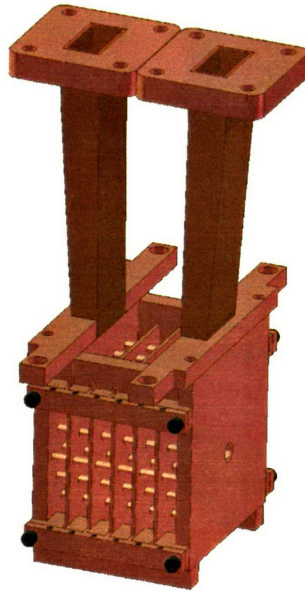
Figure 6-1: Autodesk Inventor drawing of a PBG structure.

the PBG accelerator.

6.2 Computation of the correct coupling curves and field profiles

I applied HFSS to compute the correct coupling curves and the field profiles for a 6-cell accelerator. Two PBG couplers and four TW pillbox cells shown in figure 6-2 were modelled. The pillbox cells dimensions were adjusted so that they would have the same dispersion as the PBG cells. The walls of the structure were made conductive with the conductance $\sigma = 3 \cdot 10^7 \, (\Omega \cdot m)^{-1}$, which is slightly less than the ideal conductance of copper ($\sigma_{ideal} = 5.8 \cdot 10^7 \, (\Omega \cdot m)^{-1}$). The S_{11} and S_{12} coupling curves were computed and plotted (see figure 6-3). It can be seen from the figure, that the S_{11} coupling curve has six distinct dips, which correspond to six eigenmodes of the structure. The eigenmodes have different phase shifts over the length of the structure. The phase shifts and the eigenmode frequencies are summarized in table

91
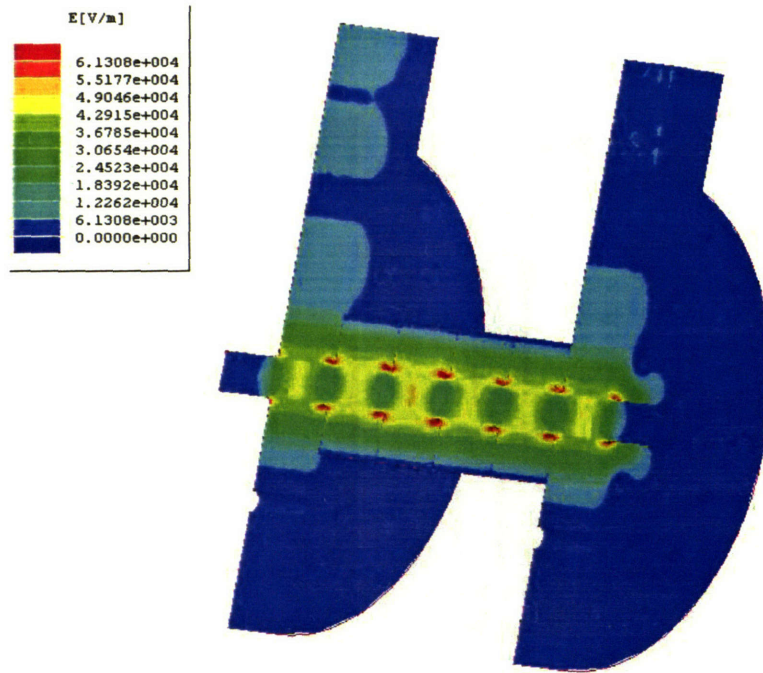
Figure 6-2: The HFSS model of a 6-cell PBG accelerator. The electric field magnitude is shown in color.

6.1. Mode 4 is the one closest to the accelerating $2\pi/3$ mode. I also computed the correct profiles of the electric field on axis of the structure for each eigenmode. The field profiles are plotted in figure 6-4.

Table 6.1: The eigenmodes of a 6-cell PBG accelerator.

	mode 1	mode 2	mode 3	mode 4	mode 5	mode 6
Phase shift per 6 cells	0	π	2π	3π	4π	5π
Frequency, GHz	17.004	17.043	17.090	17.130	17.177	17.218

6.3 Fabrication of the TW PBG accelerator

As it was mentioned above, brazing of a 6-cell PBG accelerator turned out to be complicated. Therefore, our first attempt was to build a PBG accelerator without brazing, just with bolting the parts together. The rods and plates were machined out
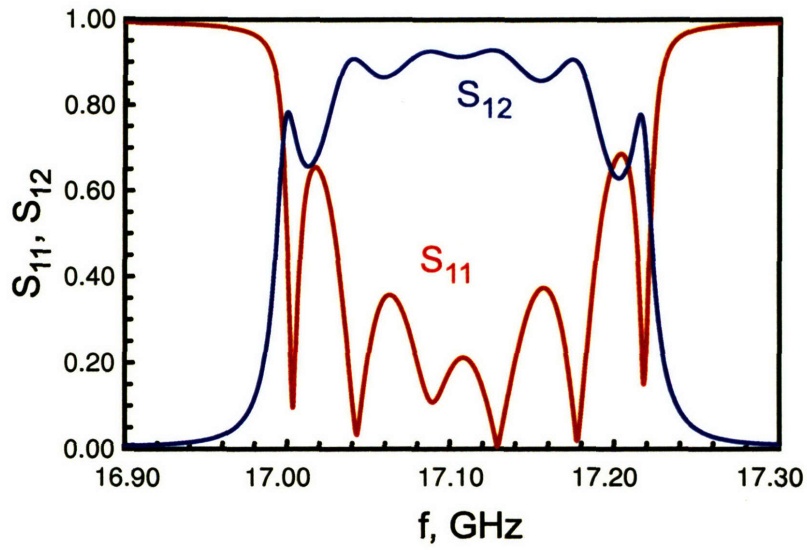
Figure 6-3: Coupling curves for a 6-cell PBG accelerator computed with HFSS.
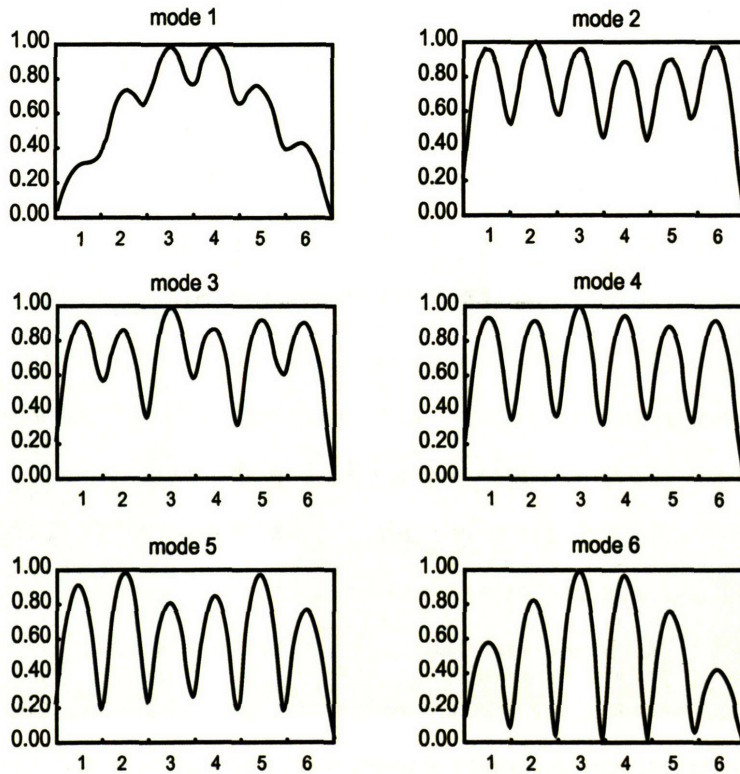
Figure 6-4: Electric field profiles for the eigenmodes of a 6-cell PBG accelerator (HFSS computation).
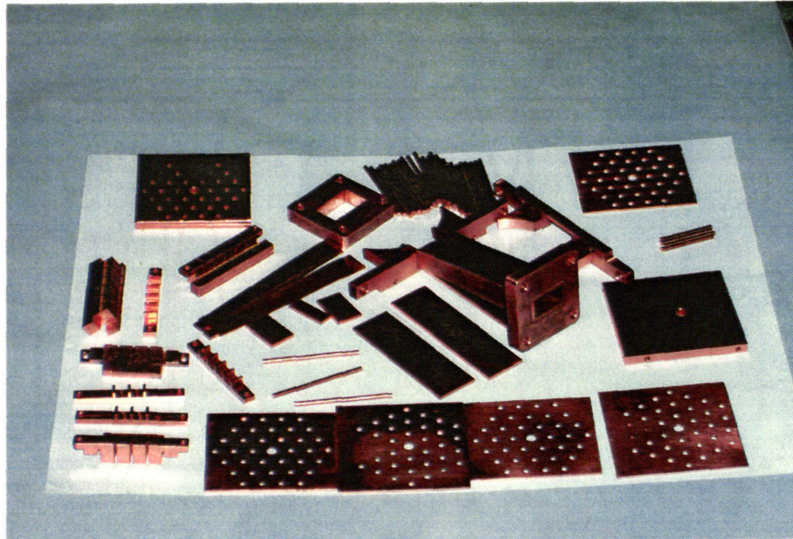
Figure 6-5: Fabricated parts of a 6-cell PBG accelerator.

of class 1 oxygen free electronic (OFE) copper (figure 6-5). The plates were placed in slots of the side pieces and the whole structure was bolted together as shown in figure 6-1. We were hoping that the conductivity of the OFE copper was high enough so that we would be able to obtain the structure with reasonably high Q without brazing. The structure was then cold-tested with the HP8720 network analyzer. The coupling curve was measured. I found that the measured transmission was very low. The reflection (S_{11}) curve is shown in figure 6-6. The S_{11} curve in the figure has only three dips. This means that the losses in the structure are so high that the field was not able to penetrate beyond the third cell of the structure. The bead pull measurements proved that there was no field in the cells beyond the third cell. The field in the third cell had low amplitude. It was concluded that the attempt to construct a bolted PBG accelerator was unsuccessful.

The new idea of a PBG accelerator fabrication was electroforming. Electroforming is a process when the rods and the plates are grown together as a single copper structure. Then good electrical connections between rods and plates in the structure would be automatically ensured. The electroforming was performed by Custom Microwave, Inc [33]. The aluminum mandrels with holes in place of the rods were fabricated first.
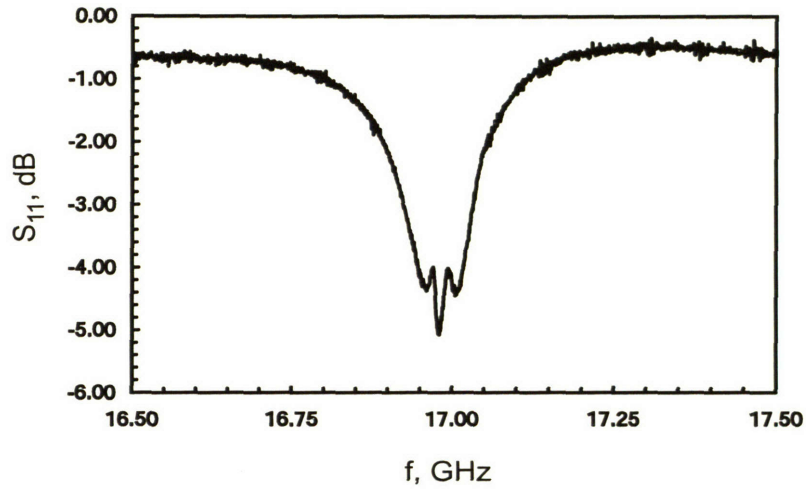
Figure 6-6: The S_{11} coupling curve for the bolted 6-cell PBG accelerator.
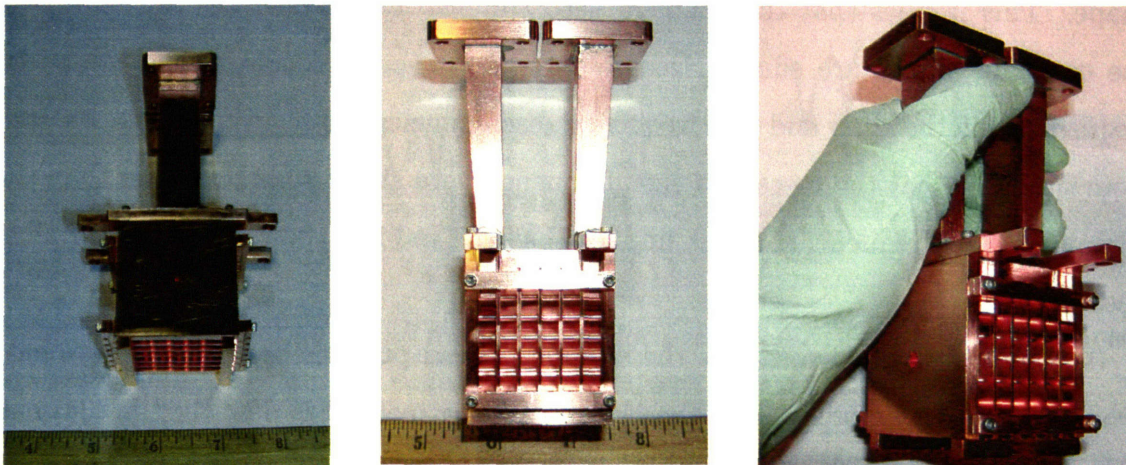
Figure 6-7: Electroformed PBG accelerator structure.

Then the mandrels were placed into copper solution. Copper ions were deposited on the mandrels and PBG cells consisting of the rods and two half-plates were formed. Aluminum was then etched away. The cells were put together and soldered. Copper was flashed over the whole structure to cover the solder joints. The waveguides were bolted to the structure. Side pieces were bolted for additional mechanical strength. The electroformed structure is shown in figure 6-7.

6.4 First cold test results and conclusions

First, the coupling curves for the new structure were measured with the HP8720 network analyzer. The coupling curves are shown in figure 6-8. Coupling into both waveguides was measured. Two coupling curves S_{11} and S_{22} are slightly different due to losses in the structure. The coupling curves are shown in both, linear and logarithmical, formats. The measured curves closely resemble the computed curves of figure 6-3. The comparison of the measured and theoretical reflection curves is shown in figure 6-9. Six dips are present in the reflection coefficient measurement. This means that six standing waves are present in the structure and all six cells resonate. The shape of the coupling curves is slightly different from the computed shape. This implies that the couplers need tuning. The frequencies of the dips in the coupling curves are summarized in table 6.2. For comparison, the computed frequencies of the dips and the frequency discrepancies are shown. It can be seen from the table that the measured eigenfrequencies are about 20 MHz higher than the computed eigenfrequencies. This implies that the radii of the rods are larger than needed.

The next test performed was the so-called "bead pull" measurement of the field profile in the eigenmodes. The "bead pull" testing method is described in [34] and is based on Slater perturbation theorem [35]. According to Slater's theorem, the resonant frequency of a cavity shifts when a small dielectric volume is placed inside the cavity. The frequency shift is proportional to the square electric field magnitude
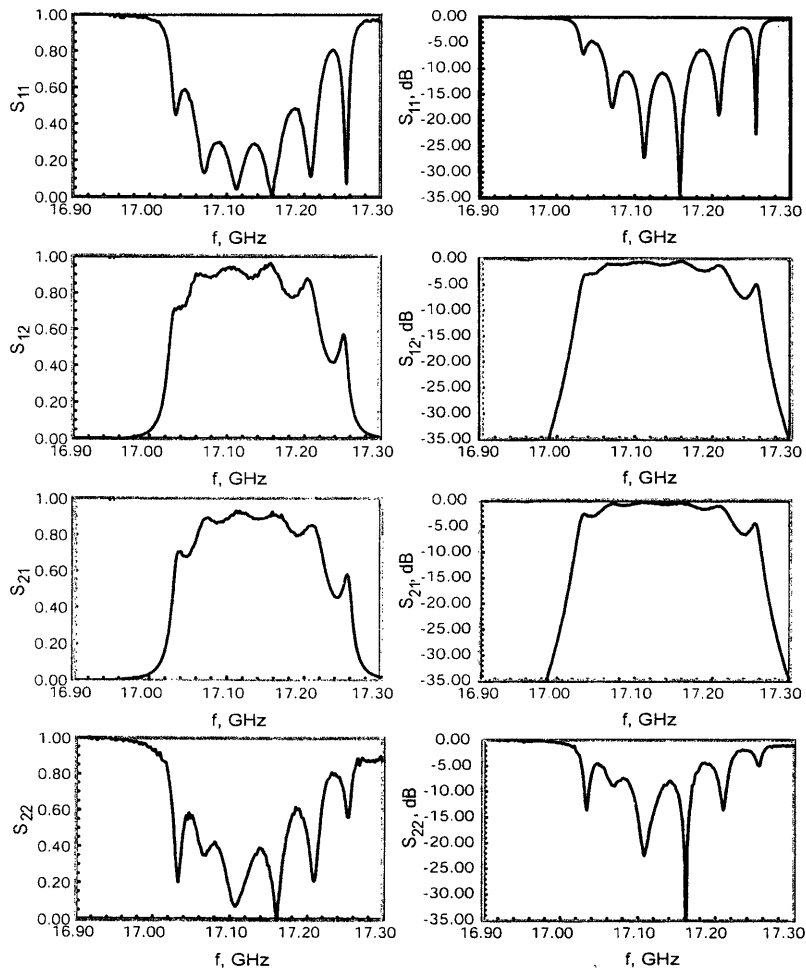
Figure 6-8: The coupling curves for the electroformed 6-cell PBG accelerator in linear and logarythm formats.
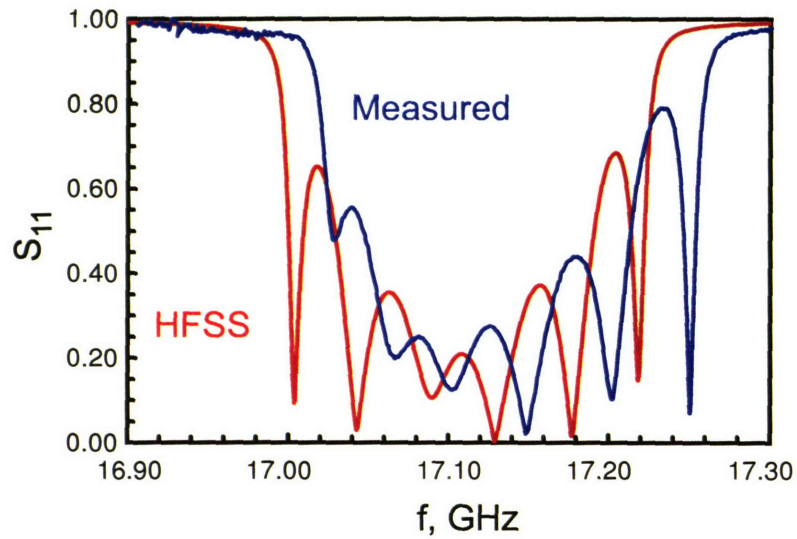
Figure 6-9: The comparison between the theoretical S_{11} curve for the 6-cell PBG accelerator and the measured S_{11} curve for the electroformed structure in linear format.
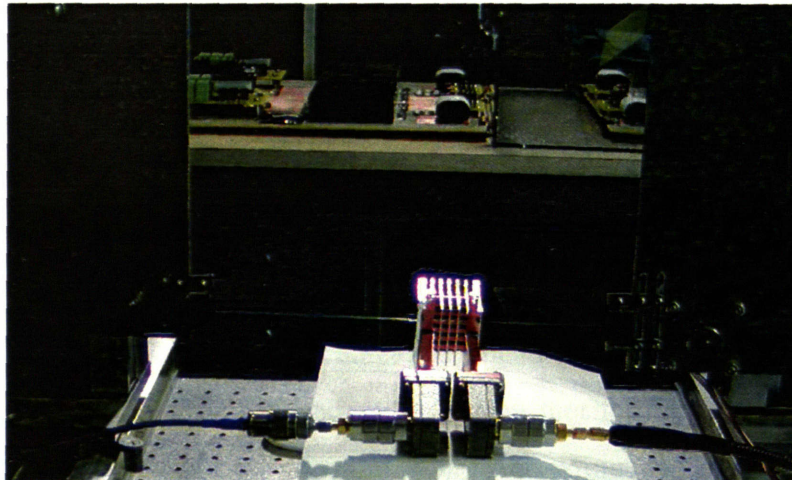
Figure 6-10: Beadpull test stand.
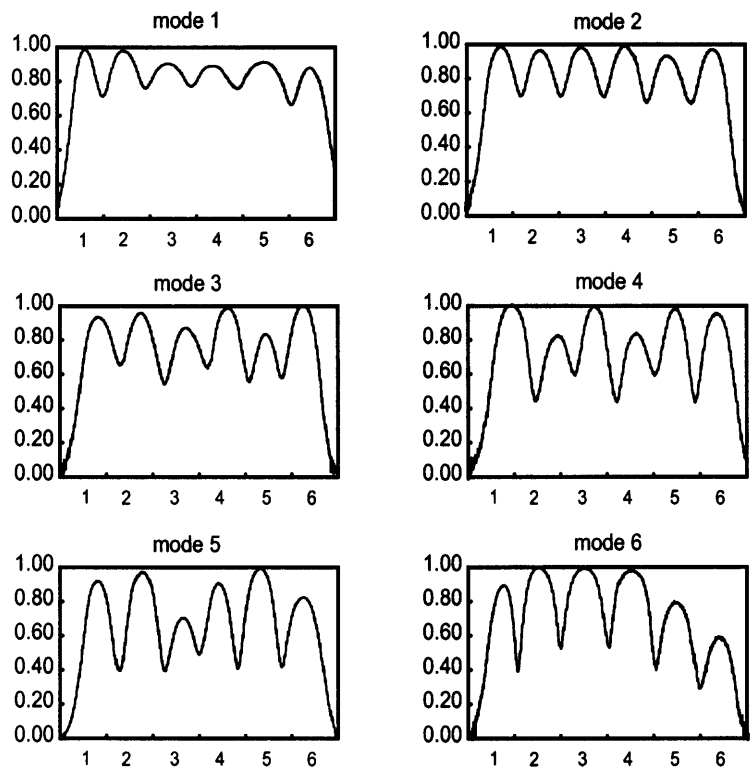
Figure 6-11: Field profiles of the eigenmodes of the electroformed PBG accelerator.

at the perturbation point E^2:

$$\frac{\Delta\omega}{\omega} = \frac{3V_{pert}}{4W}\frac{\varepsilon - 1}{\varepsilon + 2}E^2, \tag{6.1}$$

where V_{pert} is the volume of the perturbing object, ε is its dielectric permittivity, W is the energy stored in the resonator. If the resonator is powered from a port, the phase of the reflected signal behaves linearly with frequency in the vicinity of the resonance. When the resonant frequency shifts, the phase of the reflected signal (or of the signal transmitted through another port) at the resonance frequency changes linearly, proportionally to the frequency shift. This allows us to calculate the electric field at different points of the structure based on the measurement of the resonant frequency shifts or transmission phase shifts.

The measurement was performed as follows. A $1/32''$ diameter nylon $(\varepsilon \sim 3)$ bead was mounted on a thin 2-pound fishing line. The line with the bead was pulled though the structure with a motor (figure 6-10). An HP8720 network analyzer was switched into the time-domain mode with a 10 s sweep time. The phase shift of the signal transmitted through the structure was recorded as the bead travelled through the structure on axis. The network analyzer trace was then saved with a Labview program, written by this author. The data was analyzed and the field profile was derived for each resonant mode. The field profiles are plotted in figure 6-11. The field profiles look similar to those computed theoretically (figure 6-4), but still are slightly different. This again implies that the structure coupler must be tuned. There might also be discrepancies between different TW cells frequencies.

Table 6.2: The eigenmodes of an electroformed 6-cell PBG accelerator vs. theoretically computed eigenmodes.

	mode 1	mode 2	mode 3	mode 4	mode 5	mode 6
Frequency (measured), GHz	17.026	17.062	17.106	17.146	17.201	17.248
Frequency (theory), GHz	17.004	17.043	17.090	17.130	17.177	17.218
Frequency mismatch, MHz	22	19	26	16	24	30
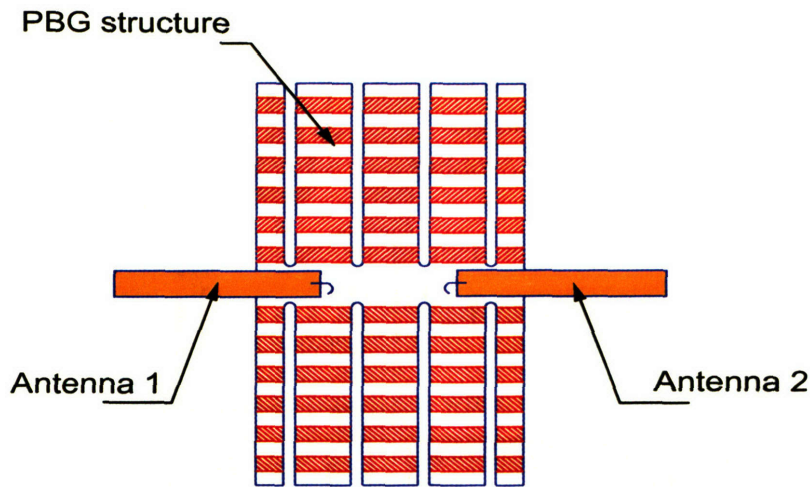
Figure 6-12: Cell frequency measurement with two coaxial antenna.

The following technique was applied to measure the TW cells frequency discrepancies. Two 0.140″ semi-rigid coax cables were placed at the middle of PBG cells as shown in figure 6-12. The cell in between two antennas was excited and the frequency of maximum transmission was measured. An amplifier was used to obtain a stronger signal. The eigenfrequencies of the cells #2 though #5 were measured this way. The results are summarized in table 6.3. The frequencies of cells #2, #3 and #4 were found to be very close, while the cell #5 was 10 MHz lower in frequency than its neighbor cells. Unfortunately, the two-antenna method does not allow us to measure the frequencies of the coupler cell. Also, one cannot say how the frequency measured with the antenna is related to the frequency of the $2\pi/3$ mode of the structure. The method allowing to determine the coupler cell frequency and the frequency mismatch for the TW cells is described in the next section.

Table 6.3: The eigenfrequencies of TW cells of electro-formed structure measured with two coaxial cables.

Cell number	2	3	4	5
Frequency, GHz	17.138	17.138	17.136	17.127
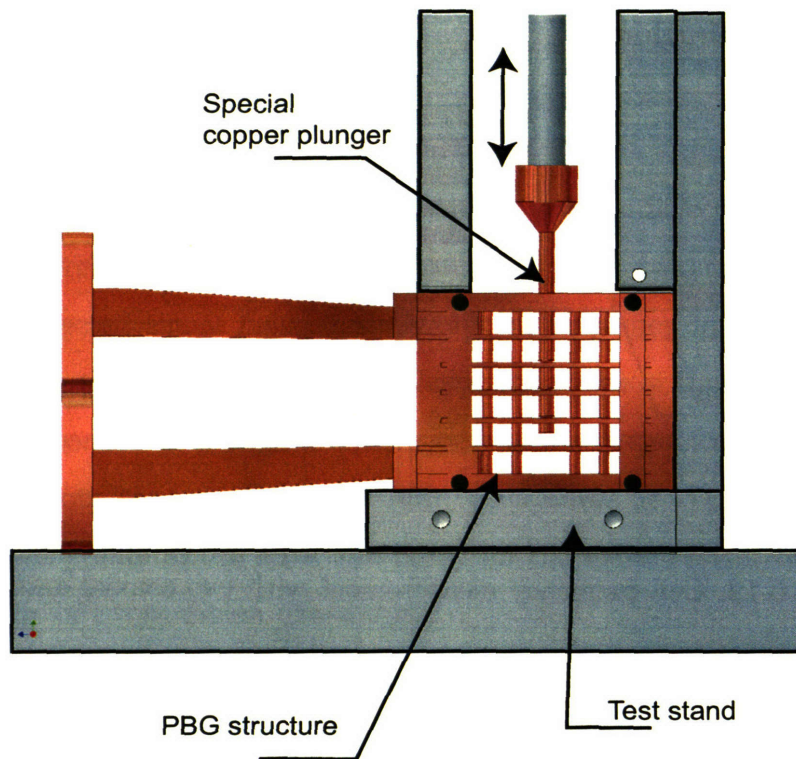
Figure 6-13: The special test stand with a copper plunger for the coupler cell testing with Kyhl's method.

6.5   PBG coupler testing with Kyhl's method

Kyhl's method of impedance matching when a rectangular waveguide is connected to the TW periodic structure is best described in [36]. The method allows to determine by how much the dimensions of the coupling cell and the coupling opening are different from the ideal matching dimensions. First, I will describe the measurement procedure and next, I will explain the theoretical basics for the method. To start the measurements, a special copper plunger must be manufactured and installed to move straight along the structure axis (see figure 6-13).

At the beginning, the plunger must be moved down so that the coupling cell is detuned. The phase of the reflection in this case is almost independent of the frequency. The value of the phase must be recorded. Then the plunger is retracted to the following cavity. The phase of the reflection must now be determined for the

following frequencies:

- The computed frequency of the $2\pi/3$ mode $f_{2\pi/3}$.

- The computed frequency of the $\pi/2$ mode $f_{\pi/2}$.

- The arithmetic mean of the above frequencies f_{ave}.

If the size of the coupler cell is correct, then the phase of the reflection at f_{ave} will be different from the phase of the reflection when the plunger is in the coupling cell by 180^0. If this is not true, then the diameter of the coupling cell must be adjusted to bring the phase of the reflection to the correct value. Next, if the coupling opening dimension is correct, then four reflection points will fall on the Smith chart as shown in figure 6-14 (a). If the reflection points fall as shown in figure 6-14 (b), then the structure is undercoupled. The coupling hole must be increased to achieve critical coupling. If the reflection points fall as shown in figure 6-14 (c), then the structure is overcoupled. The coupling hole must be decreased to achieve critical coupling.

The theoretical basics for this method is the following. The electrical properties of the accelerator structure operating in the lowest passband are fully described by its equivalent circuit. The equivalent circuit for a low bandwidth accelerator structure is derived in Appendix B and shown in figure B-6. Assume, we have some input coupling network, which provides critical coupling into $2\pi/3$ mode of the structure. This means that the admittance of the coupling network is equal to the infinite structure admittance at $2\pi/3$ mode (see Eq. (B.28)):

$$jY_{in} = jY_\infty \left(\frac{2\pi}{3} \right) = \frac{Y_c}{2\sqrt{3}}.$$ (6.2)

Placing a detuning plunger in a coupling cavity has an effect of disconnecting the whole network from its first capacitive section (figure 6-15). The reflection from this section is equal to

$$R_1 = \frac{jY_{in} - jY_c/2}{jY_{in} + jY_c/2} = \frac{1 - j\sqrt{3}}{1 + j\sqrt{3}} = \exp\left(-j\frac{2\pi}{3} \right).$$ (6.3)

103
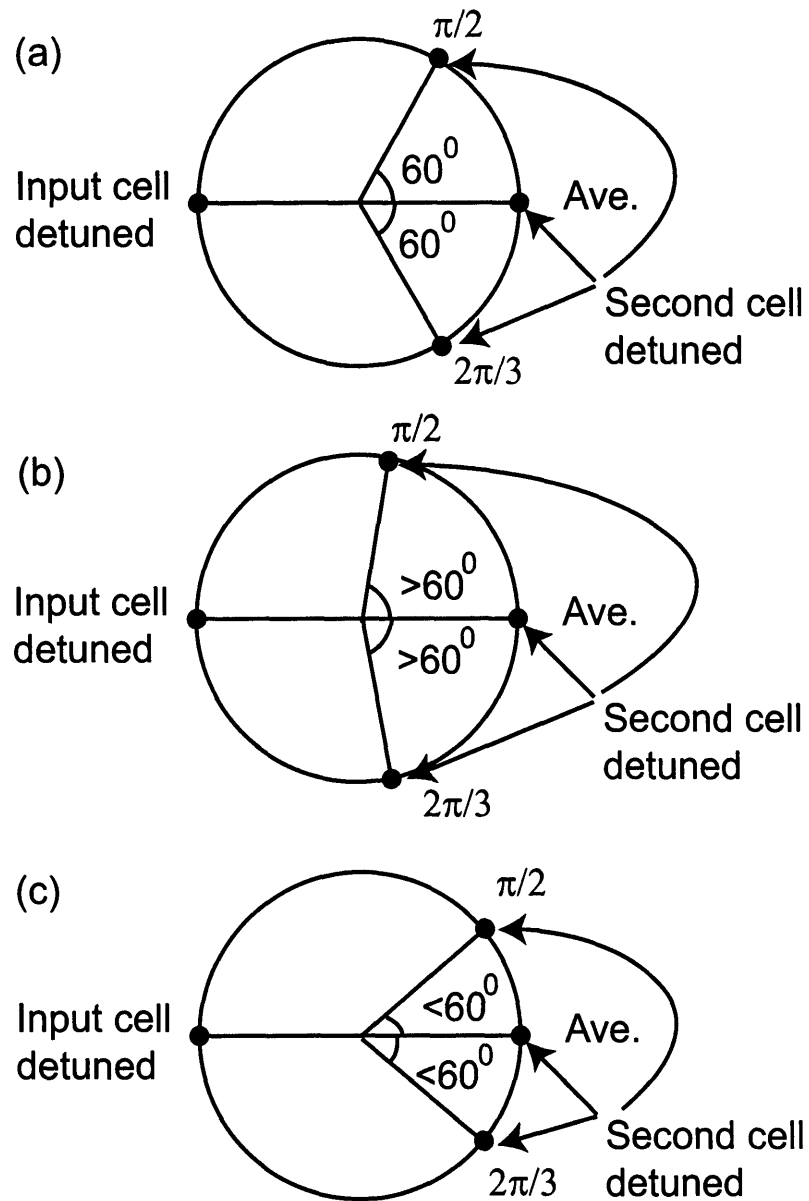
Figure 6-14: Smith chart plot for reflections from the copper plunger: (a) critically coupled structure, (b) undercoupled structure, (c) overcoupled structure.
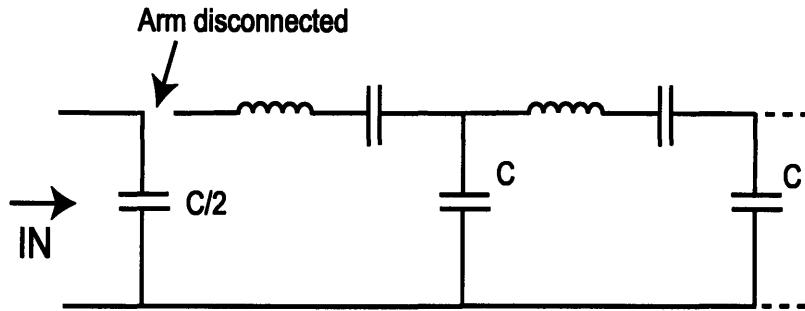
Figure 6-15: Equivalent circuit for the accelerator structure with coupler cell detuned with plunger.
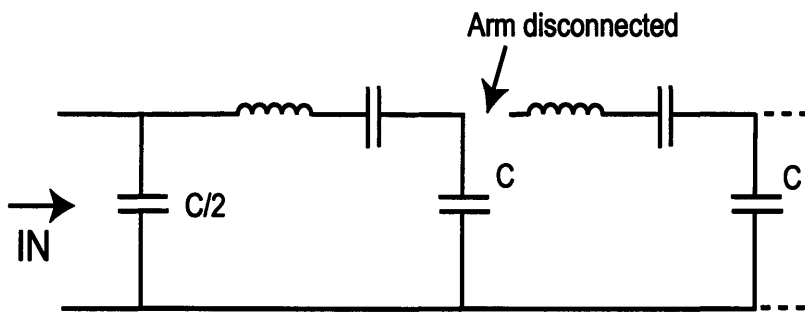
Figure 6-16: Equivalent circuit for the accelerator structure with second cell detuned with plunger.
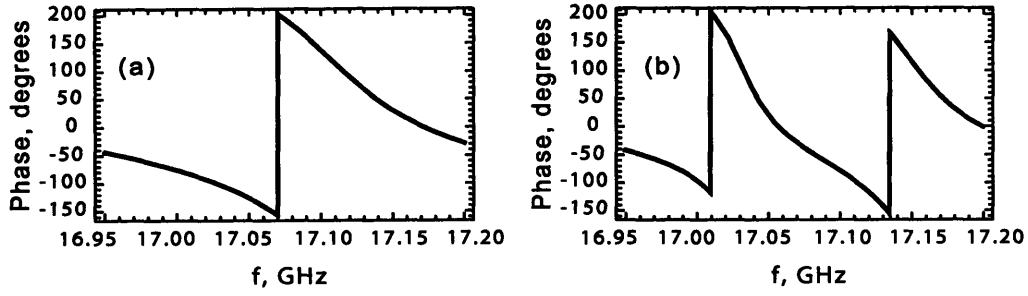
Figure 6-17: Phase of the reflection from detuning plunger vs. frequency: (a) plunger in a second cell, (b) plunger in a third cell.

Placing a detuning plunger in a second cavity disconnects the network from the coupling scheme section (figure 6-16). Using the definitions of Appendix B, we compute that the reflection from the plunger now will be

$$R_2 = \frac{jY_{in} - jY_c\left(\frac{1}{2} + \frac{1}{1-Y_cX_{ser}}\right)}{jY_{in} + jY_c\left(\frac{1}{2} + \frac{1}{1-Y_cX_{ser}}\right)} = \frac{1 - j\sqrt{3}\left(1 + \frac{2}{1-Y_cX_{ser}}\right)}{1 + j\sqrt{3}\left(1 + \frac{2}{1-Y_cX_{ser}}\right)}. \qquad (6.4)$$

Knowing that X_{ser} is linear with frequency, we can plot the dependence of the phase of R_2 on the frequency (figure 6-17(a)). In particular, for the frequencies of the $\pi/2$ -mode, $2\pi/3$-mode and the average frequency we have

$$R_2\left(\frac{\pi}{2}\right) = \exp\left(j\frac{2\pi}{3}\right),$$

$$R_2\left(\frac{2\pi}{3}\right) = 1,$$

$$R_2\,(\text{ave}) = \exp\left(j\frac{\pi}{3}\right).$$

Thus the reflection from a plunger detuning the first cell of a periodic structure with a correctly tuned coupler will follow the Smith chart of figure 6-14 (a).

When the coupler is tuned right, Kyhl's method allows us to check the correct frequency of the first TW cell (second cavity). To do this, the plunger must be retracted to the third cavity and the dependence of the phase of the reflection R_3 on frequency must be measured. The dependence of the phase of R_3 on frequency for the

106

correctly tuned TW cell is shown in figure 6-17(b). The phase of R_3 at $2\pi/3$ mode is different from the phase of R_2 at $2\pi/3$ mode by 240^0. If the difference between two phases is not 240^0 then the second cavity does not have the right frequency and must be tuned.

Two couplers of the electroformed PBG structure were tested with Kyhl's method. f_{ave} was measured and compared to the computed value of 17.108 GHz. One coupler (cell #6) was found to be correct. The second coupler was found to be about 20 MHz higher in frequency than it should be.

6.6   PBG structure etching

To correct the frequency of the cells it was proposed to etch the rods, which would make the rods smaller, effective PBG resonator diameter bigger and the frequency of the cells lower. Based on the measurement results and HFSS computations, the machine shop order for etching was made. It is summarized in table 6.4.

Table 6.4: Etching order for tuning of a 6-cell PBG accelerator.

Cell number	Etch in diameter
1	0.0004″
2	0.0004″
3	0.0004″
4	0.0004″
5	0.0002″
6	do not etch (mask)

The etching was performed at the Material Science and Technology group at Los Alamos National Laboratory (LANL). The structure was mounted on a stainless steel rod, about 12 inches in length. The rod was wrapped with heat shrink tubing and tape to a diameter that provided a press fit into the beam hole of the structure and

107
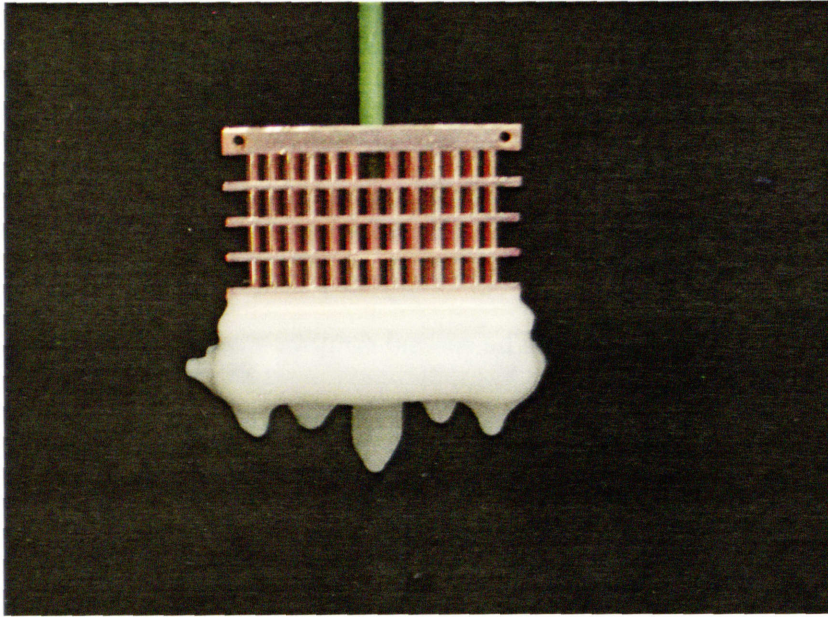
Figure 6-18: PBG structure with cells #5 and #6 masked with wax.

then was inserted into the beam hole. This served both to mask the beam hole and as a handle for the dipping operation. Jack-o-lantern candles were melted in a beaker on a hot plate and served as a masking material. This wax was found to be suitably resistant to chemical attack by the açid solution. Acid solution was mixed as follows: 100 ml nitric acid, 275 ml phosphoric acid, 125 ml acetic acid. This solution is usually used at 65C to polish copper and removes about 0.0005″ per minute from each side. The candle wax, however melted at 50C, so the acid bath was used at 45C instead. At 45C, the acid mixture removes 0.0001″ per minute from each side of copper rods.

First, the structure was dipped into the molten wax just enough to cover cell #6. The dip was repeated several times and cooled to room temperature between dips so that a thick layer of wax could form. The entire structure was then dipped into the 45C acid mixture for one minute for removal of 0.0001″ per surface or 0.0002″ from the diameter of the rods. Next, the structure was rinsed in deionized water and blow-dried with nitrogen. After that the structure was dipped again in wax - this time enough to cover cells #5 and #6, repeated and cooled for a thick coat. Figure 6-18 shows the structure with cells #5 and #6 masked. The entire structure was

108

dipped in 45C acid mixture for one more minute, rinsed with deionized water and blow-dried with nitrogen.

The wax was removed with a detergent cleaner in an ultrasonic tank at 70C. The structure was rinsed with deionized water and dipped in chromic acid solution for final cleaning of tarnish spots from previous steps. Finally, it was rinsed in deionized water and blow dried again. The etching was successfully completed.

6.7 Cold test results for the etched structure

The same tests as described above were performed again to test the etched PBG accelerator. New transmission and reflection curves are shown in figure 6-19. The comparison of the S_{11} transmission curve to the S_{11} curve computed with HFSS is shown in figure 6-20. Very good agreement is observed between two curves. The only difference is the increased dispersion of the measured curve. The reason for the increased dispersion is the etching process. While the etching decreased the diameter of the rods it also decreased the plate thickness and thus increased the dispersion. In the Conclusion chapter, I will discuss what modification could be made to the tuning method to be able to compensate the change of the dispersion. Slight increase in the dispersion of the structure due to etching should not affect significantly the acceleration properties of the structure. The future accelerating mode, Mode 4, was found to be at 17.135 GHz in air, which means that it will be at around 17.140 GHz in vacuum.

Field profiles for the structure eigenmodes were again measured with the beadpull. Figure 6-21 shows the field profiles. Mode 4, which is the most important for us, now has the flat field profile. This result is correct and agrees with the computation.

Eigenfrequencies of the four TW cells were measured with two coax cables. The results are summarized in table 6.5. It can be seen from the table that now the TW cells are almost identical.
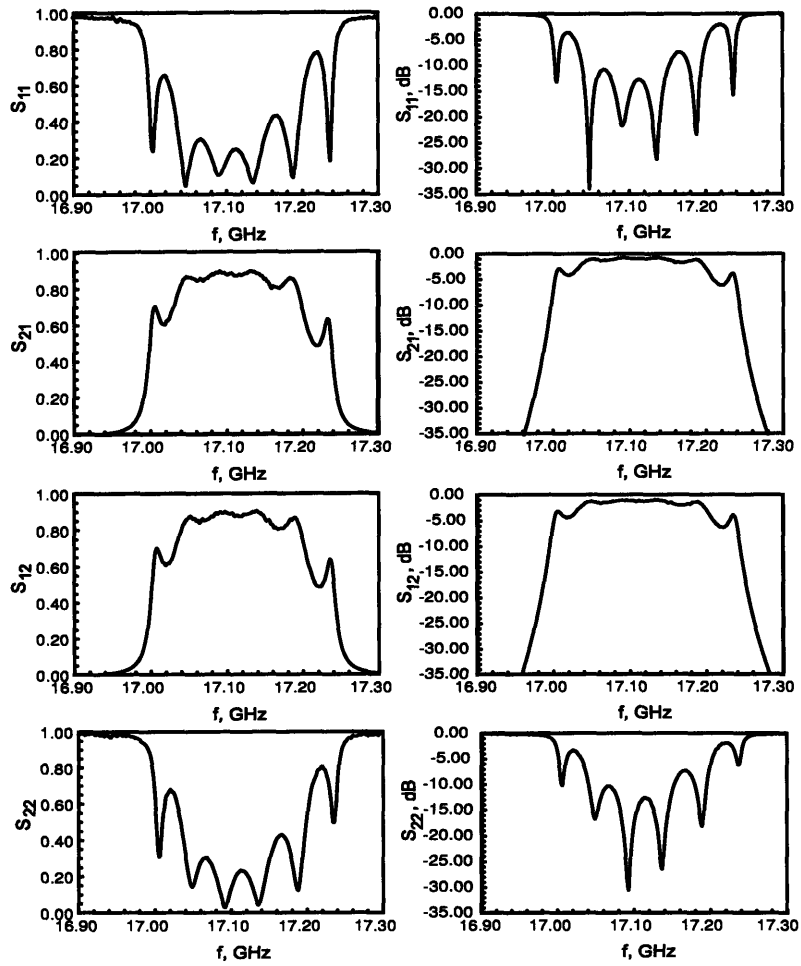
Figure 6-19: The coupling curves for the etched 6-cell PBG accelerator in linear and logarithm formats.
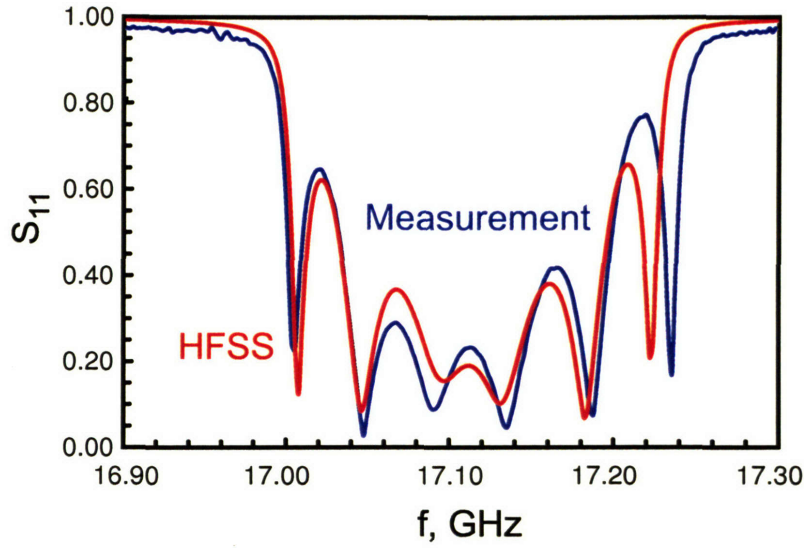
Figure 6-20: The comparison between the theoretical S_{11} curve for the 6-cell PBG accelerator and the measured S_{11} curve for the etched structure in linear format.
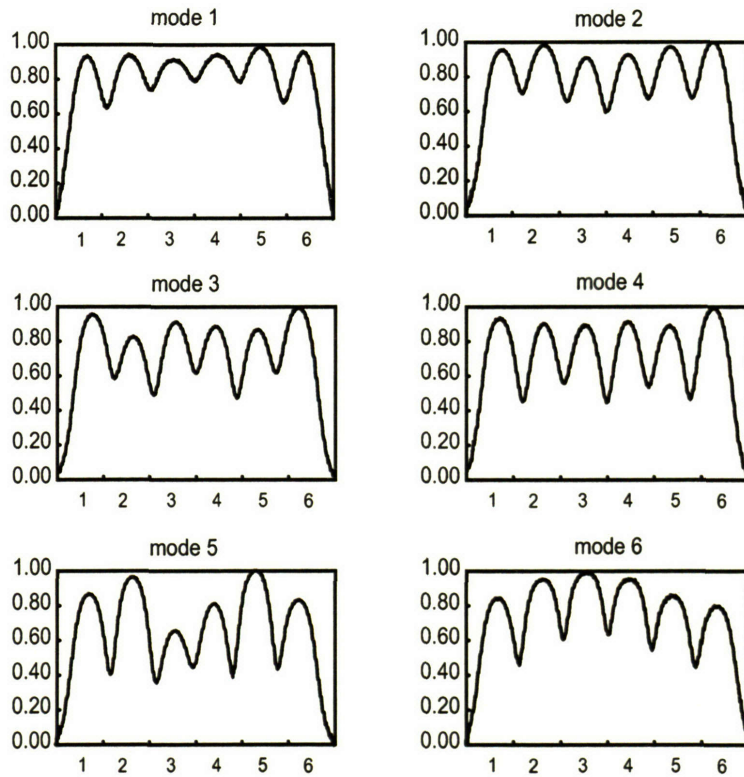
Figure 6-21: Field profiles of the eigenmodes of the etched PBG accelerator.

Table 6.5: The eigenfrequencies of TW cells of etched structure measured with two coaxial cables.

Cell number	2	3	4	5
Frequency, GHz	17.120	17.118	17.117	17.119

Two couplers of the etched PBG structure were again tested with Kyhl method. f_{ave} was measured for both couplers. First coupler (cell #1) had $f_{ave} = 17.109$ GHz. The second coupler (cell #6) had $f_{ave} = 17.108$ GHz. The phase of the reflection from the plunger at different frequencies was also measured. For cell #1 I obtained:

$$\phi_{\pi/2} - \phi_{ave} = 68^0,$$
$$\phi_{ave} - \phi_{2\pi/3} = 64^0. \qquad (6.5)$$

For cell #6:

$$\phi_{\pi/2} - \phi_{ave} = 67^0,$$
$$\phi_{ave} - \phi_{2\pi/3} = 67^0. \qquad (6.6)$$

Taking into account that the phase length of the coupling waveguide is about 9^0 bigger for the $\pi/2$ - mode frequency than for the average frequency and also 9^0 bigger for the the average frequency than for the $2\pi/3$ - mode frequency, the critical coupling phase difference must be 69^0. This implies that the structure is $2^0 - 3^0$ overcoupled. This is just a slight overcoupling. Therefore, it can be concluded that the PBG accelerator was tuned successfully.

6.8 Temperature dependence of the structure eigenfrequencies

Powering the accelerator structure with several MW of rf may lead to the structure heating due to Ohmic losses. Therefore it is important to know how the accelerating mode frequency will behave with temperature. A special oven was used to measure the temperature dependence (see figure 6-22). The structure was placed inside the
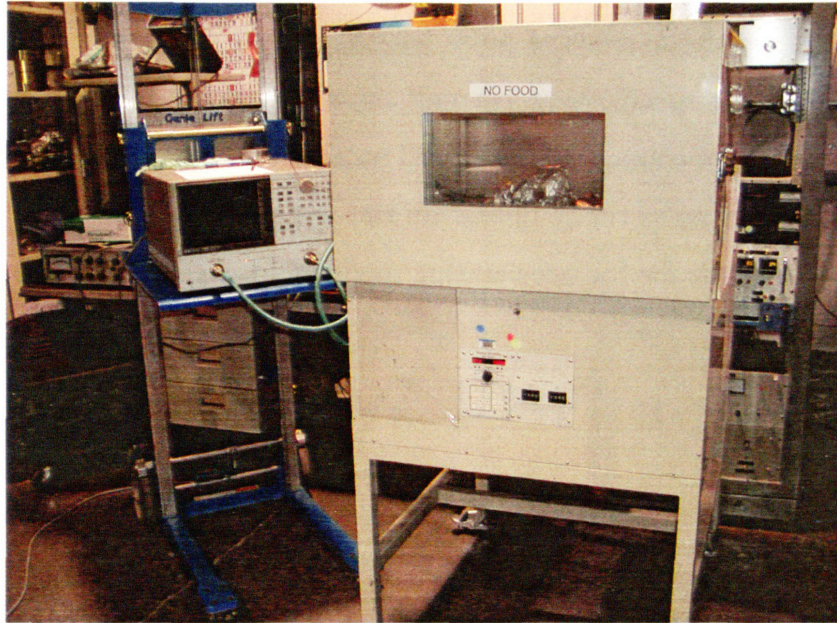
Figure 6-22: PBG structure inside the heating oven.

oven and heated slowly at about 5^0C/hour. This ensured the uniform temperature throughout the structure. The frequencies of Mode 4 and Mode 6 were recorded with the network analyzer. The data is summarized in table 6.6. The data shows that the eigenmode frequencies decrease with temperature at the rate of about 1 MHz per 5^0 C.

Table 6.6: Temperature dependence of the structure eigenmode frequencies.

t, ^{0}C	26	31	36	41	46
Frequency (Mode 4), GHz	17.135	17.134	17.133	17.132	17.131
Frequency (Mode 6), GHz	17.233	17.231	17.230	17.229	17.228

To estimate the temperature rise due to microwave heating of the PBG accelerator structure the following formula can be applied [37] :

$$\Delta T = R_s H_{wall}^2 \sqrt{\frac{t_{pulse}}{\pi \rho c_v k}},$$

113

where R_s is the structure shunt impedance, H_{wall} is the maximum magnetic field on the wall, t_{pulse} is the microwave pulse length, $\rho = 8900\frac{kg}{m^3}$ is the copper density, $c_v = 385.39\frac{J}{kg\,^0C}$ is the specific heat per unit mass of the copper, $k = 380\frac{W}{^0C\cdot m}$ is the thermal conductivity of copper. For the PBG accelerator with the average gradient of 30 MV/m and 100 ns pulse the temperature rise will not exceed 10 ^{0}C, which means that the frequency shift for the accelerating mode will not exceed 2 MHz.

Chapter 7

Hot test of a TW PBG accelerator

7.1 Introduction

The goal of the hot test experiment was to demonstrate the acceleration of a real electron beam by a 6-cell PBG accelerator structure. The PBG structure was installed on a 17 GHz MIT linac beamline [29] (see layout in figure 7-1 and the photograph in figure 7-2). A power splitter was installed at the Haimson Research Corporation (HRC) klystron [28] output arm. 10 MW of power was produced by the klystron and split into two parts. The bigger power was used to feed the linac, while the smaller part, about 3 MW were transported in a 12 feet long WR62 waveguide to the PBG accelerator. Approximately 2 MW reached the PBG chamber, which would be enough to produce the accelerating gradient of 35 MV/m and accelerate the linac electron beam by more than 1 MeV. The energy gain is measured by the HRC spectrometer. The schematic of the test components is shown in figure 7-3.

This chapter describes the hot test experiment. First, the major system components of the 17 GHz accelerator experiment will be introduced. The high power 17 GHz klystron, linac and linac beamline will be discussed. Next, the PBG vacuum chamber, high power feed and spectrometer will be described. Finally, experimental results will be explained.
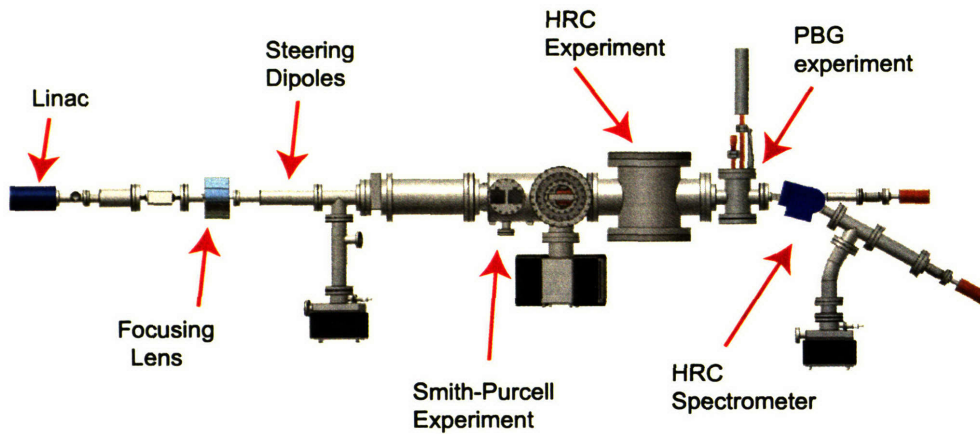
Figure 7-1: 17 GHz linac beamline layout with PBG chamber installed.

7.2 17 GHz accelerator experiment components

7.2.1 The klystron

The Haimson Research Corporation relativistic klystron amplifier supplies the power for the accelerator and the PBG structure. The klystron is designed to produce up to 25 MW (saturated gain up to 70 dB) of RF power at 17.132-17.142 GHz for pulse lengths up to 1 μs. It consists of the input RF cavity, followed by a gain section and then followed by a travelling wave output section. The klystron beam is supplied by a pierce electron gun which is built by Thomson Co. and is able to produce the current up to 100 A [38]. The drive for the klystron is provided by a travelling wave tube amplifier (TWTA) with 1-10W of output power. The TWTA is driven with the HP6871B synthesizer, which produces 1μW to 10 mW of power at 2-18 GHz. Due to the absence of a circulator at the output, the klystron was rarely operated at the maximum power. In the PBG experiment, the synthesizer was typically operated at about 1 mW, which results in about 10 MW of output klystron power.
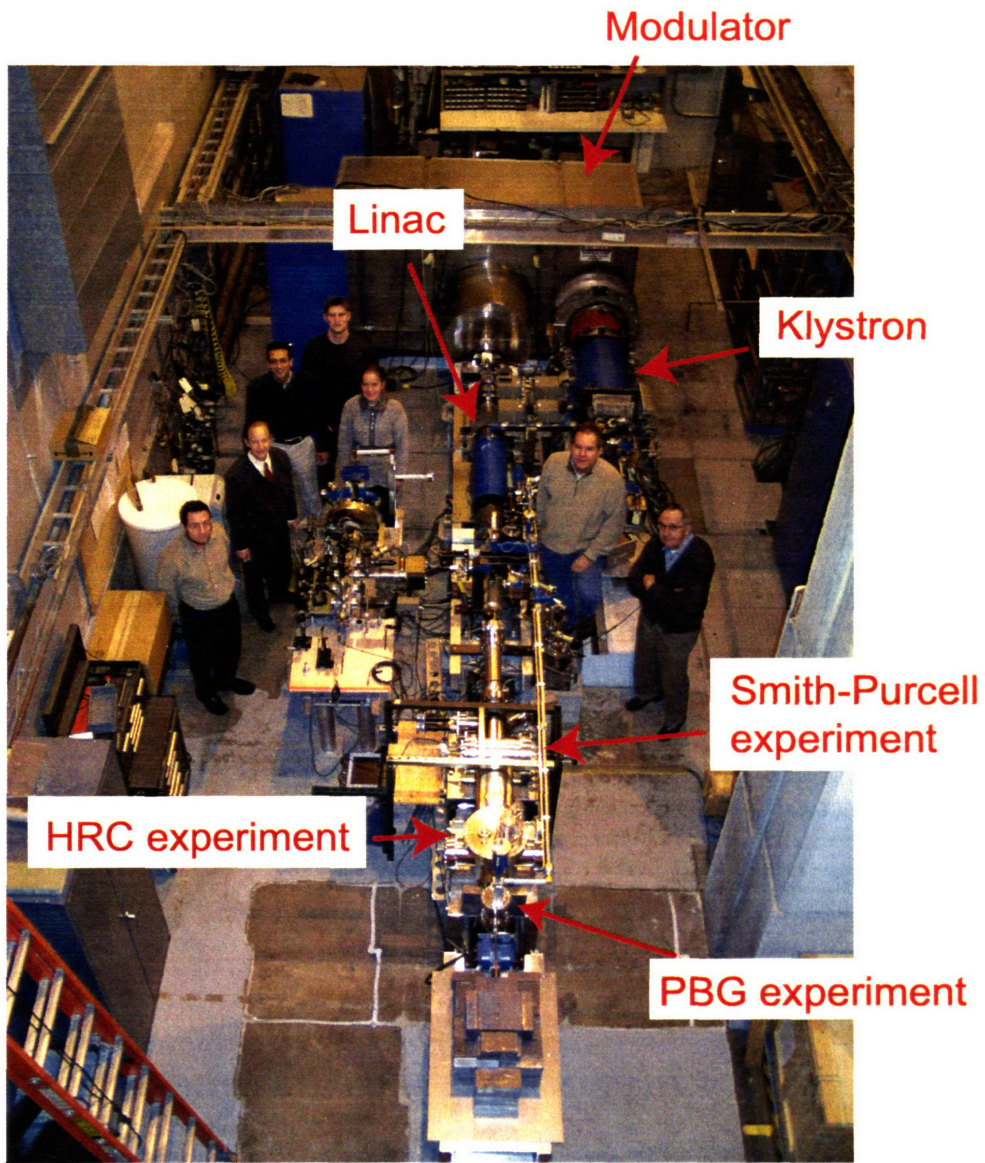
Figure 7-2: MIT 17 GHz acceleration laboratory photograph.
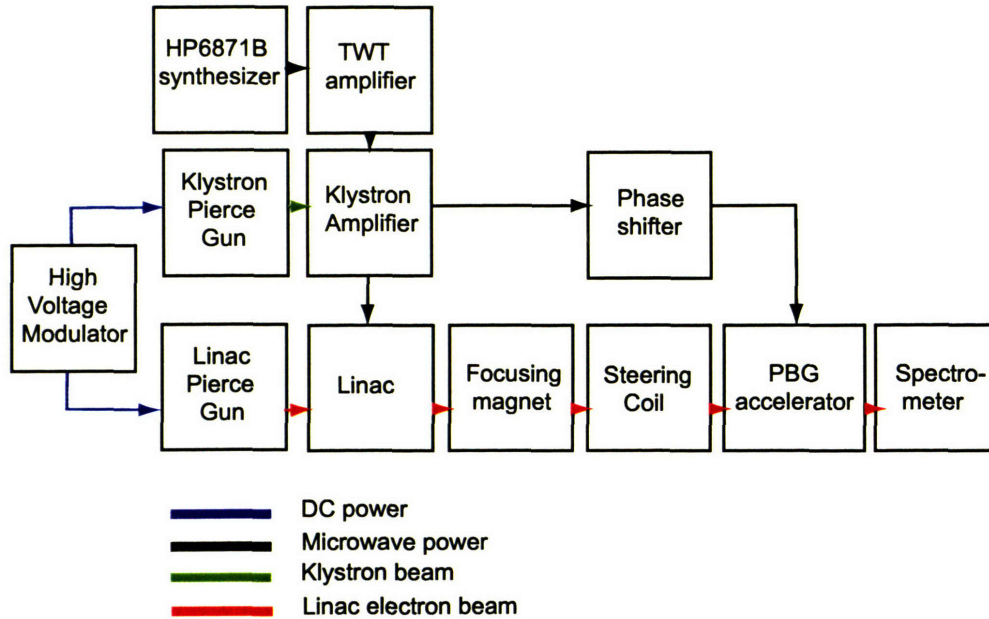
Figure 7-3: The schematic of the PBG accelerator hot test components.

The klystron output is connected into a four-port hybrid coupler designed by HRC. Dual WR-62 output waveguides are connected and the power is then directed into two separate arms. Power levels ratio between the arms can be varied. One arm is directed towards the linac and the second arm goes to the PBG experiment. The forward and reflected power on both arms is measured by using 65 dB directional couplers combined with additional attenuator chains terminated by Schottky diode detectors. The diode responses were calibrated at 17.140 GHz with the HP6871B synthesizer and with the HP4323B power meter.

7.2.2 The linac

The $2\pi/3$ mode 17.136 GHz linac is a quasi-constant gradient disk-loaded structure consisting of 94 cells with 15 different cell types. The linac provides accelerating gradients up to 45 MV/m, depending on the input RF power, and outputs a 10-20 MeV electron beam. The structure has a group velocity in the range of $0.0196 \div 0.0474c$ which results in 58 ns filling time [29]. The linac beam is generated in a DC (Pierce) electron gun at the energy of 0.55 MeV with a normalized RMS emittance

of 1.8 π mm-mrad and transported to the chopper-prebuncher section. The chopper cavity produces bunches with the charge of 0.01 nC which are 100^0 long (with 360^0 corresponding to one rf period at 17 GHz), the prebuncher cavity provides a 10:1 charge compression and reduces 50 keV energy spread in the bunch to less than 10 keV and compresses the bunch length to 15^0 (out of 360^0). The 15^0 bunch is imputed into the main accelerator, where it is further compressed by another factor of 15 to 1^0. This corresponds to 180 fs bunch length [39]. The bunches come out in long bunch trains, one bunch per rf period.

7.2.3 The linac beamline

The linac beamline layout is shown in figure 7-1. At 0.5 m beyond the linac on the beamline, a focusing solenoid is installed. The solenoid produces magnetic fields up to 0.6 Tesla, which provide the minimum beam spot size of about 1 mm. Vertical and horizontal steering coils are located after the lens. Focusing solenoid and steering coils provide means to control the beam for the input to the experiments. Two bunch-length measurement experiments are installed further down the beamline. The first experiment is the MIT Smith-Purcell radiation experiment [40, 41] and the second experiment is the HRC bunch length measurement experiment [42]. PBG chamber and the HRC spectrometer were installed on the beamline last (figure 7-2). The HRC spectrometer ends with a Faraday cup (FC) which provides means for measuring the beam current.

7.3 PBG experiment components

7.3.1 PBG chamber

The PBG structure was installed on inside a vacuum chamber (see figure 7-4). The structure coupling waveguides were attached to the upper flange of the vacuum chamber with screws (figure 7-5). Two WR62 waveguides were welded into the upper flange for the microwave coupling. The microwave power from the klystron would be cou-
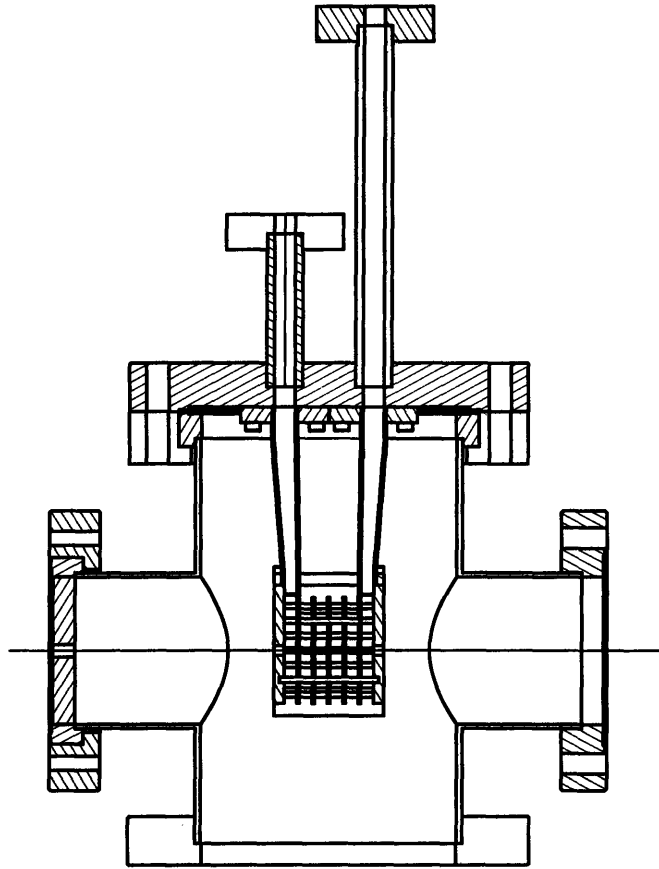
Figure 7-4: The PBG structure installed inside the vacuum chamber (Autocad drawing).

pled into the PBG accelerator though one of the waveguides. The load was installed on the second waveguide to absorb the power which passed though the structure. A stainless steal collimator was installed at the entrance to the PBG chamber. The collimator had a small (3.5 mm diameter) hole which would only allow the on-axis electron beam though. The collimator would prevent the electron beam from hitting and destroying the copper plates of the PBG accelerator. The PBG chamber was installed at the end of the linac beamline (figure 7-6). The collimator hole, the PBG structure beam hole and the Faraday cup at the end of the chamber were pre-aligned with a flash light.
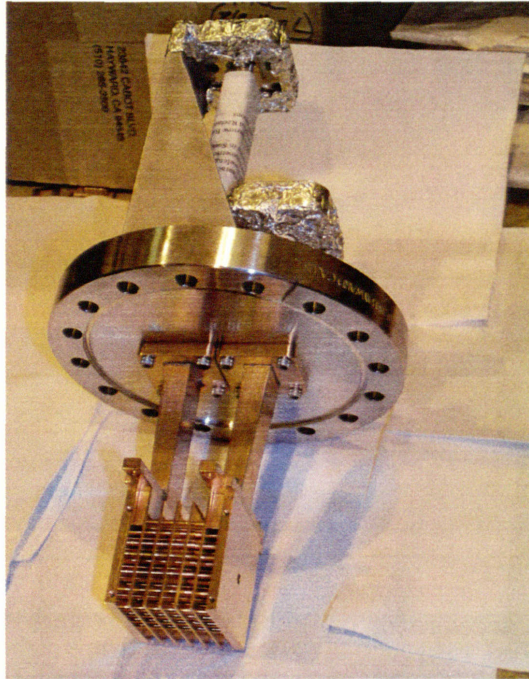
Figure 7-5: The PBG structure attached to the flange of the vacuum chamber.
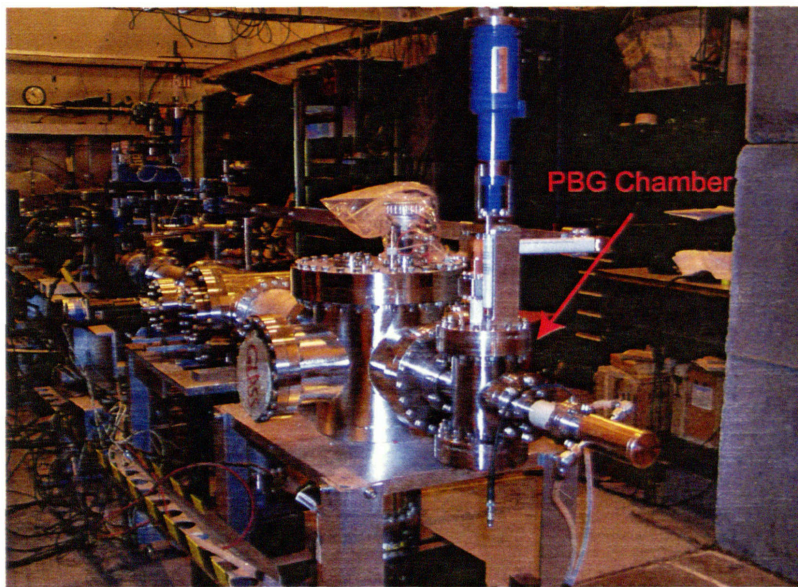
Figure 7-6: The PBG chamber installed on the linac beamline.
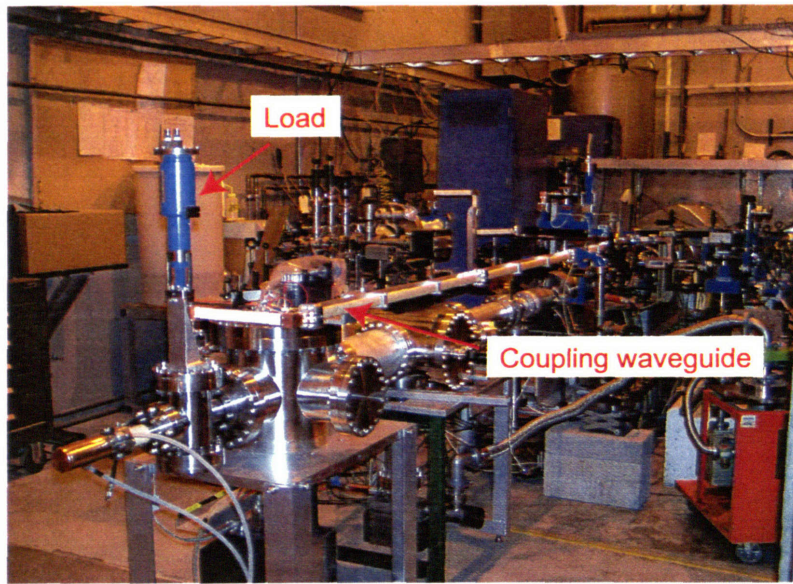
Figure 7-7: PBG accelerator coupling waveguide and high power load.

7.3.2   PBG structure power feed

Microwave power from the klystron was transported to the PBG structure by the means of a 12-feet-long WR62 waveguide (figure 7-7). The coupled and reflected power is measured at the klystron end of the waveguide with two 65 dB directional couplers combined with Schottky diode detectors. Some power becomes lost when transported to the PBG accelerator. Typical losses in OFE copper WR62 waveguide at 17 GHz are 0.5 dB (about 11%) per 10 feet, but higher losses occur at the waveguide bends. Measurement of the reflected power during breakdowns while we were doing the initial processing indicated that about 25% of power was actually lost in the waveguide.

A dielectric window installed in the waveguide separated the PBG accelerator section from the klystron section. Thus, installation and maintenance of the PBG accelerator chamber was possible without breaking the klystron vacuum. Finally, a phase shifter was installed on the waveguide allowing for different phase shifts between microwaves in the linac and the PBG accelerator. Optimal acceleration of the beam in the PBG structure is observed when the beam and the power enter the PBG structure

in correct phase. Power transmitted through the PBG structure was dumped into a load (figure 7-7).

Microwave power is coupled into the linac and the PBG structure at 100 ns pulses with a repetition rate of 1 Hz. The timing of the events in the system is shown in table 7.1. It takes longer for the microwave power to reach the PBG structure than for the speed-of-light electron beam. However, the filling time of linac is much longer than the filling time of the PBG structure, which is 10 ns. Thus, by the time the linac is filled and the electron beam starts coming through, the PBG structure also fills to accelerate the beam.

Table 7.1: Timing in the PBG accelerator experiment.

Time	Event
t=0	Linac and PBG accelerator powered
t=30 ns	Microwave power reaches PBG accelerator
t=40 ns	PBG accelerator fills
t=50 ns	Electron beam exits the linac
t=58 ns	Linac fills
t=60 ns	Electron beam enters the PBG accelerator
t=100 ns	Microwave pulse ends in linac
t=110 ns	Electron beam ceases in PBG accelerator
t=130 ns	Microwave pulse ends in PBG accelerator

7.3.3 The spectrometer

The HRC magnetic spectrometer (figure 7-8) was employed for the beam energy measurements. The physical principles of the spectrometer are the following. The main component of the spectrometer is the solenoid magnet. The electron beam entering the spectrometer is bent by the magnetic field of the solenoid. The magnetic field is confined within the solenoid volume, where the field is almost uniform. The magnitude of the magnetic field is proportional to the solenoidal current. The bending

radius for the electron beam is given by the following formula

$$r_{bend} = \frac{p_\perp c}{eB} \approx_{mc^2 \ll p_\perp c} \frac{E_{beam}}{eB} \propto \frac{E_{beam}}{I_{sol}},$$

(7.1)

where E_{beam} is the beam energy, I_{sol} is the solenoidal current. The stronger is the solenoidal current, the higher energy beam will be bent by exactly 30^0 over the width of the solenoid. After the solenoid the electron beam is detected by two Faraday cups: the first is straight on the beam line and the second one is at a 30^0 bend (see the photograph in figure 7-8 and the schematic in figure 7-9). When the solenoidal current is off, the current in the first Faraday cup is maximum. When the solenoidal current is turned on, the signal is the first Faraday cup is low. The value of the solenoidal current, when the signal at the second Faraday cup is maximum, is proportional to the beam energy. The spectrometer was calibrated and the dependence of the beam energy on the solenoidal current, for which signal is present at the second Faraday cup, was plotted (figure 7-10). For beam energies less than 25 MeV, this dependence is linear and can be approximated by the following formula

$$E[\text{MeV}] = 1.4 I[\text{A}].$$

(7.2)

7.4 PBG accelerator experiment results

Beam transport through PBG accelerator was optimized by adjusting the current in vertical and horizontal steering magnets and focusing solenoid. The Faraday cup signal at the end of the line was maximized. A typical FC signal corresponding to ~ 80 mA of current in plotted in figure 7-11.

The PBG accelerator structure was conditioned to couple 2 MW of microwave power at 17.140 GHz for 100 ns. The conditioning time was 1 week. According to the HFSS computations (see Table 5.2), the average accelerating gradient inside the PBG structure achieved for 2MW of input power must be around 35 MV/m. The typical forward and reflected signals for coupling into PBG structure are shown in
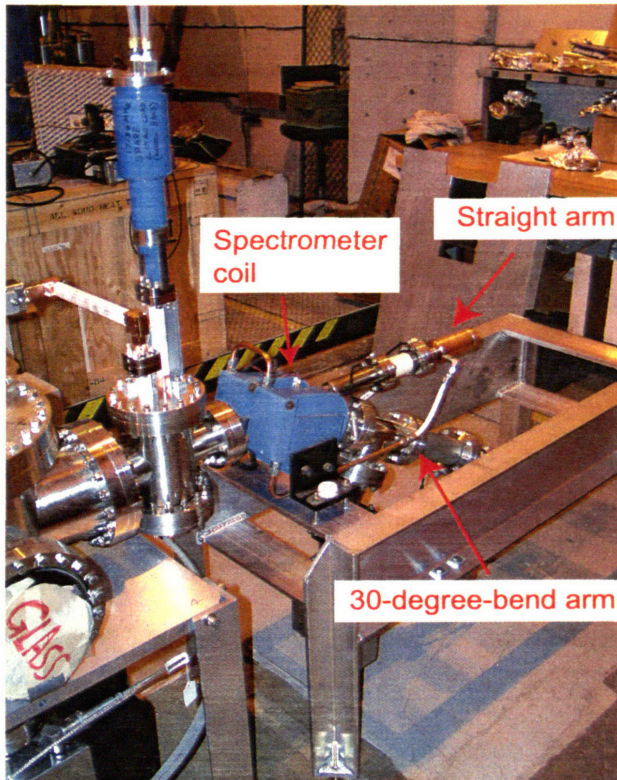
Figure 7-8: The photograph of spectrometer.
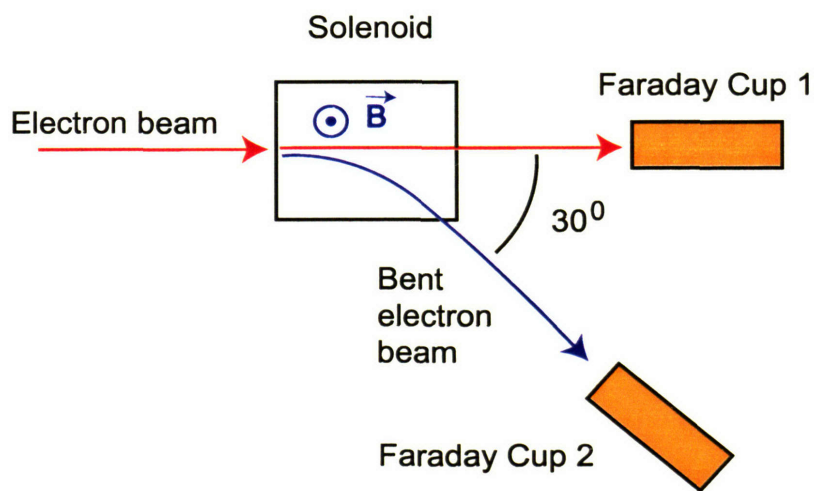
Figure 7-9: The schematic of spectrometer.
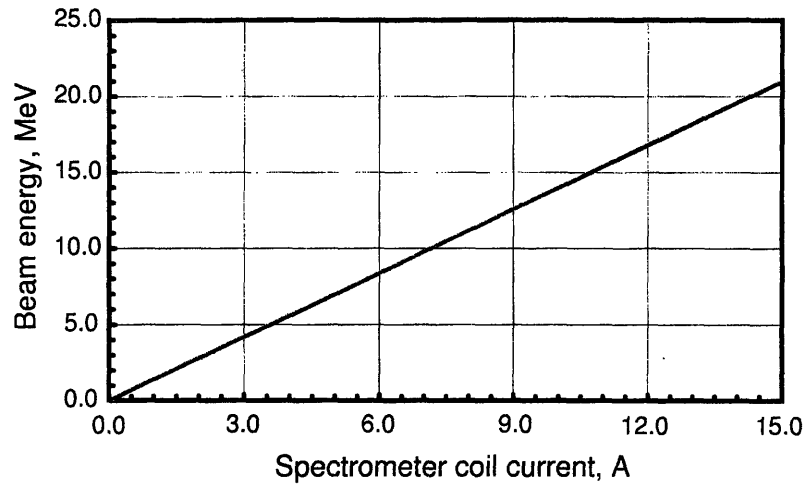
Figure 7-10: Energy of the electron beam entering 30-degree-bend Faraday cup versus spectrometer coil current.
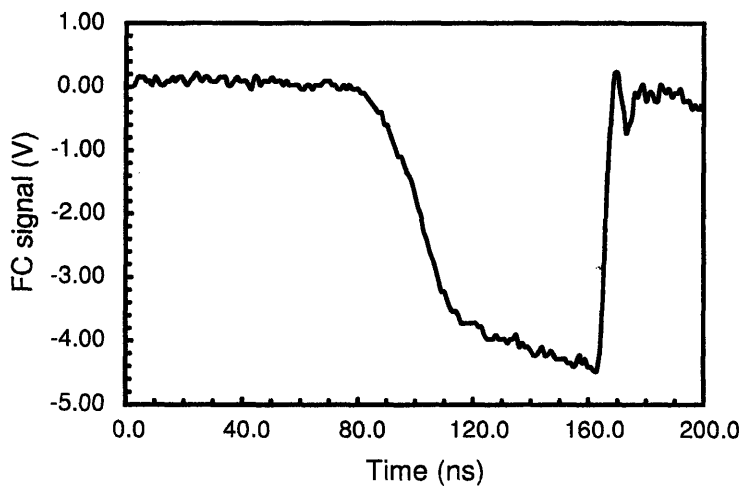
Figure 7-11: Typical Faraday cup signal.
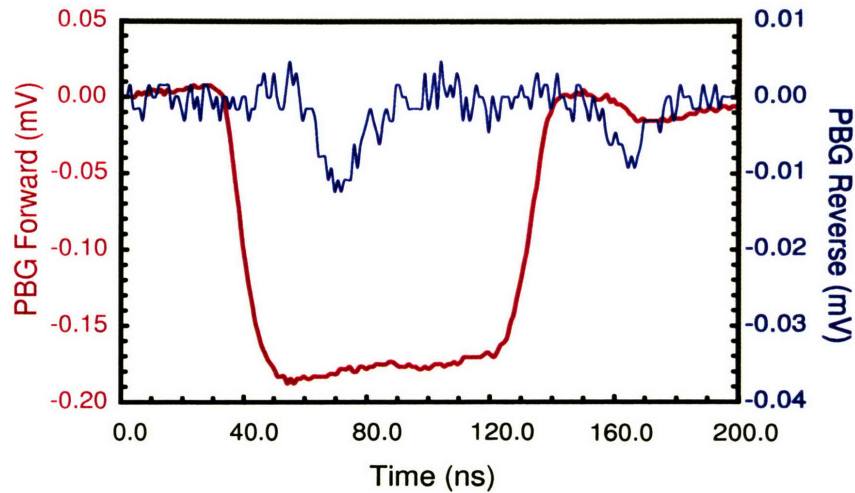
Figure 7-12: Typical PBG forward and reflected signals for 2 MW 100 ns pulse.

figure 7-12. Since the filling time of the PBG structure is of the order of the forward pulse rise time, the amplitude of the reflected signal is low.

The spectrometer coil current was varied in order to measure the beam energy. First, the current was increased slowly, until some signal was seen on the 30-degree-bend Faraday cup (FC2). Different shapes of the 30-degree-bend FC signals are shown in figure 7-13. At the beginning and at the end of electron pulse the linac is not completely filled. Therefore, those parts of electron beam have lower energy, and are seen on the FC2 for lower values of the spectrometer coil current. In the middle of the electron beam pulse (2.81-2.82 μs in figure 7-13) the linac is filled and the beam has high energy and appears on FC2 at high coil current. When the length of the microwave pulse is increased beyond 100 ns the duration of high energy beam part also increases.

Next, we studied the energy spectrum of the electron beam in the middle of the pulse (2.815 μs). The FC2 current at $t = 2.815\mu$s is plotted in figure 7-14 as a function of the spectrometer coil current, which is proportional to the beam energy. The FC2 current value was averaged over 10 shots to reduce the contribution of the shot-to-shot jitter. It can be seen from the figure 7-14 and the spectrometer calibration that the rms energy variation in the middle of the beam is about 0.5 MeV. When high
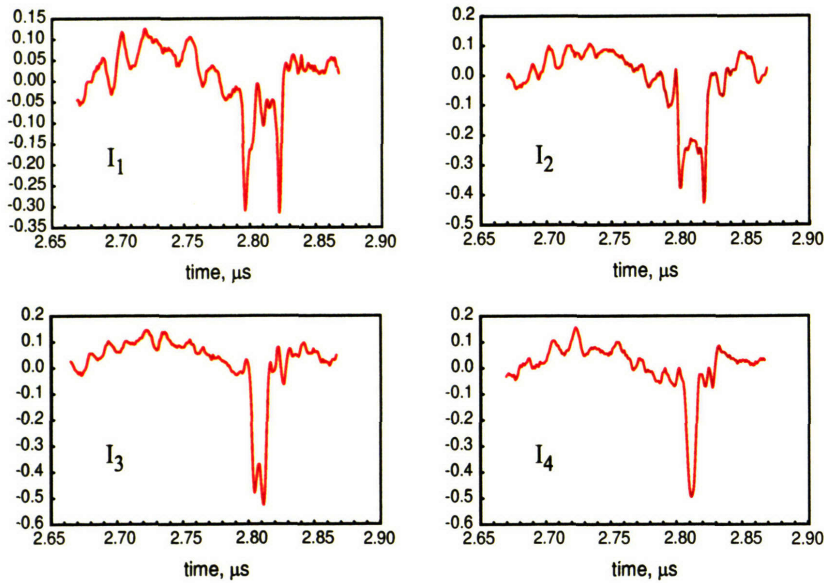
Figure 7-13: Typical 30-degree-bend Faraday cup signals for different values of the spectrometer coil current: $I_1 < I_2 < I_3 < I_4$.

power is coupled into PBG structure, the beam is accelerated. The beam energy increases and the maximum of the FC2 signal shifts towards a higher spectrometer current (figure 7-14). The contribution of the PBG accelerator to the beam energy can be calculated by formula 7.2.

Using the above procedure the electron beam energy was measured for different phase shifts between the linac and the PBG accelerator and for different input powers in the PBG accelerator. The dependence of the electron beam energy on the phase shift between the linac and PBG accelerator is shown in figure 7-15. The PBG input power was approximately 1 MW. The linac beam was initially at 9.4 MeV. The beam was accelerated or decelerated by 1 MeV depending on the phase shift between linac and PBG. The dependence of the beam energy on the gradient (proportional to the square root of the input power) inside PBG structure is shown in figure 7-16. The experimental points in figure 7-16 are connected with a straight line, which is the least squares regression line for the data. In this measurement, the beam exited the linac with the energy of 16.5 MeV. The phase shift between the linac and the PBG was kept 0^0 for the maximum acceleration. Different powers were injected into the
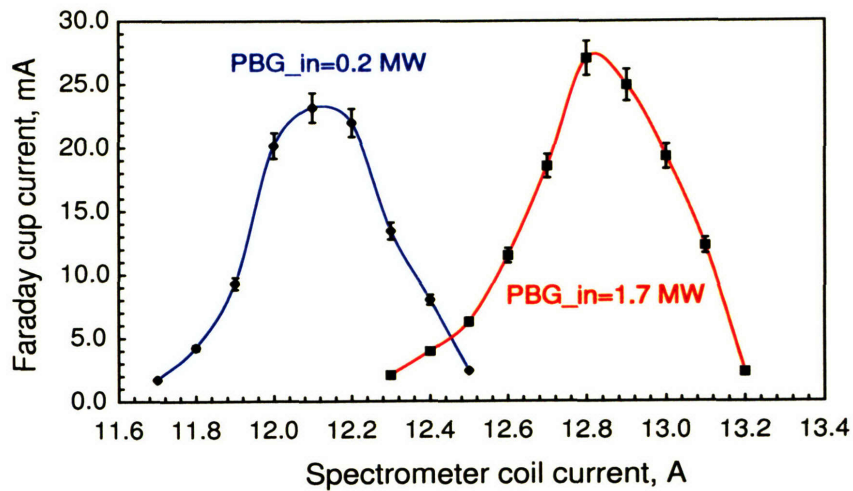
Figure 7-14: 30-degree-bend Faraday cup current in the middle of the electron beam versus spectrometer coil current for different input powers into PBG accelerator.

PBG structure. The electron beam energy was measured for each input power. Based on the HFSS computations, for 2 MW of the input power the accelerating gradients in the PBG structure were expected to be about 35 MV/m. The total length of the PBG accelerator is about 4 mm. Thus the electron energy gain of about 1.4 MeV was expected. A maximum electron beam acceleration inside the PBG structure of about 1.4 MeV was measured for the input power of 2 MW, which is in excellent agreement with the prediction.
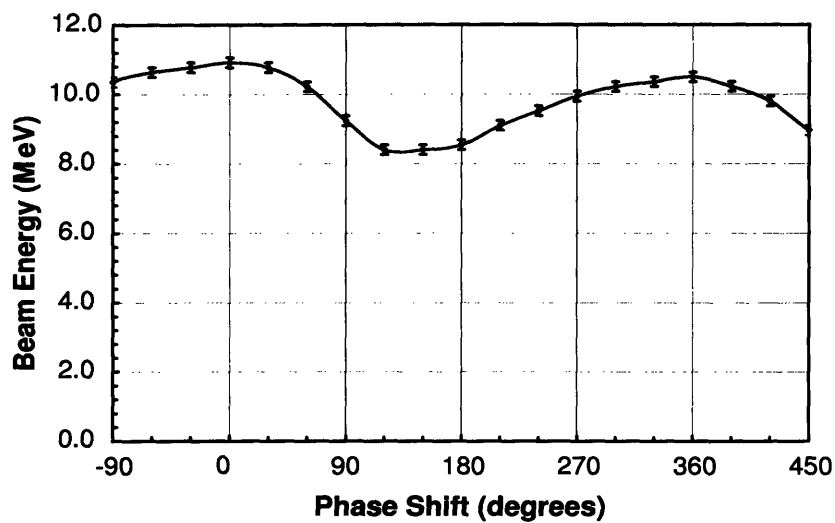
Figure 7-15: Measured electron beam energy versus phase shift between the linac and the PBG accelerator. Input power into PBG accelerator is 1 MW.
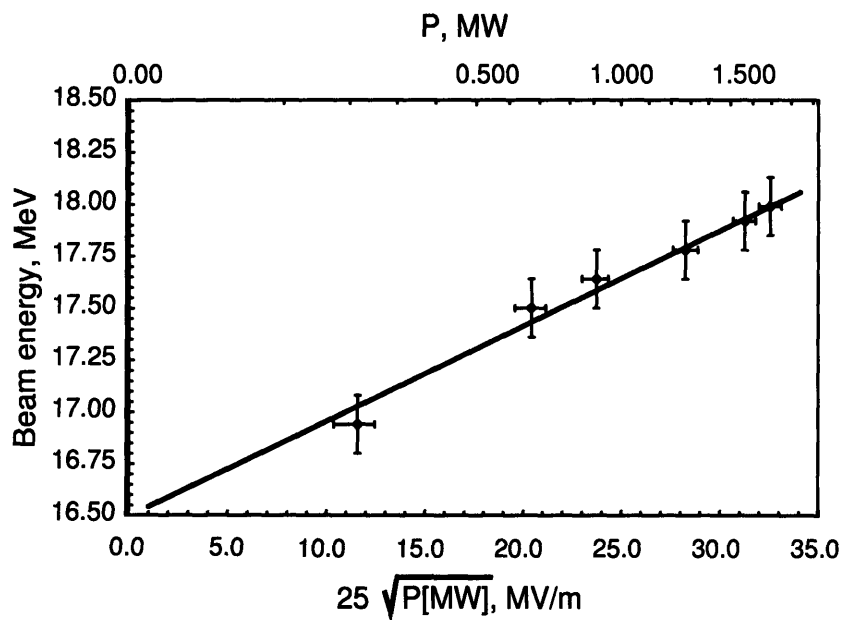
Figure 7-16: Measured electron beam energy versus square root of the PBG accelerator input power.

Chapter 8

Summary

8.1 Conclusion

This thesis research focused on demonstration of a first travelling wave linear photonic band gap accelerator. The unique advantage of the PBG accelerator over the conventional disk-loaded accelerator is in the efficient long-range wakefields suppression. Suppression of wakefields would allow scientists to extend the operating frequencies of future linear colliders to higher frequencies without sacrificing the beam quality. The higher-frequency energy-efficient linear colliders would be able to reach the ever-higher multi-TeV energies and to probe beyond the established picture of particle physics.

The first complete theory of metal photonic band gap structures was developed by the author of this thesis. The band gap pictures for 2D lattices of metallic rods were derived and plotted. Next, 2D PBG resonators were studied and the design of a resonator which would completely suppress the wakefields was presented. Numerous 2D PBG resonators were successfully constructed and tested. Two goals were achieved: the theory of 2D metallic PBG structures and the simulations were benchmarked, and single-mode confinement in a PBG resonator was proven. Engineering efforts were undertaken to successfully demonstrate a high Q PBG resonator. Rods and plates of the resonator were machined of high-purity oxygen-free copper. The rods were brazed into the plates which provided good electrical contact between the

parts of the structure. Measurements of the brazed structure yielded a very high Q_w of 5000, which is in an excellent agreement with the computed number of 5300.

The first ever design of a travelling-wave PBG accelerator structure was performed. The PBG structure consisting of two coupler cell and four travelling wave (TW) cells, which suppressed the wakefields, was modelled successfully with the commercial software package called "High Frequency Structure Simulator (HFSS)". The new PBG coupler had a mode symmetry, which was much better than that available in most conventional couplers. New computational techniques for PBG couplers design were developed. Travelling wave cells were designed without the outer metal wall and with the ratio of the radius of the rods to the spacing between the rods $a/b = 0.155$. This design provided the excellent suppression of higher-order modes. A total of two TW PBG structures were constructed and cold-tested. The first structure was bolted together and although it proved the correctness of computational design, was dominated by high ohmic losses. Therefore, a second structure was built by electroforming methods to reduce ohmic losses. Electroforming proved to be a good technique for fabrication of multi-cell PBG structures and provided us with a first working PBG accelerating structure with low losses. Initially, the electroformed structure was found to resonate at higher frequency than it was designed for. Etching was applied to tune the dimensions of the rods in the PBG accelerator structure which then decreased the resonant frequency to the desired value. Final cold test results for the tuned structure were in perfect agreement with the computations.

To complete this thesis work, the acceleration of an electron beam inside the PBG accelerator was experimentally demonstrated at the MIT accelerator laboratory. The PBG structure was installed on the MIT linac beamline and powered with 2MW of microwaves at 17.140 GHz from the klystron. The structure was successfully conditioned to eliminate electrical breakdowns. The linac electron beam was injected into the PBG structure and accelerated by 1.4 MeV, consistent with the expected accelerating gradients of about 35 MV/m.

8.2 Future directions

Future plans for the linear PBG accelerator research program is the demonstration of a structure, which could be a candidate for a future linear collider section. The following problems must be addressed.

- *The wakefields suppression in a multi-cell structure.* While we experimentally demonstrated the suppression of wakefields in PBG resonators, the demonstration of the wakefields suppression in a travelling wave structure is desirable. The suppression of wakefields by the factor of 100 is needed. One way to demonstrate the wakefield suppression is to conduct a hot test, where two beams pass through the structure: the first beam excites the structure, and the second beam witnesses the wakefields. An example of such experiment is the ASSET in Stanford Linear Accelerator Center (SLAC) (see, for example [43, 44]). To conduct this experiment, the beams with higher charges than those available at MIT are needed. Also, a longer accelerator section than just six cells is required to excite detectable wakefields. The construction of a long PBG accelerator is a big effort. The tuning of a long section has to be performed with the highest possible accuracy. Otherwise, there will be no resonant interaction between the structure and the electron beam. Alternative ideas of wakefield testing (such as the wire method [45]) might also be explored.

- *The electrical breakdown problem.* When high power is coupled into the structure and high surface gradients are achieved, the problem of electrical breakdown arise. The surface gradients are higher when smaller scales are present in the structure. The smallest scales in a PBG accelerator are the diameters of the rods and the irises. By increasing the iris thickness and iris opening diameter, the shunt impedance of the structure decreases. Thus, a longer structure must be build to achieve strong acceleration. The diameter of the rods might be increased in two ways. The first idea is to increase only the diameter of the inner row rods. Then, the PBG structure of the outer rows of rods would not confine the wakefields, while the inner row rods will have higher breakdown threshold.

133

Extensive study of the mode spectrum of such resonators must be performed in order to determine how big the inner rods can be without having the wakefields confined. An alternative idea of increasing the diameter of the rods is to study PBG lattices which are different from the square or the triangular lattices that were explored by the author of this thesis. Different lattices might have different band gap diagrams. Thicker rods do not necessarily lead to the appearance of higher order band gaps and HOM confinement in other lattices.

- *The cooling problem.* Ohmic losses inevitably lead to heating of the copper structure. The heating is stronger when more power is coupled into the structure, or when the microwave pulse is longer and the repetition rate is higher. The heating causes changes in the structure dimension, detunes the accelerator and in time may lead to the distraction of the structure. In conventional linacs, water cooling is usually employed. Cold water is flowing in pipes surrounding the accelerator and cools the hot walls. In a PBG accelerator the inner row of rods would be heated most of all. Cooling with water flowing along the outside wall of the structure would not be efficient. One idea of making the cooling work is to manufacture the inner row rods hollow and pass water inside the copper rods. Electroforming is a natural way of manufacturing hollow rods.

- *The cost problem.* Although the fabrication and tuning of multi-cell PBG structure were successful, the processes of electroforming and etching were rather costly. Engineering efforts must be undertaken in order to develop the cheapest possible processes for electroforming and etching. For example, one may consider electroforming separate cells and cold-testing the cell stack under mechanical pressure without soldering the cells. If the cells are separate, it would be easier to etch individual cells and costly masking will not be needed. Mechanical and electrical engineering knowledge must be employed in order to determine what pressure should be applied to the stack of the cells in order to achieve good electrical contact between the cells, and if the strength of individual cells is sufficient to withstand the pressure.

- *The dispersion problem.* One drawback of applying etching to tune the structure was discovered in the cold tests. In addition to changing the diameters of the rods the etching decreased the plate thickness, thus increasing the dispersion. Increased dispersion did not change the performance of a 6-cell accelerator. But a longer structure would not be able to maintain the resonance between the beam and the electromagnetic wave, if its dispersion was incorrect. In my opinion, the dispersion problem could be resolved if electroforming was used to tune the structure. I would suggest to electroform the structure with undersized rods first, then cold-test it and make a conclusion about how much the dimensions of the cells differ from the correct dimensions. Then I would electroform more copper onto the rods (and, inevitably, the plates) to tune the frequencies of the cells. This would make the structure dispersion more narrow. However, now the size of beam hole can be increased slightly by wire-EDM. Bigger beam hole will compensate for the ticker plates and increase the dispersion.

An alternative direction of research is the study of dielectric PBG resonators. Dielectrics are really attractive for high frequency accelerators, because of lower losses at high frequencies and higher breakdown limits. The theory of 2D dielectric PBG lattices is well developed. However, manufacturing of dielectric PBG resonators at X- and K-bands has not yet been studied. In addition, in a dielectric PBG structure it is possible to confine a higher order (for example, TM_{02}) accelerating mode without having lower order wakefield modes confined [46]. Therefore, it is possible to go to higher frequencies without going to smaller accelerating structures which are hard to manufacture, tune and cool.

Appendix A

Wake fields excitation by a point charge

A.1 Introduction

In this appendix the expressions for the wake potentials are re-derived. The expressions were initially published by Bane et al. in [4]. First, the witness charge following the first charge along the same path will be considered. Then the generalization for the case of parallel paths will be performed for the special case of cavity with translational symmetry. Finally the Panofsky-Wenzel theorem will be derived.

A.2 Normal mode expansion of fields in the cavity

A closed, empty cavity with perfectly conducting walls is considered. An exciting particle with charge Q traverses the cavity at velocity $v = c$. The cavity axis is arranged so that the charge enters the cavity at $z = 0$ at time $t = 0$, follows along the z-axis and leaves at $z = L$. The test charge follows the same path at the distance s behind the exciting charge (see figure A-1)

The calculations are based on the following Maxwell equations, written in mks
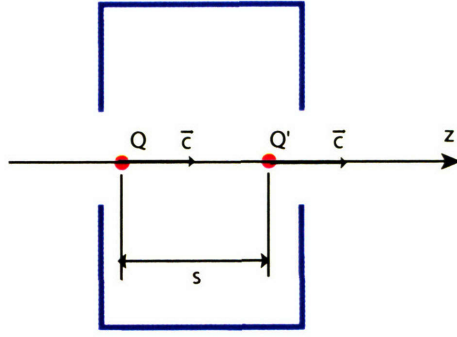
Figure A-1: The cavity and two charges entering along the same path: the first charge is exciting the cavity and the second charge is the test charge

units:

$$\vec{\nabla} \times \vec{B} = \mu_0 \vec{j} + \frac{1}{c^2} \frac{\partial \vec{E}}{\partial t}, \tag{A.1}$$

$$\vec{\nabla} \cdot \vec{E} = \frac{\rho}{\varepsilon_0}. \tag{A.2}$$

The electric field $\vec{E}(\vec{x}, t)$ and magnetic induction $\vec{B}(\vec{x}, t)$ can be written in terms of a vector potential $\vec{A}(\vec{x}, t)$ and a scalar potential $\Phi(\vec{x}, t)$ as

$$\vec{B} = \vec{\nabla} \times \vec{A}, \; \vec{E} = -\frac{\partial \vec{A}}{\partial t} - \vec{\nabla}\Phi. \tag{A.3}$$

Plug the potentials to the Maxwell equation and use the Coulomb gauge ($\vec{\nabla} \cdot \vec{A} = 0$). This yields

$$\vec{\nabla}^2 \vec{A} - \frac{1}{c^2} \frac{\partial^2 \vec{A}}{\partial t^2} - \frac{1}{c^2} \frac{\partial}{\partial t} \vec{\nabla}\Phi = -\mu_0 \vec{j}. \tag{A.4}$$

The vector potential can be expanded into the set of $\vec{a}_\lambda(\vec{x})$

$$\vec{A}(\vec{x}, t) = \sum_\lambda q_\lambda(t) \, \vec{a}_\lambda(\vec{x}), \tag{A.5}$$

where $\vec{a}_\lambda(\vec{x})$ satisfy the following equation and boundary conditions on the metallic

surface of the cavity:

$$\vec{\nabla}^2 \vec{a}_\lambda + \frac{\omega_\lambda^2}{c^2} \vec{a}_\lambda = 0, \tag{A.6}$$

$$\vec{a}_\lambda \times \hat{n}|_S = 0. \tag{A.7}$$

To satisfy the Coulomb gauge for the vector potential it is also required that

$$\vec{\nabla} \cdot \vec{a}_\lambda = 0. \tag{A.8}$$

Similarly, we expand the scalar potential as

$$\Phi(\vec{x}, t) = \sum_\lambda r_\lambda(t) \phi_\lambda(\vec{x}), \tag{A.9}$$

where $\phi_\lambda(\vec{x})$ satisfy the following equation and boundary conditions on the metallic surface of the cavity:

$$\vec{\nabla}^2 \phi_\lambda + \frac{\Omega_\lambda^2}{c^2} \phi_\lambda = 0, \tag{A.10}$$

$$\phi_\lambda|_S = 0. \tag{A.11}$$

The set of equations (A.6),(A.7) and (A.8) ((A.10) and (A.11)) defines the Strum-Liouville problem which has the solution representing a set of eigenvalues ω_λ (Ω_λ) with a consequent set of eigenfunctions $\vec{a}_\lambda$ (ϕ_λ). The eigenvectors $\vec{a}_\lambda$ (ϕ_λ) are orthogonal and the set of eigenvectors is complete, thus they can be used to compose any $\vec{A}(\vec{x}, t)$ ($\Phi(\vec{x}, t)$) at any particular instant of time. Note, that in general $\omega_\lambda \neq \Omega_\lambda$. Any series

$$\vec{E} = -\sum_\lambda \left(\frac{\partial q_\lambda(t)}{\partial t} \vec{a}_\lambda + r_\lambda(t) \vec{\nabla} \phi_\lambda(\vec{x}) \right) \tag{A.12}$$

will automatically satisfy the metallic boundary condition:

$$\vec{E} \times \hat{n}\Big|_S = -\sum_\lambda \left(\frac{\partial q_\lambda(t)}{\partial t} \vec{a}_\lambda \times \hat{n}|_S + r_\lambda(t) \vec{\nabla} \phi_\lambda(\vec{x}) \times \hat{n}\Big|_S \right) = 0.$$

Substituting the series for $\vec{A}$ and Φ into Eq. (A.4) gives

$$\sum_\lambda \left(q_\lambda \vec{\nabla}^2 \vec{a}_\lambda - \vec{a}_\lambda \frac{1}{c^2} \frac{\partial^2 q_\lambda}{\partial t^2} - \frac{1}{c^2} \frac{\partial}{\partial t} r_\lambda \vec{\nabla} \phi_\lambda \right) = -\mu_0 \vec{j}, \qquad \text{(A.13)}$$

which using the Eqs (A.6) and (A.10) can be rewritten as

$$\sum_\lambda \left(\vec{a}_\lambda \left(q_\lambda \omega_\lambda^2 + \ddot{q}_\lambda \right) + \dot{r}_\lambda \vec{\nabla} \phi_\lambda \right) = \mu_0 c^2 \vec{j}. \qquad \text{(A.14)}$$

In the next equation of the paper the summation over λ is omitted, which is incorrect. Dotting Eq.(A.14) with $\vec{a}_{\lambda'}$ and integrating over the cavity volume V gives

$$\sum_\lambda \left(\left(q_\lambda \omega_\lambda^2 + \ddot{q}_\lambda \right) \int_V \vec{a}_\lambda \cdot \vec{a}_{\lambda'} dV + \dot{r}_\lambda \int_V \vec{\nabla} \phi_\lambda \cdot \vec{a}_{\lambda'} dV \right) = \mu_0 c^2 \int_V \vec{j} \cdot \vec{a}_{\lambda'} dV. \quad \text{(A.15)}$$

The second integral of Eq.(A.15) can be written as

$$\int_V \vec{\nabla} \phi_\lambda \cdot \vec{a}_{\lambda'} dV = \int_S \phi_\lambda \vec{a}_{\lambda'} \cdot d\vec{S} - \int_V \phi_\lambda \left(\vec{\nabla} \cdot \vec{a}_{\lambda'} \right) dV$$

The first integral on the right vanished since $\phi_\lambda = 0$ on the boundary, the second term vanishes because of the gauge (A.8). Normalize $\vec{a}_\lambda$ as

$$\int_V \vec{a}_\lambda \cdot \vec{a}_{\lambda'} dV = \frac{2U_\lambda}{\varepsilon_0} \delta_{\lambda\lambda'}. \qquad \text{(A.17)}$$

Note, that $\varepsilon_0 \mu_0 c^2 = 1$. The equation (A.15) becomes simply

$$\ddot{q}_\lambda + q_\lambda \omega_\lambda^2 = \frac{1}{2U_\lambda} \int_V \vec{j} \cdot \vec{a}_\lambda dV. \qquad \text{(A.18)}$$

Note, that whenever there is no current in the cavity the q_λ vary sinusoidally at frequencies ω_λ

$$q_\lambda = C_\lambda \cos \left(\omega_\lambda t + \theta_\lambda \right).$$

In this case $\vec{A}$ is written as

$$\vec{A}\left(\vec{x}, t\right) = \sum_{\lambda} C_{\lambda} \vec{a}_{\lambda}\left(\vec{x}\right) \cos\left(\omega_{\lambda} t + \theta_{\lambda}\right), \qquad (A.19)$$

which means, that $\vec{a}_{\lambda}\left(\vec{x}\right)$ are the eigenmodes of the empty cavity and corresponding ω_{λ} are the resonant frequencies.

Similarly, beginning with the Maxwell equation (A.2) and plugging the expression of $\vec{E}$ through the potentials (A.3) we get

$$\vec{\nabla} \cdot \left(\frac{\partial \vec{A}}{\partial t} + \vec{\nabla}\Phi\right) = -\frac{\rho}{\varepsilon_0}. \qquad (A.20)$$

Using the expansions (A.5) and (A.9) yields

$$\sum_{\lambda} \left(\frac{\partial q_{\lambda}}{\partial t} \vec{\nabla} \cdot \vec{a}_{\lambda} + r_{\lambda}\left(t\right) \vec{\nabla}^2 \phi_{\lambda}\left(\vec{x}\right)\right) = -\frac{\rho}{\varepsilon_0}. \qquad (A.21)$$

Dotting Eq.(A.21) with $\phi_{\lambda'}$ and integrating over the cavity volume V gives

$$\sum_{\lambda} \left(\frac{\partial q_{\lambda}}{\partial t} \int_V \left(\vec{\nabla} \cdot \vec{a}_{\lambda}\right) \phi_{\lambda'} dV + r_{\lambda}\left(t\right) \int_V \vec{\nabla}^2 \phi_{\lambda}\left(\vec{x}\right) \phi_{\lambda'} dV\right) = -\frac{1}{\varepsilon_0} \int_V \rho \phi_{\lambda'} dV. \quad (A.22)$$

The first integral in Eq.(A.22) vanishes because of the gauge (A.8), the second integral can be rewritten as

$$\int_V \vec{\nabla}^2 \phi_{\lambda}\left(\vec{x}\right) \phi_{\lambda'} dV = \int_S \phi_{\lambda'} \vec{\nabla} \phi_{\lambda}\left(\vec{x}\right) \cdot d\vec{S} - \int_V \vec{\nabla} \phi_{\lambda}\left(\vec{x}\right) \cdot \vec{\nabla} \phi_{\lambda'} dV. \qquad (A.23)$$

The first integral in (A.23) is zero due to the boundary conditions (A.11). Let the ϕ_{λ} are normalized by

$$\int_V \vec{\nabla} \phi_{\lambda}\left(\vec{x}\right) \cdot \vec{\nabla} \phi_{\lambda'} dV = \frac{2T_{\lambda}}{\varepsilon_0} \delta_{\lambda\lambda'}. \qquad (A.24)$$

Thus the equation (A.22) becomes

$$r_{\lambda}\left(t\right) = \frac{1}{2T_{\lambda}} \int_V \rho \phi_{\lambda} dV. \qquad (A.25)$$

140

Whenever there are no charges in the cavity, all the r_λ (and thus also Φ) are zero.

Given the homogeneous solutions $\vec{a}_\lambda$, ϕ_λ and the sources $\vec{j}$, ρ we can solve for the q_λ, r_λ form Eqs (A.18) and (A.25). These in turn allow us to solve for $\vec{E}$ and $\vec{B}$ by the way of Eqs. (A.3), (A.5), and (A.9). So the magnetic induction and the electric field are given by

$$\vec{B} = \sum_\lambda q_\lambda(t) \left(\vec{\nabla} \times \vec{a}_\lambda(\vec{x}) \right), \tag{A.26}$$

$$\vec{E} = -\sum_\lambda \left(\dot{q}_\lambda(t) \vec{a}_\lambda(\vec{x}) + r_\lambda(t) \vec{\nabla}\phi_\lambda(\vec{x}) \right). \tag{A.27}$$

The energy, stored in the cavity is given by

$$\mathcal{E} = \frac{1}{2} \int_V \left(\varepsilon_0 E^2 + B^2/\mu_0 \right) dV \tag{A.28}$$

$$= \frac{1}{2} \sum_{\lambda,\lambda'} \varepsilon_0 \left(\dot{q}_\lambda(t) \dot{q}_{\lambda'}(t) \int_V \vec{a}_\lambda(\vec{x}) \cdot \vec{a}_{\lambda'}(\vec{x}) \, dV \right.$$

$$\left. +2\dot{q}_\lambda(t) r_{\lambda'}(t) \int_V \vec{a}_\lambda(\vec{x}) \cdot \vec{\nabla}\phi_\lambda(\vec{x}) \, dV + r_\lambda(t) r_{\lambda'}(t) \int_V \vec{\nabla}\phi_\lambda(\vec{x}) \cdot \vec{\nabla}\phi_{\lambda'}(\vec{x}) \, dV \right)$$

$$+\frac{1}{2} \sum_{\lambda,\lambda'} q_\lambda(t) q_{\lambda'}(t) \int_V \left(\vec{\nabla} \times \vec{a}_\lambda(\vec{x}) \right) \cdot \left(\vec{\nabla} \times \vec{a}_{\lambda'}(\vec{x}) \right) /\mu_0 \, dV.$$

We proved above, that $\int_V \vec{a}_\lambda(\vec{x}) \cdot \vec{\nabla}\phi_\lambda(\vec{x}) \, dV = 0$. Using the normalization conditions (A.17) and (A.24) we rewrite the expression for stored energy as

$$\mathcal{E} = \sum_\lambda \left(\dot{q}_\lambda^2 U_\lambda + r_\lambda^2 T_\lambda \right)$$

$$+\frac{1}{2} \sum_{\lambda,\lambda'} q_\lambda(t) q_{\lambda'}(t) \int_V \left(\vec{\nabla} \times \vec{a}_\lambda(\vec{x}) \right) \cdot \left(\vec{\nabla} \times \vec{a}_{\lambda'}(\vec{x}) \right) /\mu_0 \, dV.$$

Use the facts, that

$$\left(\vec{\nabla} \times \vec{a}_\lambda \right) \cdot \left(\vec{\nabla} \times \vec{a}_{\lambda'} \right) = \vec{\nabla} \left(\vec{a}_{\lambda'} \times \left(\vec{\nabla} \times \vec{a}_\lambda \right) \right) + \vec{a}_{\lambda'} \left(\vec{\nabla} \times \left(\vec{\nabla} \times \vec{a}_\lambda \right) \right),$$

and that

$$\left(\vec{\nabla} \times \left(\vec{\nabla} \times \vec{a}_\lambda\right)\right) = -\vec{\nabla}^2 \vec{a}_\lambda = \frac{\omega_\lambda^2}{c^2} \vec{a}_\lambda.$$

We write the last integral as

$$\int_V \left(\vec{\nabla} \times \vec{a}_\lambda\left(\vec{x}\right)\right) \cdot \left(\vec{\nabla} \times \vec{a}_{\lambda'}\left(\vec{x}\right)\right) dV$$

$$= \int_V \vec{\nabla}\left(\vec{a}_{\lambda'} \times \left(\vec{\nabla} \times \vec{a}_\lambda\right)\right) dV + \frac{\omega_\lambda^2}{c^2} \int_V \vec{a}_\lambda dV.$$

The first integral in the sum is proved to be zero due to the boundary conditions (A.7):

$$\int_V \vec{\nabla}\left(\vec{a}_{\lambda'} \times \left(\vec{\nabla} \times \vec{a}_\lambda\right)\right) dV = \int_S \left(\vec{a}_{\lambda'} \times \left(\vec{\nabla} \times \vec{a}_\lambda\right)\right) \cdot d\vec{S}$$

$$= \int_S \left(\vec{\nabla} \times \vec{a}_\lambda\right) \cdot \left(\vec{a}_{\lambda'} \times d\vec{S}\right) = 0.$$

Thus the stored energy

$$\mathcal{E} = \sum_\lambda \left(\left(\dot{q}_\lambda^2 + \omega_\lambda^2 q_\lambda^2\right) U_\lambda + r_\lambda^2 T_\lambda\right). \tag{A.29}$$

A.3   The longitudinal wake potential

The delta-function longitudinal wake potential is defined by (4.1). For now we consider the case of $\vec{r} = \vec{r'} = 0$. To calculate W_z first find the fields in the cavity due to the exciting charge. The source terms due to the exciting charge are

$$\rho\left(\vec{x}, t\right) = Q\delta\left(x\right)\delta\left(y\right)\delta\left(z - ct\right), \tag{A.30}$$

$$\vec{j}\left(\vec{x}, t\right) = \hat{z}c\rho\left(\vec{x}, t\right).$$

Eq. (A.18) becomes

$$\ddot{q}_\lambda + q_\lambda \omega_\lambda^2 = \frac{1}{2U_\lambda} \int_V \vec{j} \cdot \vec{a}_\lambda dV$$

$$= \frac{cQ}{2U_\lambda} \int_V a_{\lambda z} \delta(x) \delta(y) \delta(z - ct) dV \qquad (A.31)$$

$$= \frac{cQ}{2U_\lambda} \begin{cases} 0, & t < 0 \\ a_{\lambda z}(0,0,ct), & 0 < t < L/c \\ 0, & t > L/c \end{cases},$$

where L is the cavity length, $a_{\lambda z}(x, y, z)$ is the $z-$component of $\vec{a}_\lambda$. Solve Eq. (A.31) using the initial conditions $q(0) = \dot{q}(0) = 0$ (no fields in the cavity before the charge enters). For $t < 0$ and $t > L/c$ the equation is homogeneous and the solution is

$$\begin{cases} q_\lambda \equiv 0, & t < 0 \\ q_\lambda = q_\lambda(t = L/c) \cos \omega_\lambda(t - L/c) + \frac{\dot{q}_\lambda(t=L/c)}{\omega_\lambda} \sin \omega_\lambda(t - L/c), & t > L/c \end{cases}.$$

For $0 < t < L/c$ solve the equation by the variation of parameters. Seek for the solution in form

$$q_\lambda = \alpha(t) \sin \omega_\lambda t + \beta(t) \cos \omega_\lambda t.$$

Plugging this form of solution to the Eq. (A.31) for $0 < t < L/c$ and the boundary conditions, we obtain the system of equations for $\alpha(t)$, $\beta(t)$

$$\begin{cases} \alpha'(t) \sin \omega_\lambda t + \beta'(t) \cos \omega_\lambda t = 0 \\ \omega_\lambda(\alpha'(t) \cos \omega_\lambda t - \beta'(t)) \sin \omega_\lambda t = \frac{cQ}{2U_\lambda} a_{\lambda z}(0,0,ct) \end{cases},$$

$$\alpha(0) = \beta(0) = 0.$$

The solution is

$$\alpha\left(t\right) = \frac{cQ}{2U_\lambda\omega_\lambda}\int_0^t a_{\lambda z}\left(0,0,ct'\right)\cos\omega_\lambda t'dt',$$

$$\beta\left(t\right) = -\frac{cQ}{2U_\lambda\omega_\lambda}\int_0^t a_{\lambda z}\left(0,0,ct'\right)\sin\omega_\lambda t'dt',$$

$$q_\lambda = \frac{cQ}{2U_\lambda\omega_\lambda}\int_0^t a_{\lambda z}\left(0,0,ct'\right)\sin\omega_\lambda\left(t-t'\right)dt'.$$

The solution valid for all t

$$q_\lambda\left(t\right) = \frac{cQ}{2U_\lambda\omega_\lambda}\int_0^{\min(t,L/c)} a_{\lambda z}\left(0,0,ct'\right)\sin\omega_\lambda\left(t-t'\right)dt'. \tag{A.32}$$

Similarly, substitution of (A.30) to (A.25) yields

$$\begin{aligned}
r_\lambda\left(t\right) &= \frac{1}{2T_\lambda}\int_V Q\delta\left(x\right)\delta\left(y\right)\delta\left(z-ct\right)\phi_\lambda dV \\
&= \frac{Q}{2T_\lambda}\begin{cases} 0, & t<0 \\ \phi_\lambda\left(0,0,ct\right), & 0<t<L/c \\ 0, & t>L/c \end{cases}
\end{aligned} \tag{A.33}$$

With the above two equations and the equations (A.26), (A.27), and (A.29) it is possible to construct the fields and stored energy due to the exciting charge in terms of the empty cavity solutions ϕ_λ, $\vec{a}_\lambda$, ω_λ.

The energy left in the cavity after the exciting charge left $(t > L/c)$ can be easily calculated from (A.29)

$$\begin{aligned}
\mathcal{E} &= \sum_\lambda\left(\dot{q}_\lambda^2+\omega_\lambda^2 q_\lambda^2\right)U_\lambda \tag{A.34} \\
&= Q^2\sum_\lambda\frac{1}{4U_\lambda}\int_0^L\int_0^L dz'\,dz''a_{\lambda z}\left(0,0,z'\right)a_{\lambda z}\left(0,0,z''\right)\cos\frac{\omega_\lambda\left(z''-z'\right)}{c}.
\end{aligned}$$

Introduce

$$V_\lambda = \int_0^L dz\exp\left(i\omega_\lambda z/c\right)a_{\lambda z}\left(0,0,z\right). \tag{A.35}$$

$$|V_\lambda|^2 = \int_0^L \int_0^L dz' \, dz'' a_{\lambda z} (0, 0, z') \, a_{\lambda z} (0, 0, z'') \cos \frac{\omega_\lambda (z'' - z')}{c}.$$

Comparing the last expression with (A.34) we obtain

$$\mathcal{E} = Q^2 \sum_\lambda \frac{|V_\lambda|^2}{4U_\lambda}. \tag{A.36}$$

Define the loss factor as

$$k_\lambda = \frac{|V_\lambda|^2}{4U_\lambda}. \tag{A.37}$$

The stored energy becomes simply

$$\mathcal{E} = Q^2 \sum_\lambda k_\lambda. \tag{A.38}$$

Thus k_λ gives the amount of energy deposited in mode λ by the exciting charge.

Now calculate the wake potential W_z. Plug (A.27) to (4.1):

$$W_z (s) = \frac{1}{Q} \sum_\lambda \int_0^L \left(\dot{q}_\lambda \left(\frac{z + s}{c} \right) a_{\lambda z} (z) + r_\lambda \left(\frac{z + s}{c} \right) \frac{\partial}{\partial z} \phi_\lambda (z) \right), \tag{A.39}$$

where $a_{\lambda z} (z) = a_{\lambda z} (0, 0, z)$, $\phi_\lambda (z) = \phi_\lambda (0, 0, z)$. Substituting q_λ, r_λ from Eqs. (A.32) and (A.33) will give the final result. The problem is naturally solved in four pieces:

a) $s > L$: The test charge enters after the exciting charge has already left the cavity.

In this case

$$r_\lambda \left(\frac{z + s}{c} \right) = 0,$$

$$\dot{q}_\lambda \left(\frac{z + s}{c} \right) = \frac{Q}{2U_\lambda} \int_0^L a_{\lambda z} (z') \cos \frac{\omega_\lambda (z + s - z')}{c} dz',$$

$$W_z (s) = \sum_\lambda \frac{1}{2U_\lambda} \int_0^L \int_0^L a_{\lambda z} (z) \, a_{\lambda z} (z') \cos \frac{\omega_\lambda (z + s - z')}{c} dz' dz.$$

145

Compare the last integral with

$$\text{Re}\left\{V_\lambda V_\lambda^* \exp\left(i\omega_\lambda s/c\right)\right\}$$
$$= \int_0^L \int_0^L dz' dz \cos\left(\frac{\omega_\lambda\left(z - z' + s\right)}{c}\right) a_{\lambda z}\left(z\right) a_{\lambda z}\left(z'\right).$$

So we find the longitudinal wake potential for $s > L$:

$$
\begin{aligned}
W_z\left(s\right) &= \sum_\lambda \frac{1}{2U_\lambda} \text{Re}\left\{V_\lambda V_\lambda^* \exp\left(i\omega_\lambda s/c\right)\right\} \\
&= \sum_\lambda \frac{|V_\lambda|^2}{2U_\lambda} \cos\frac{\omega_\lambda s}{c} = \sum_\lambda 2k_\lambda \cos\frac{\omega_\lambda s}{c}.
\end{aligned}
\tag{A.40}
$$

b) $0 < s < L$: The test charge enters while the exciting charge is still in the cavity. Here

$$r_\lambda\left(\frac{z + s}{c}\right) = \frac{Q}{2T_\lambda}\phi_\lambda\left(z + s\right),$$

$$\dot{q}_\lambda\left(\frac{z + s}{c}\right) = \frac{Q}{2U_\lambda}\int_0^{\min(z+s,L)} a_{\lambda z}\left(z'\right) \cos\frac{\omega_\lambda\left(z + s - z'\right)}{c} dz',$$

$$
\begin{aligned}
W_z\left(s\right) &= \sum_\lambda \frac{1}{2U_\lambda}\int_0^L dz \int_0^{\min(z+s,L)} dz' a_{\lambda z}\left(z\right) a_{\lambda z}\left(z'\right) \cos\frac{\omega_\lambda\left(z + s - z'\right)}{c} \\
&\quad + \sum_\lambda \int_0^L \frac{1}{2T_\lambda}\phi_\lambda\left(z + s\right)\frac{\partial}{\partial z}\phi_\lambda\left(z\right) dz \\
&= \sum_\lambda \left(\frac{I_{1\lambda}\left(s\right) - I_{2\lambda}\left(s\right)}{2U_\lambda} + \frac{K_{1\lambda}\left(s\right)}{2T_\lambda}\right),
\end{aligned}
\tag{A.41}
$$

146

where

$$
\begin{aligned}
I_{1\lambda}(s) &= \int_0^L \int_0^L a_{\lambda z}(z)\, a_{\lambda z}(z') \cos \frac{\omega_\lambda (z + s - z')}{c} dz' dz \\
&= \operatorname{Re}\left\{ V_\lambda V_\lambda^* \exp\left(i\omega_\lambda s/c\right) \right\}, \\
I_{2\lambda}(s) &= \int_0^L dz \int_{\min(z+s,L)}^L dz'\, a_{\lambda z}(z)\, a_{\lambda z}(z') \cos \frac{\omega_\lambda (z + s - z')}{c} \\
&= \int_0^{L-s} dz \int_{z+s}^L dz'\, a_{\lambda z}(z)\, a_{\lambda z}(z') \cos \frac{\omega_\lambda (z + s - z')}{c}, \\
K_{1\lambda}(s) &= \int_0^L \phi_\lambda(z+s)\, \frac{\partial}{\partial z}\phi_\lambda(z)\, dz \\
&= \int_0^{L-s} \phi_\lambda(z+s)\, \frac{\partial}{\partial z}\phi_\lambda(z)\, dz, \text{ since } \phi_\lambda(z+s) = 0 \text{ for } z > L - s.
\end{aligned}
$$

The causality requires, that the wake potential is zero for $s < 0$. In particular, in the range $-L < s < 0$ it yields

$$
r_\lambda\left(\frac{z+s}{c}\right) = \frac{Q}{2T_\lambda}\phi_\lambda(z+s)\,\vartheta(z+s), \quad \vartheta(z) \text{ is the Step-function,}
$$

$$
\dot{q}_\lambda\left(\frac{z+s}{c}\right) = \frac{Q}{2U_\lambda}\int_0^{\max(0,z+s)} a_{\lambda z}(z') \cos \frac{\omega_\lambda(z+s-z')}{c} dz',
$$

$$
W_z(s) = \sum_\lambda \frac{1}{2U_\lambda}\int_0^L dz \int_0^{\max(0,z+s)} dz'\, a_{\lambda z}(z)\, a_{\lambda z}(z') \cos \frac{\omega_\lambda(z+s-z')}{c}
$$

$$
+ \sum_\lambda \int_{-s}^L \frac{1}{2T_\lambda}\phi_\lambda(z+s)\, \frac{\partial}{\partial z}\phi_\lambda(z)\, dz = \sum_\lambda \left(\frac{I_{3\lambda}(s)}{2U_\lambda} + \frac{K_{2\lambda}(s)}{2T_\lambda}\right) = 0,
$$

where

$$
\begin{aligned}
I_{3\lambda}(s) &= \int_0^L dz \int_0^{\max(0,z+s)} dz'\, a_{\lambda z}(z)\, a_{\lambda z}(z') \cos \frac{\omega_\lambda(z+s-z')}{c} \\
&= \int_0^{L+s} dz \int_{z-s}^L dz'\, a_{\lambda z}(z)\, a_{\lambda z}(z') \cos \frac{\omega_\lambda(z-s-z')}{c} = I_{2\lambda}(-s),
\end{aligned}
$$

$$
K_{2\lambda}(s) = \int_{-s}^L \phi_\lambda(z+s)\, \frac{\partial}{\partial z}\phi_\lambda(z)\, dz.
$$

Integrate by parts

$$
\begin{aligned}
K_{2\lambda}(s) &= -\int_{-s}^{L} \phi_\lambda(z) \frac{\partial}{\partial z} \phi_\lambda(z+s)\, dz \\
&= -\int_{0}^{L+s} \phi_\lambda(z-s) \frac{\partial}{\partial z} \phi_\lambda(z)\, dz = -K_{1\lambda}(-s).
\end{aligned}
$$

Thus

$$
\sum_\lambda \left(\frac{I_{2\lambda}(s)}{2U_\lambda} - \frac{K_{1\lambda}(s)}{2T_\lambda} \right) = 0 \tag{A.42}
$$

for $0 < z < L$. So the equation (A.41) becomes

$$
W_z(s) = \sum_\lambda \frac{I_{1\lambda}(s)}{2U_\lambda} = \sum_\lambda 2k_\lambda \cos \frac{\omega_\lambda s}{c}. \tag{A.43}
$$

Note, that the longitudinal wake potential for $0 < z < L$ has the same form as the longitudinal wake potential for $z > L$.

c) $s < 0$. The test charge enters before the exciting charge. From causality

$$
W_z(s) = 0, \quad s < 0. \tag{A.44}
$$

d) $s = 0$. $W_z(0)$ can be interpreted as the voltage the exciting charge itself loses to the cavity, divided by the charge Q. It can be seen from (A.38), that the voltage loss of a charge to mode λ is $k_\lambda Q$. Thus

$$
W_z(0) = \sum_\lambda k_\lambda. \tag{A.45}
$$

Summarizing the results, given by the equations (A.40), (A.43), (A.44), and (A.45) the final answer for the longitudinal wake potential can be written:

$$
W_z(s) = \sum_\lambda k_\lambda \cos \frac{\omega_\lambda s}{c} \begin{cases} 0, & s < 0 \\ 1, & s = 0 \\ 2, & s > 0 \end{cases}. \tag{A.46}
$$

Note that due to the symmetry introduced by taking the velocities to be c, W_z does not depend on the scalar potential solutions ϕ_λ, even if the test charge enters while the exciting charge is still in the cavity. Note also that, since W_z is expressible as a sum of cosines, its maximum value is at $s = +0$.

A.4   The transverse wake potential

The delta-function transverse wake potential is defined by (4.2). Express $\vec{E}$ and $\vec{B}$ in terms of vector-potentials and plug to (4.2)

$$
\begin{aligned}
\vec{W}_\perp(s) &= \frac{1}{Q} \int_0^L dz \left[-\frac{\partial \vec{A}_\perp}{\partial t} - \vec{\nabla}_\perp \Phi + \left(\vec{v} \times \left(\vec{\nabla} \times \vec{A} \right) \right)_\perp \right]_{t=(z+s)/c} \\
&= \frac{1}{Q} \int_0^L dz \left(c\vec{\nabla}_\perp A_z - \vec{\nabla}_\perp \Phi \right)_{t=(z+s)/c} - \frac{c}{Q} \left. \vec{A}_\perp \right|_{z=0,\,t=s/c}^{z=L,\,t=(L+s)/c} .
\end{aligned}
$$

For cavities with walls perpendicular to the $z-$axis at $z = 0$ and $z = L$ the boundary conditions are $\vec{E}_\perp(z = 0) = \vec{E}_\perp(z = L) = 0$ and thus the boundary term is expression for $\vec{W}_\perp$ vanishes

$$
\vec{W}_\perp(s) = \frac{1}{Q} \int_0^L dz \left(c\vec{\nabla}_\perp A_z - \vec{\nabla}_\perp \Phi \right)_{t=(z+s)/c} . \tag{A.47}
$$

Analogously to the longitudinal case, $\vec{W}_\perp$ can be used as a Green's function for transverse momentum kick per total charge within an ultra-relativistic bunch of arbitrary shape.

Plug the series (A.5) and (A.9) to (A.47):

$$
\vec{W}_\perp(s) = \frac{1}{Q} \sum_\lambda \int_0^L dz \left(cq_\lambda \left(\frac{z+s}{c} \right) \vec{\nabla}_\perp a_{\lambda z}(z) - r_\lambda \left(\frac{z+s}{c} \right) \vec{\nabla}_\perp \phi_\lambda(z) \right) . \tag{A.48}
$$

Substituting q_λ, r_λ from Eqs. (A.32) and (A.33) will give the final result for $\vec{W}_\perp$. The problem is naturally solved in three pieces:

a) $s > L$: The test charge enters after the exciting charge has already left the cavity.

149

In this case

$$r_\lambda \left(\frac{z+s}{c}\right) = 0,$$

$$q_\lambda \left(\frac{z+s}{c}\right) = \frac{Q}{2U_\lambda \omega_\lambda} \int_0^L a_{\lambda z}(z') \sin \frac{\omega_\lambda (z+s-z')}{c} dz',$$

$$\vec{W}_\perp(s) = \sum_\lambda \frac{c}{2U_\lambda \omega_\lambda} \int_0^L \int_0^L \left(\vec{\nabla}_\perp a_{\lambda z}(z)\right) a_{\lambda z}(z') \sin \frac{\omega_\lambda (z+s-z')}{c} dz' dz$$

$$= \sum_\lambda \frac{c}{2U_\lambda \omega_\lambda} \vec{I}_{1\lambda}(s),$$

where

$$\vec{I}_{1\lambda}(s) = \int_0^L \int_0^L \left(\vec{\nabla}_\perp a_{\lambda z}(z)\right) a_{\lambda z}(z') \sin \frac{\omega_\lambda (z+s-z')}{c} dz' dz. \qquad (A.49)$$

Compare the last integral with

$$\mathrm{Im}\left\{ V_\lambda^* \left(\vec{\nabla}_\perp V_\lambda\right) \exp\left(i\omega_\lambda s/c\right)\right\}$$

$$= \int_0^L \int_0^L dz' dz \sin\left(\frac{\omega_\lambda (z-z'+s)}{c}\right) \left(\vec{\nabla}_\perp a_{\lambda z}(z)\right) a_{\lambda z}(z').$$

So we find the transverse wake potential for $s > L$:

$$\vec{W}_\perp(s) = \sum_\lambda \frac{c}{2U_\lambda \omega_\lambda} \mathrm{Im}\left\{ V_\lambda^* \left(\vec{\nabla}_\perp V_\lambda\right) \exp\left(i\omega_\lambda s/c\right)\right\}. \qquad (A.50)$$

b) $0 < s < L$: The test charge enters while the exciting charge is still in the

150

cavity. In this case

$$r_\lambda\left(\frac{z+s}{c}\right) = \frac{Q}{2T_\lambda}\phi_\lambda\left(z+s\right),$$

$$q_\lambda\left(\frac{z+s}{c}\right) = \frac{Q}{2U_\lambda\omega_\lambda}\int_0^{\min(z+s,L)} a_{\lambda z}\left(z'\right)\sin\frac{\omega_\lambda\left(z+s-z'\right)}{c}dz',$$

$$\vec{W}_\perp\left(s\right) = \sum_\lambda \frac{c}{2U_\lambda\omega_\lambda}\int_0^L dz \int_0^{\min(z+s,L)} dz \left(\vec{\nabla}_\perp a_{\lambda z}\left(z\right)\right) a_{\lambda z}\left(z'\right)\sin\frac{\omega_\lambda\left(z+s-z'\right)}{c}$$

$$-\sum_\lambda \int_0^L \frac{1}{2T_\lambda}\phi_\lambda\left(z+s\right)\left(\vec{\nabla}_\perp\phi_\lambda\left(z\right)\right)dz = \sum_\lambda\left(c\frac{\vec{I}'_{1\lambda}\left(s\right)-\vec{I}'_{2\lambda}\left(s\right)}{2U_\lambda\omega_\lambda} - \frac{\vec{K}'_{1\lambda}\left(s\right)}{2T_\lambda}\right),$$

$$\text{(A.51)}$$

where

$$
\begin{aligned}
\vec{I}'_{2\lambda}\left(s\right) &= \int_0^L dz \int_{\min(z+s,L)}^L dz' \left(\vec{\nabla}_\perp a_{\lambda z}\left(z\right)\right) a_{\lambda z}\left(z'\right)\sin\frac{\omega_\lambda\left(z+s-z'\right)}{c} \\
&= \int_0^{L-s} dz \int_{z+s}^L dz' \left(\vec{\nabla}_\perp a_{\lambda z}\left(z\right)\right) a_{\lambda z}\left(z'\right)\sin\frac{\omega_\lambda\left(z+s-z'\right)}{c}, \\
\vec{K}_{1\lambda}\left(s\right) &= \int_0^L \phi_\lambda\left(z+s\right)\left(\vec{\nabla}_\perp\phi_\lambda\left(z\right)\right)dz \\
&= \int_0^{L-s} \phi_\lambda\left(z+s\right)\left(\vec{\nabla}_\perp\phi_\lambda\left(z\right)\right)dz, \text{ since } \phi_\lambda\left(z+s\right) = 0 \text{ for } z > L-s.
\end{aligned}
$$

The causality requires, that the wake potential is zero for $s < 0$. In particular, in the range $-L < s < 0$ it yields

$$r_\lambda\left(\frac{z+s}{c}\right) = \frac{Q}{2T_\lambda}\phi_\lambda\left(z+s\right)\vartheta\left(z+s\right),$$

$$q_\lambda\left(\frac{z+s}{c}\right) = \frac{Q}{2U_\lambda\omega_\lambda}\int_0^{\max(0,z+s)} a_{\lambda z}\left(z'\right)\sin\frac{\omega_\lambda\left(z+s-z'\right)}{c}dz',$$

$$\vec{W}_\perp\left(s\right) = \sum_\lambda \frac{c}{2U_\lambda\omega_\lambda}\int_0^L dz \int_0^{\max(0,z+s)} dz' \left(\vec{\nabla}_\perp a_{\lambda z}\left(z\right)\right) a_{\lambda z}\left(z'\right)\sin\frac{\omega_\lambda\left(z+s-z'\right)}{c}$$

$$-\sum_\lambda \int_{-s}^L \frac{1}{2T_\lambda}\phi_\lambda\left(z+s\right)\left(\vec{\nabla}_\perp\phi_\lambda\left(z\right)\right)dz$$

$$= \sum_\lambda\left(c\frac{\vec{I}'_{3\lambda}\left(s\right)}{2U_\lambda\omega_\lambda} - \frac{\vec{K}'_{2\lambda}\left(s\right)}{2T_\lambda}\right) = 0, \qquad\text{(A.52)}$$

151

where

$$
\begin{aligned}
\vec{I}_{3\lambda}\left(s\right) & = \int_0^L dz \int_0^{\max(0,z+s)} dz' \left(\vec{\nabla}_\perp a_{\lambda z}\left(z\right)\right) a_{\lambda z}\left(z'\right) \sin \frac{\omega_\lambda\left(z + s - z'\right)}{c} \\
& = -\int_0^{L+s} dz \int_{z'-s}^L dz' \left(\vec{\nabla}_\perp a_{\lambda z}\left(z'\right)\right) a_{\lambda z}\left(z\right) \sin \frac{\omega_\lambda\left(z - s - z'\right)}{c}. \quad (A.53)
\end{aligned}
$$

and

$$
\begin{aligned}
\vec{K}_{2\lambda}'\left(s\right) & = \int_{-s}^L \phi_\lambda\left(z + s\right)\left(\vec{\nabla}_\perp \phi_\lambda\left(z\right)\right) dz \\
& = \int_0^{L+s} \phi_\lambda\left(z\right)\left(\vec{\nabla}_\perp \phi_\lambda\left(z - s\right)\right) dz. \quad (A.54)
\end{aligned}
$$

Unlike the longitudinal case, Eq. (A.51) cannot be in general simplified. But nevertheless the certain similarity between $\vec{I}_{3\lambda}'$ and $\vec{I}_{2\lambda}'$, and between $\vec{K}_{2\lambda}'$ and $\vec{K}_{1\lambda}'$ can be seen. For the special case of a right cylinder with arbitrary cross-section whose axis is aligned with the $z-$ axis $a_{\lambda z}$ and ϕ_λ can be written as

$$
\begin{aligned}
a_{\lambda z}\left(x, y, z\right) & = f_\lambda\left(x, y\right) g_\lambda\left(z\right), \\
\phi_\lambda\left(x, y, z\right) & = \varphi_\lambda\left(x, y\right) \varsigma_\lambda\left(z\right).
\end{aligned}
$$

In this case

$$
\begin{aligned}
\vec{I}_{3\lambda}\left(s\right) & = -\vec{I}_{2\lambda}\left(-s\right), \\
\vec{K}_{2\lambda}'\left(s\right) & = \vec{K}_{1\lambda}'\left(-s\right),
\end{aligned}
$$

and the relation (A.52) becomes

$$
\sum_\lambda \left(c \frac{\vec{I}_{2\lambda}'\left(s\right)}{2U_\lambda \omega_\lambda} + \frac{\vec{K}_{1\lambda}'\left(s\right)}{2T_\lambda} \right) = 0, \quad 0 < s < L. \quad (A.55)
$$

Plugging (A.55) to (A.51) we see, that for cavities with translational symmetry for

152

$0 < s < L$

$$\vec{W}_\perp(s) = \sum_\lambda \frac{c}{2U_\lambda \omega_\lambda} \operatorname{Im}\left\{V_\lambda^* \left(\vec{\nabla}_\perp V_\lambda\right) \exp\left(i\omega_\lambda s/c\right)\right\}$$

$$= \sum_\lambda \frac{c}{2U_\lambda \omega_\lambda} V_\lambda^* \left(\vec{\nabla}_\perp V_\lambda\right) \sin\left(\frac{\omega_\lambda s}{c}\right). \qquad (A.56)$$

c) $s < 0$. The test charge enters before the exciting charge. From causality

$$\vec{W}_\perp(s) = 0, \quad s < 0. \qquad (A.57)$$

The exciting charge itself feels no the transverse wake field. Since the transverse wake is a sum of sine terms it rises to a maximum value somewhere behind the exciting charge.

A.5 Generalization for the case of parallel paths of charges

An important generalization is to define the wake fields in terms of an exciting charge and a test charge that move on parallel paths, not merely on the identical path (figure 4-4). Take those paths to be parallel to the $\hat{z}$-axis. The source terms due to the exciting charge are

$$\rho(\vec{x},t) = Q\delta\left(\vec{r} - \vec{r}\prime\right)\delta\left(z - ct\right), \qquad (A.58)$$

$$\vec{j}(\vec{x},t) = \hat{z}c\rho\left(\vec{x},t\right),$$

where the cylindrical coordinate system is used with $\vec{x} = \vec{r} + \hat{z}_0 z$, $\vec{r}$ is the transverse coordinate, $\vec{r}\prime$ is the transverse coordinate of the exciting charge.

The wake fields are functions of the transverse coordinates of the exciting charge $\vec{r}\prime$ and the test charge $\vec{r}$ as well as of their longitudinal separation s. Consider a special case of cavity with translational symmetry.

A.5.1 Generalization for the longitudinal wake potential

All the equations (A.31)-(A.34) are generalized for the case of non-identical paths straight forward by substituting $a_{\lambda z}(0,0,ct)$ by $a_{\lambda z}(\vec{r},ct)$. V_λ will be now the function of $\vec{r}$ and is introduced as

$$V_\lambda(\vec{r}) = \int_0^L dz \exp(i\omega_\lambda z/c)\, a_{\lambda z}(\vec{r},ct), \tag{A.59}$$

and

$$\mathcal{E}(\vec{r}) = Q^2 \sum_\lambda \frac{|V_\lambda(\vec{r})|^2}{4U_\lambda}. \tag{A.60}$$

The wake potential is given by

$$W_z(\vec{r}',\vec{r},s) = \frac{1}{Q}\sum_\lambda \int_0^L \left(\dot{q}_\lambda^{r'}\left(\frac{z+s}{c}\right) a_{\lambda z}(\vec{r},z) + r_\lambda^{r'}\left(\frac{z+s}{c}\right) \frac{\partial}{\partial z}\phi_\lambda(\vec{r},z) \right), \tag{A.61}$$

where

$$q_\lambda^{r'}(t) = \frac{cQ}{2U_\lambda\omega_\lambda} \int_0^{\min(t,L/c)} a_{\lambda z}(\vec{r}',ct')\sin\omega_\lambda(t-t')\,dt'. \tag{A.62}$$

$$r_\lambda^{r'}(t) = \frac{Q}{2T_\lambda}\begin{cases} 0, & t < 0 \\ \phi_\lambda(\vec{r}',ct), & 0 < t < L/c \\ 0, & t > L/c \end{cases} \tag{A.63}$$

Consider different times when the test charge enters the cavity.

a) $s > L$: The test charge enters after the exciting charge has already left the cavity.

In this case

$$\begin{aligned} W_z(\vec{r}',\vec{r},s) &= \sum_\lambda \frac{1}{2U_\lambda} \int_0^L \int_0^L a_{\lambda z}(\vec{r},z)\, a_{\lambda z}(\vec{r}',z')\cos\frac{\omega_\lambda(z+s-z')}{c}\,dz'dz \\ &= \sum_\lambda \frac{1}{2U_\lambda} V_\lambda(\vec{r}) V_\lambda^*(\vec{r})\cos\left(\frac{\omega_\lambda s}{c}\right). \end{aligned}$$

b) $0 < s < L$: The test charge enters while the exciting charge is still in the

cavity. Here

$$W_z\left(\vec{r}',\vec{r},s\right) = \sum_\lambda \frac{1}{2U_\lambda} \int_0^L dz \int_0^{\min(z+s,L)} dz' a_{\lambda z}\left(\vec{r},z\right) a_{\lambda z}\left(\vec{r}',z'\right) \cos\frac{\omega_\lambda\left(z+s-z'\right)}{c}$$

$$+ \sum_\lambda \int_0^L \frac{1}{2T_\lambda}\phi_\lambda\left(\vec{r}',z+s\right)\frac{\partial}{\partial z}\phi_\lambda\left(\vec{r},z\right)dz$$

$$= \sum_\lambda \left(\frac{I_{1\lambda}\left(\vec{r}',\vec{r},s\right) - I_{2\lambda}\left(\vec{r}',\vec{r},s\right)}{2U_\lambda} + \frac{K_{1\lambda}\left(\vec{r}',\vec{r},s\right)}{2T_\lambda}\right), \qquad \text{(A.64)}$$

with

$$I_{1\lambda}\left(\vec{r}',\vec{r},s\right) = \int_0^L \int_0^L a_{\lambda z}\left(\vec{r},z\right) a_{\lambda z}\left(\vec{r}',z'\right) \cos\frac{\omega_\lambda\left(z+s-z'\right)}{c}dz'dz$$

$$= \text{Re}\left\{V_\lambda\left(\vec{r}\right) V_\lambda^*\left(\vec{r}'\right)\exp\left(i\omega_\lambda s/c\right)\right\},$$

$$I_{2\lambda}\left(\vec{r}',\vec{r},s\right) = \int_0^L dz \int_{\min(z+s,L)}^L dz' a_{\lambda z}\left(\vec{r},z\right) a_{\lambda z}\left(\vec{r}',z'\right) \cos\frac{\omega_\lambda\left(z+s-z'\right)}{c}$$

$$= \int_0^{L-s} dz \int_{z+s}^L dz' a_{\lambda z}\left(\vec{r},z\right) a_{\lambda z}\left(\vec{r}',z'\right) \cos\frac{\omega_\lambda\left(z+s-z'\right)}{c},$$

$$K_{1\lambda}\left(\vec{r}',\vec{r},s\right) = \int_0^L \phi_\lambda\left(\vec{r}',z+s\right)\frac{\partial}{\partial z}\phi_\lambda\left(\vec{r},z\right)dz$$

$$= \int_0^{L-s} \phi_\lambda\left(\vec{r}',z+s\right)\frac{\partial}{\partial z}\phi_\lambda\left(\vec{r},z\right)dz,$$

since $\phi_\lambda\left(\vec{r}',z+s\right) = 0$ for $z > L - s$.

The causality requires, that the wake potential is zero for $s < 0$. In particular, in the range $-L < s < 0$ it yields

$$W_z\left(\vec{r}',\vec{r},s\right) = \sum_\lambda \frac{1}{2U_\lambda} \int_0^L dz \int_0^{\max(0,z+s)} dz' a_{\lambda z}\left(\vec{r},z\right) a_{\lambda z}\left(\vec{r}',z'\right) \cos\frac{\omega_\lambda\left(z+s-z'\right)}{c}$$

$$+ \sum_\lambda \int_{-s}^L \frac{1}{2T_\lambda}\phi_\lambda\left(\vec{r}',z+s\right)\frac{\partial}{\partial z}\phi_\lambda\left(\vec{r},z\right)dz$$

$$= \sum_\lambda \left(\frac{I_{3\lambda}\left(\vec{r}',\vec{r},s\right)}{2U_\lambda} + \frac{K_{2\lambda}\left(\vec{r}',\vec{r},s\right)}{2T_\lambda}\right) = 0, \qquad \text{(A.65)}$$

where

$$I_{3\lambda}\left(\vec{r}',\vec{r},s\right) = \int_0^L dz \int_0^{\max(0,z+s)} dz'' a_{\lambda z}\left(\vec{r},z\right) a_{\lambda z}\left(\vec{r}',z'\right) \cos\frac{\omega_\lambda\left(z+s-z'\right)}{c}$$

$$= \int_0^{L+s} dz \int_{z-s}^L dz' a_{\lambda z}\left(\vec{r}',z\right) a_{\lambda z}\left(\vec{r},z'\right) \cos\frac{\omega_\lambda\left(z-s-z'\right)}{c}.$$

$$K_{2\lambda}\left(\vec{r}',\vec{r},s\right) = \int_{-s}^L \phi_\lambda\left(\vec{r}',z+s\right) \frac{\partial}{\partial z}\phi_\lambda\left(\vec{r},z\right) dz.$$

Integrate by parts

$$K_{2\lambda}\left(\vec{r}',\vec{r},s\right) = -\int_{-s}^L \frac{\partial}{\partial z}\phi_\lambda\left(\vec{r}',z+s\right) \phi_\lambda\left(\vec{r},z\right) dz$$

$$= -\int_0^{L+s} \phi_\lambda\left(\vec{r},z-s\right) \frac{\partial}{\partial z}\phi_\lambda\left(\vec{r}',z\right) dz.$$

Unlike the case of the same paths, Eq. (A.64) cannot be in general simplified. But nevertheless the certain similarity between $\vec{I}_{3\lambda}$ and $\vec{I}_{2\lambda}$, and between $\vec{K}_{2\lambda}$ and $\vec{K}_{1\lambda}$ can be seen. For the special case of a right cylinder with arbitrary cross-section whose axis is aligned with the $z-$ axis $a_{\lambda z}$ and ϕ_λ can be written as

$$a_{\lambda z}\left(\vec{r},z\right) = f_\lambda\left(\vec{r}\right) g_\lambda\left(z\right),$$

$$\phi_\lambda\left(\vec{r},z\right) = \varphi_\lambda\left(\vec{r}\right) \varsigma_\lambda\left(z\right).$$

In this case

$$\vec{I}_{3\lambda}\left(\vec{r}',\vec{r},s\right) = \vec{I}_{2\lambda}\left(\vec{r}',\vec{r},-s\right),$$

$$\vec{K}_{2\lambda}\left(\vec{r}',\vec{r},s\right) = -\vec{K}_{1\lambda}\left(\vec{r}',\vec{r},-s\right),$$

and the relation (A.65) becomes

$$\sum_\lambda \left(c\frac{\vec{I}_{2\lambda}\left(\vec{r}',\vec{r},s\right)}{2U_\lambda\omega_\lambda} - \frac{\vec{K}_{1\lambda}\left(\vec{r}',\vec{r},s\right)}{2T_\lambda}\right) = 0, \quad 0 < s < L. \tag{A.66}$$

So we find the wake potential

$$
\begin{aligned}
W_z\left(\vec{r}', \vec{r}, s\right) &= \sum_\lambda \frac{I_{1\lambda}\left(\vec{r}', \vec{r}, s\right)}{2U_\lambda} \\
&= \sum_\lambda \frac{1}{2U_\lambda} V_\lambda\left(\vec{r}\right) V_\lambda^*\left(\vec{r}'\right) \cos\left(\frac{\omega_\lambda s}{c}\right).
\end{aligned}
\tag{A.67}
$$

As in the case of the same paths, the longitudinal wake potential for $0 < z < L$ has the same form as the longitudinal wake potential for $z > L$.

c) $s < 0$. The test charge enters before the exciting charge. From causality

$$
W_z\left(\vec{r}', \vec{r}, s\right) = 0, \quad s < 0.
\tag{A.68}
$$

A.5.2 Generalization for the transverse wake potential

The Eq.(A.48) for the transverse wake potential is generalized for the case of non-identical paths as

$$
\begin{aligned}
\vec{W}_\perp\left(\vec{r}', \vec{r}, s\right) &= \frac{1}{Q} \sum_\lambda \int_0^L dz \left(c q_\lambda^{r'}\left(\frac{z+s}{c}\right) \vec{\nabla}_\perp a_{\lambda z}\left(\vec{r}, z\right) \right. \\
&\left. \quad - r_\lambda^{r'}\left(\frac{z+s}{c}\right) \vec{\nabla}_\perp \phi_\lambda\left(\vec{r}, z\right) \right),
\end{aligned}
\tag{A.69}
$$

where $q_\lambda^{r'}$ and $r_\lambda^{r'}$ are given by (A.62) and (A.63). As we did above consider three different cases:

a) $s > L$: The test charge enters after the exciting charge has already left the cavity.

In this case

$$
\begin{aligned}
\vec{W}_\perp\left(\vec{r}', \vec{r}, s\right) &= \sum_\lambda \frac{c}{2U_\lambda \omega_\lambda} \int_0^L \int_0^L \left(\vec{\nabla}_\perp a_{\lambda z}\left(\vec{r}, z\right)\right) a_{\lambda z}\left(\vec{r}', z'\right) \sin\frac{\omega_\lambda\left(z+s-z'\right)}{c} dz' dz \\
&= \sum_\lambda \frac{c}{2U_\lambda \omega_\lambda} V_\lambda^*\left(\vec{r}', z'\right) \left(\vec{\nabla}_\perp V_\lambda\left(\vec{r}, z\right)\right) \sin\left(\frac{\omega_\lambda s}{c}\right).
\end{aligned}
$$

The last equality is true only for the case of the cavity with translational symmetry.

b) $0 < s < L$: The test charge enters while the exciting charge is still in the cavity. In this case

$$\vec{W}_\perp\left(\vec{r'},\vec{r},s\right) = \sum_\lambda \frac{c}{2U_\lambda\omega_\lambda} \int_0^L dz \int_0^{\min(z+s,L)} dz$$

$$\left(\vec{\nabla}_\perp a_{\lambda z}\left(\vec{r},z\right)\right) a_{\lambda z}\left(\vec{r'},z'\right) \sin\frac{\omega_\lambda\left(z+s-z'\right)}{c}$$

$$-\sum_\lambda \int_0^L \frac{1}{2T_\lambda}\phi_\lambda\left(\vec{r'},z+s\right)\left(\vec{\nabla}_\perp\phi_\lambda\left(\vec{r},z\right)\right) dz$$

$$= \sum_\lambda \left(c\frac{\vec{I}_{1\lambda}'\left(\vec{r'},\vec{r},s\right) - \vec{I}_{2\lambda}'\left(\vec{r'},\vec{r},s\right)}{2U_\lambda\omega_\lambda} - \frac{\vec{K}_{1\lambda}'\left(\vec{r'},\vec{r},s\right)}{2T_\lambda}\right), \quad (A.70)$$

where

$$\vec{I}_{2\lambda}'\left(\vec{r'},\vec{r},s\right) = \int_0^L dz \int_{\min(z+s,L)}^L dz' \left(\vec{\nabla}_\perp a_{\lambda z}\left(\vec{r},z\right)\right) a_{\lambda z}\left(\vec{r'},z'\right) \sin\frac{\omega_\lambda\left(z+s-z'\right)}{c}$$

$$= \int_0^{L-s} dz \int_{z+s}^L dz' \left(\vec{\nabla}_\perp a_{\lambda z}\left(\vec{r},z\right)\right) a_{\lambda z}\left(\vec{r'},z'\right) \sin\frac{\omega_\lambda\left(z+s-z'\right)}{c},$$

$$\vec{K}_{1\lambda}'\left(\vec{r'},\vec{r},s\right) = \int_0^L \phi_\lambda\left(\vec{r'},z+s\right)\left(\vec{\nabla}_\perp\phi_\lambda\left(\vec{r},z\right)\right) dz$$

$$= \int_0^{L-s} \phi_\lambda\left(\vec{r'},z+s\right)\left(\vec{\nabla}_\perp\phi_\lambda\left(\vec{r},z\right)\right) dz,$$

since $\phi_\lambda\left(\vec{r'},z+s\right) = 0$ for $z > L - s$.

The causality requires, that the wake potential is zero for $s < 0$. In particular, in the range $-L < s < 0$ it yields

$$\vec{W}_\perp\left(\vec{r'},\vec{r},s\right) = \sum_\lambda \frac{c}{2U_\lambda\omega_\lambda}$$

$$\int_0^L dz \int_0^{\max(0,z+s)} dz' \left(\vec{\nabla}_\perp a_{\lambda z}\left(\vec{r},z\right)\right) a_{\lambda z}\left(\vec{r'},z'\right) \sin\frac{\omega_\lambda\left(z+s-z'\right)}{c}$$

$$-\sum_\lambda \int_{-s}^L \frac{1}{2T_\lambda}\phi_\lambda\left(\vec{r'},z+s\right)\left(\vec{\nabla}_\perp\phi_\lambda\left(\vec{r},z\right)\right) dz$$

$$= \sum_\lambda \left(c\frac{\vec{I}_{3\lambda}'\left(\vec{r'},\vec{r},s\right)}{2U_\lambda\omega_\lambda} - \frac{\vec{K}_{2\lambda}'\left(\vec{r'},\vec{r},s\right)}{2T_\lambda}\right) = 0, \quad (A.71)$$

where

$$
\begin{aligned}
\vec{I}_{3\lambda}\left(\vec{r}',\vec{r},s\right) &= \int_0^L dz \int_0^{\max(0,z+s)} dz'\left(\vec{\nabla}_\perp a_{\lambda z}\left(\vec{r},z\right)\right) a_{\lambda z}\left(\vec{r}',z'\right)\sin\frac{\omega_\lambda\left(z+s-z'\right)}{c} \\
&= -\int_0^{L+s} dz \int_{z'-s}^L dz'\left(\vec{\nabla}_\perp a_{\lambda z}\left(\vec{r},z'\right)\right) a_{\lambda z}\left(\vec{r}',z\right)\sin\frac{\omega_\lambda\left(z-s-z'\right)}{c}.
\end{aligned}
$$

and

$$
\begin{aligned}
\vec{K}'_{2\lambda}\left(\vec{r}',\vec{r},s\right) &= \phi_\lambda\left(\vec{r}',z+s\right)\left(\vec{\nabla}_\perp\phi_\lambda\left(\vec{r},z\right)\right) dz \\
&= \int_0^{L+s}\phi_\lambda\left(\vec{r}',z\right)\left(\vec{\nabla}_\perp\phi_\lambda\left(\vec{r},z-s\right)\right) dz.
\end{aligned} \tag{A.72}
$$

The Eq. (A.70) can be simplified for the special case of a right cylinder with arbitrary cross-section whose axis is aligned with the $z-$axis, when $a_{\lambda z}$ and ϕ_λ can be written as

$$
a_{\lambda z}\left(\vec{r},z\right) = f_\lambda\left(\vec{r}\right) g_\lambda\left(z\right), \tag{A.73}
$$

$$
\phi_\lambda\left(\vec{r},z\right) = \varphi_\lambda\left(\vec{r}\right)\varsigma_\lambda\left(z\right). \tag{A.74}
$$

In this case

$$
\begin{aligned}
\vec{I}_{3\lambda}\left(\vec{r}',\vec{r},s\right) &= -\vec{I}_{2\lambda}\left(\vec{r}',\vec{r},-s\right), \\
\vec{K}'_{2\lambda}\left(\vec{r}',\vec{r},s\right) &= \vec{K}'_{1\lambda}\left(\vec{r}',\vec{r},-s\right),
\end{aligned}
$$

and the relation (A.71) becomes

$$
\sum_\lambda\left(c\frac{\vec{I}'_{2\lambda}\left(\vec{r}',\vec{r},s\right)}{2U_\lambda\omega_\lambda}+\frac{\vec{K}'_{1\lambda}\left(\vec{r}',\vec{r},s\right)}{2T_\lambda}\right) = 0, \quad 0 < s < L. \tag{A.75}
$$

Then Eq. (A.70) becomes

$$
\begin{aligned}
\vec{W}_\perp\left(\vec{r}',\vec{r},s\right) &= \sum_\lambda \frac{c}{2U_\lambda\omega_\lambda} \operatorname{Im}\left\{ V_\lambda^*\left(\vec{r}',z'\right)\left(\vec{\nabla}_\perp V_\lambda\left(\vec{r},z\right)\right)\exp\left(i\omega_\lambda s/c\right)\right\} \\
&= \sum_\lambda \frac{c}{2U_\lambda\omega_\lambda} V_\lambda^*\left(\vec{r}',z'\right)\left(\vec{\nabla}_\perp V_\lambda\left(\vec{r},z\right)\right)\sin\left(\frac{\omega_\lambda s}{c}\right). \qquad (\text{A.76})
\end{aligned}
$$

c) $s < 0$. The test charge enters before the exciting charge. From causality

$$
\vec{W}_\perp\left(\vec{r}',\vec{r},s\right) = 0, \quad s < 0. \tag{A.77}
$$

The exciting charge itself feels no the transverse wake field. Since the transverse wake is a sum of sine terms it rises to a maximum value somewhere behind the exciting charge.

A.5.3   Panofsky-Wenzel theorem

Let us summarize the results, which we obtained. We considered the wake potentials for the case when the exciting charge and the test charge move along the parallel paths. We found, that for the case of the cavities with translational symmetry, that

$$
W_z\left(\vec{r}',\vec{r},s\right) = \sum_\lambda \frac{1}{2U_\lambda} V_\lambda\left(\vec{r}\right) V_\lambda^*\left(\vec{r}'\right)\cos\left(\frac{\omega_\lambda s}{c}\right), \tag{A.78}
$$

$$
\vec{W}_\perp\left(\vec{r}',\vec{r},s\right) = \sum_\lambda \frac{c}{2U_\lambda\omega_\lambda} V_\lambda^*\left(\vec{r}',z'\right)\left(\vec{\nabla}_\perp V_\lambda\left(\vec{r},z\right)\right)\sin\left(\frac{\omega_\lambda s}{c}\right). \tag{A.79}
$$

The Panofsky-Wenzel theorem can be proved simply by comparison of the above expressions. It claims that

$$
\frac{\partial\vec{W}_\perp}{\partial s} = \vec{\nabla}_\perp W_z. \tag{A.80}
$$

Appendix B

Equivalent circuit for a disk-loaded waveguide

B.1 Introduction

It was explained in Chapter 5 that matching the TW coupler is different from matching a coupler of a resonator. The easiest way to explain the matching algorithms for the TW coupler is the equivalent circuit language. There will be no reflection from the TW disk-loaded waveguide at certain frequency ω_0 if the admittance of the coupler section is equal to the admittance of the infinite TW section at ω_0:

$$Y_{in} = Y_\infty \left(\omega_0 \right). \tag{B.1}$$

In this appendix the equivalent circuit for an infinite disk-loaded waveguide will be derived.

B.2 Two-port network and its parameters

A general circuit for a two-port network is shown in figure B-1. The input voltage and current V_1, I_1 are related to the output voltage and current V_2, I_2 by the Kirchhoff
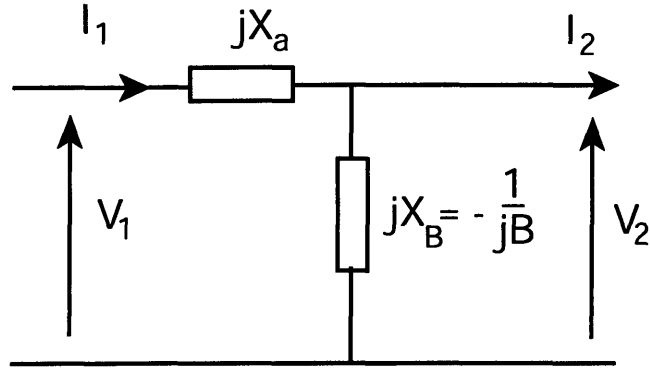
Figure B-1: Lossless two port network circuit.

laws:

$$\begin{cases} V_2 - V_1 = -jX_a I_1 \\ I_2 - I_1 = -\frac{V_2}{jX_b} = jBV_2 \end{cases} \tag{B.2}$$

B.3 Equivalent circuit for the TM mode in a unit length waveguide

A unit length waveguide can be fully represented by a lossless two-port network. This section deals with the calculation of the network parameters. The derivations follow [47]. A waveguide section schematic is shown in figure B-2. Start with Maxwell's equations in vacuum:

$$\begin{cases} \vec{\nabla} \times \vec{E} = -j\omega\mu_0\vec{H} \\ \vec{\nabla} \times \vec{H} = j\omega\varepsilon_0\vec{E} \\ \vec{\nabla} \cdot \vec{E} = 0 \\ \vec{\nabla} \cdot \vec{H} = 0 \end{cases} \tag{B.3}$$

Introduce the potentials $\vec{H} = \vec{\nabla} \times \vec{A}$, $\vec{E} = -\vec{\nabla}\varphi - \mu_0\frac{\partial \vec{A}}{\partial t}$. Use Lorenz calibration $\vec{\nabla} \cdot \vec{A} + \varepsilon_0\frac{\partial \varphi}{\partial t} = 0$. Lorenz calibration is automatically satisfied if the vector-potential $\vec{\Pi}$ is introduced so that $\varphi = -\frac{1}{j\omega\varepsilon_0}\vec{\nabla} \cdot \vec{\Pi}$, $\vec{A} = \frac{1}{j\omega}\frac{\partial \vec{\Pi}}{\partial t} = \vec{\Pi}$. Then
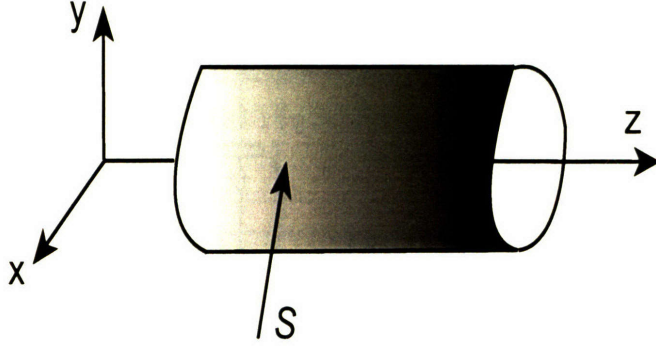
162

Figure B-2: The schematic of a waveguide section.

$$\vec{E} = \frac{1}{j\omega\varepsilon_0}\left(\vec{\nabla}\left(\vec{\nabla}\cdot\vec{\Pi}\right) + k_0^2\vec{\Pi}\right),$$
$$\vec{H} = \vec{\nabla}\times\vec{\Pi}, \qquad\qquad\qquad (B.4)$$
$$\nabla^2\vec{\Pi} + k_0^2\vec{\Pi} = 0,$$

where $k_0 = \frac{\omega}{c} = \omega\sqrt{\mu_0\varepsilon_0}$.

For the TM mode $\vec{\Pi} = \Pi\hat{z}_0$, $\Pi = \Psi\left(x,y\right)Z\left(z\right)$, $\left.\Pi\right|_S = 0$, where S is the waveguide surface and z is the coordinate along the waveguide (figure B-2). This yields:

$$\begin{cases} \vec{\nabla}_\perp^2\Psi + \kappa^2\Psi = 0 \\ Z'' + k_z^2 Z = 0 \end{cases},$$
$$\kappa_{01}^2 + k_z^2 = k_0^2$$
$$\left.\Psi\right|_S = 0.$$

The fields now express as

$$\vec{H} = -\left(\hat{z}_0\times\vec{\nabla}_\perp\Psi\right)Z,$$
$$\vec{E} = \frac{1}{j\omega\varepsilon_0}\vec{\nabla}_\perp\Psi Z' + \frac{\kappa_{01}^2}{j\omega\varepsilon_0}\Psi Z\hat{z}_0. \qquad (B.5)$$

Introduce "mode functions" $\vec{e}\left(x,y\right)$ and $\vec{h}\left(x,y\right)$ and "mode voltages" and "mode

currents" $V(z)$ and $I(z)$:

$$\begin{cases} \vec{E}_\perp = \vec{e}(x,y)\, V(z) \\ \vec{H}_\perp = \vec{h}(x,y)\, I(z) \end{cases}, \qquad (B.6)$$

$$\begin{cases} \vec{e}(x,y) = -\vec{\nabla}_\perp \Psi \\ \vec{h}(x,y) = -\left(\hat{z}_0 \times \vec{\nabla}_\perp \Psi\right) \end{cases}, \quad \begin{cases} V(z) = -\frac{1}{j\omega\varepsilon_0}Z'(z) \\ I(z) = Z(z) \end{cases}. \qquad (B.7)$$

Normalize Ψ so that $\int \left|\vec{\nabla}_\perp \Psi(x,y)\right|^2 dxdy = 1$. Then $\int |\vec{e}|^2 dxdy = \int \left|\vec{h}\right|^2 dxdy = 1$.
The general solution for $V(z)$ and $I(z)$ is

$$\begin{cases} V(z) = V^+ e^{-\gamma z} + V^- e^{\gamma z} \\ I(z) = I^+ e^{-\gamma z} + I^- e^{\gamma z} \end{cases}, \qquad (B.8)$$

$$\text{with } \gamma = jk_0\sqrt{1 - \omega_c^2/\omega^2}, \quad \omega_c = \kappa c.$$

It follows from the definition of V and I that

$$\frac{V^+}{I^+} = Z_0, \quad \frac{V^-}{I^-} = -Z_0, \qquad (B.9)$$

where Z_0 is the characteristic line impedance

$$Z_0 = 1/Y_0 = \frac{1}{c\varepsilon_0}\sqrt{1 - \omega_c^2/\omega^2}. \qquad (B.10)$$

Differentiating B.8 we obtain that $V(z)$ and $I(z)$ satisfy the transmission line equations:

$$\begin{cases} \frac{dV}{dz} = -\gamma Z_0 I \\ \frac{dI}{dz} = -\gamma Y_0 V \end{cases}. \qquad (B.11)$$

For a waveguide section of length L such that $\gamma L \ll 1$, the transmission line equations B.11 become

$$\begin{cases} V(z+L) - V(z) = -\gamma Z_0 L I \\ I(z+L) - I(z) = -\gamma Y_0 L V \end{cases}. \qquad (B.12)$$

Comparing the equations B.12 to the two-port network Kirchhoff equations B.2 we
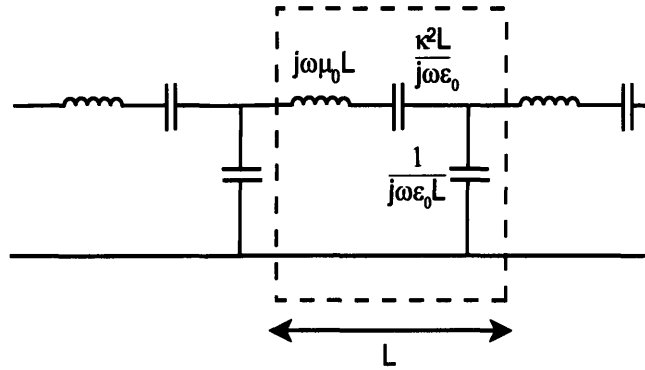
164

Figure B-3: Equivalent circuit for the TM_{01} mode in a lossless waveguide.

find that a waveguide section of length L can be represented by an equivalent circuit of figure B-1 with

$$\begin{cases} jX_a = j\omega\mu_0 L + \frac{\kappa_{01}^2 L}{j\omega\varepsilon_0} \\ jX_B = \frac{1}{j\omega\varepsilon_0 L} \end{cases} \quad . \tag{B.13}$$

Summarizing, the equivalent circuit for the TM mode in a waveguide is shown in figure B-3.

B.4 Equivalent circuit for the iris in a cylindrical waveguide with the TM_{01} mode

Now I will derive the equivalent circuit for an iris located in a cylindrical waveguide. I will follow the derivation of [48]. The following assumption are made:

- the iris is considered infinitely thin and located at $z = 0$ (figure B-4);

- the waveguide is considered single-moded at the given frequency, other modes only exist at the iris neighborhood.

Away from the iris the expressions B.6 for the fields are valid. In the absence of the iris $V(z)$ and $I(z)$ could be represented as a sum of symmetrical and antisymmetrical
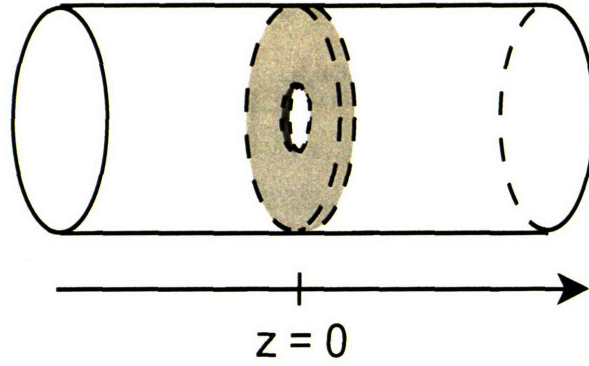
Figure B-4: Infinitely thin iris located in a cylindrical waveguide.

standing waves

$$\begin{cases} V\left(z\right) = C_1^0 \cos k_z z + C_2^0 \sin k_z z \\ I\left(z\right) = -\frac{jC_1^0}{Z_0} \sin k_z z + \frac{jC_2^0}{Z_0} \cos k_z z \end{cases} \quad . \tag{B.14}$$

The antisymmetrical part of B.14 with $V\left(z\right) = \sin k_z z$ and $I\left(z\right) = -\frac{j}{Z_0} \sin k_z z$ still satisfies the boundary condition when an infinitely thin iris is present. However the symmetric part of the solution does not satisfy the boundary conditions at $z = 0$ in the presence of iris. Iris may introduce some phase shift into the symmetrical solution. Thus in the presence of the iris the symmetrical part of the solution can be written as

$$\begin{cases} V\left(z\right) = \cos k_z \left(|z| - z_0\right) \\ I\left(z\right) = -\frac{j}{Z_0} \sin k_z \left(|z| - z_0\right) \end{cases} \quad . \tag{B.15}$$

The general solution in the presence of the iris valid for $|z| \gtrsim \pi/k_z$ is therefore

$$\begin{cases} V\left(z\right) = C_1 \cos k_z \left(|z| - z_0\right) + C_2 \sin k_z z \\ I\left(z\right) = -\frac{jC_1}{Z_0} \sin k_z \left(|z| - z_0\right) + \frac{jC_2}{Z_0} \cos k_z z \end{cases} \quad . \tag{B.16}$$
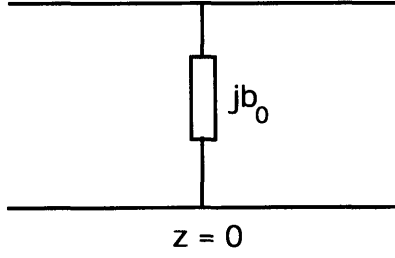
166

$$z = 0$$

Figure B-5: The equivalent circuit for an infinitely thin iris.

Consider now two reference planes: $z_1 = \pi/k_z$ and $z_2 = -\pi/k_z$. We have

$$\begin{cases} V(z_1) = -C_1 \cos k_z z_0 \\ I(z_1) = -\frac{jC_1}{Z_0} \sin k_z z_0 - \frac{jC_2}{Z_0} \end{cases}, \qquad (B.17)$$

$$\begin{cases} V(z_1) = -C_1 \cos k_z z_0 \\ I(z_1) = \frac{jC_1}{Z_0} \sin k_z z_0 - \frac{jC_2}{Z_0} \end{cases}. \qquad (B.18)$$

The characteristic admittances

$$\begin{cases} Y_1 = \frac{Z_0 I(z_1)}{V(z_1)} = j\frac{C_1 \sin k_z z_0 + C2}{C_1 \cos k_z z_0} \\ Y_2 = \frac{Z_0 I(z_2)}{V(z_2)} = j\frac{-C_1 \sin k_z z_0 + C2}{C_1 \cos k_z z_0} \end{cases}, \qquad (B.19)$$

$$Y_1 - Y_2 = 2j \tan k_z z_0 = -jb_0,$$

where b_0 is the iris susceptance. The equivalent circuit for the iris is shown in figure B-5. Now we need to find the magnitude of the iris shunt susceptance and determine the type of iris behavior: if it is capacitive or inductive.

The symmetric part of the electric field for the solution with iris can be expressed as series over all the eigenmodes in the waveguide $\left(\vec{E}_{\perp n}, , E_{zn}\right)$. Normalize the electric field of the eigenmodes so that

$$\begin{cases} \int\limits_{iris} \left|\vec{E}_{\perp n}\right|^2 dxdy = 1 \\ \int\limits_{iris} \left|\vec{E}_{zn}\right|^2 dxdy = \frac{\kappa_n^2}{k_z^2} \end{cases}. \qquad (B.20)$$

167

Then the field expansion will take form

$$
\begin{cases}
\vec{E}_{\perp s} = \sum_n \vec{E}_{\perp n} \int\limits_{iris} \vec{E}_{\perp s} \cdot \vec{E}_{\perp n}^* dxdy \\
E_{zs} = \sum_n \frac{k_z^2}{\kappa_n^2} E_{zn} \int\limits_{iris} E_{zs} E_{zn}^* dxdy
\end{cases}
\qquad (B.21)
$$

For $z = \pi/k_z$ all non-propagating modes will decay. Then

$$
\begin{cases}
\vec{E}_{\perp s}\left(z = \frac{\pi}{k_z}\right) = -\vec{e}_\perp(x,y) C_1 \cos k_z z_0 = -2\vec{e}(x,y) \int\limits_{iris} \vec{E}_{\perp s} \cdot \vec{E}_{\perp 1}^* dxdy, \\
E_z\left(z = \frac{\pi}{k_z}\right) = e_z(x,y) C_1 \sin k_z z_0 = 2je_z(x,y) \frac{k_z^2}{\kappa_{01}^2} \int\limits_{iris} E_{zs} E_{z1}^* dxdy.
\end{cases}
$$

Then

$$
b_0 = -2 \tan k_z z_0 = -2j \frac{k_z^2}{\kappa_{01}^2} \frac{\int\limits_{iris} E_{zs} E_{z1}^* dxdy}{\int\limits_{iris} \vec{E}_{\perp s} \cdot \vec{E}_{\perp 1}^* dxdy}.
$$

For the small iris opening the fields on the iris E_{zs} and $\vec{E}_{\perp s}$ can be calculated approximately in quasistatic approximation and the following expression for b_0 will be finally obtained [48]

$$
b_0 = \frac{3}{2a^3} \frac{k_z}{\kappa_{01}^2} \frac{\int\limits_{iris} E_{zs}^2 dxdy}{E_{zs}^2(0)},
$$

where a is the hole's radius. The susceptance is positive and proportional to the frequency and hence represents a capacitance.

The result of the capacitive susceptance has a straightforward physical explanation. In the TM_{01} mode the magnetic field lines travel in concentric circles and electric field lines have both, radial and longitudinal, components, but no tangential components. The current then flows normal to the iris edge (radially). This results in a concentration of charge near the edge where many electric lines end. Therefore, the capacitive behavior of the iris is expected.
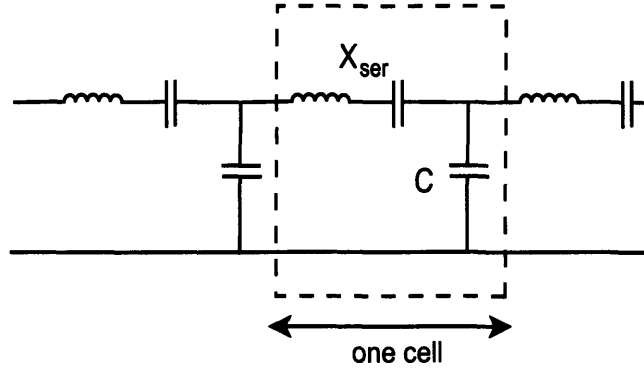
168

Figure B-6: The equivalent circuit for a microwave linear accelerator

B.5 Equivalent circuit for an accelerator and simple consequences

Combining the results of previous sections we find that a periodic structure of a microwave linear accelerator has the equivalent circuit of a bandpass filter shown in figure B-6. In figure B-6 X_{ser} stands for the total reactance of the series arm, C stands for the total capacitance.

$$\begin{cases} jX_{ser} = j\omega L_{ser} + \frac{1}{j\omega C_{ser}} = j\omega\mu_0 L_{cell} + \frac{\kappa_{01}^2 L_{cell}}{j\omega\varepsilon_0} \\ j\omega C = j\omega\varepsilon_0 L_{cell} + jb_0 \end{cases} \qquad (B.22)$$

The lowest frequency of the passband (0-mode) determines from the relationship

$$jX_{ser}(\omega_0) = j\omega_0 L_{ser} + \frac{1}{j\omega_0 C_{ser}} = 0,$$

$$\omega_0 = \frac{1}{\sqrt{L_{ser}C_{ser}}}. \qquad (B.23)$$

The width of the passband is usually small compared to the passband frequency $\Delta\omega \ll \omega_0$, therefore X_{ser} is linear over the passband [49].

$$X_{ser} = \omega L_{ser}\left(1 - \frac{\omega_0^2}{\omega^2}\right) \approx 2L_{ser}(\omega - \omega_0) = 4\pi L_{ser}(f - f_0).$$

169

C is almost constant over the passband and can be evaluated at $\pi/2$—mode for definiteness.

B.5.1 Dispersion relationship for the accelerator network

For a periodic network the solution must satisfy the Bloch theorem: $V_{n+1} = V_n e^{j\phi}$, $I_{n+1} = I_n e^{j\phi}$, where $\phi = k_z L_{cell}$ is the phase shift per cell. From B.2 we then obtain

$$\begin{cases} V_n \left(e^{j\phi} - 1\right) = -jX_{ser}I_n \\ I_n \left(e^{j\phi} - 1\right) = -j\omega C e^{j\phi}V_n \end{cases}. \tag{B.24}$$

The system of equations B.24 has a non-zero solution if the dispersion relationship is satisfied [50]:

$$\omega = \omega_0 \sqrt{\frac{2C_{ser}}{C}(1 - \cos\phi) + 1}. \tag{B.25}$$

For a narrow passband $\Delta\omega \ll \omega_0$ or $\frac{2C_{ser}}{C} \ll 1$ the dispersion relationship simplifies

$$\begin{aligned} \omega(\phi) &= \omega_0 \left(1 + \frac{C_{ser}}{C}(1 - \cos\phi)\right), \\ f(k_z L_{cell}) &= f\left(\frac{\pi}{2}\right) - \left(f\left(\frac{\pi}{2}\right) - f(0)\right)\cos k_z L_{cell}. \end{aligned} \tag{B.26}$$

B.5.2 Characteristic admittance of an infinite accelerator network

Introduce $jY_{ser} = 1/jX_{ser}$, $Y_c = \omega_{\pi/2}C$. The characteristic admittance of an infinite periodic network

$$\begin{aligned} jY_\infty &= \frac{\left(jY_\infty + j\frac{jY_c}{2}\right)jY_{ser}}{jY_\infty + j\frac{jY_c}{2} + jjY_{ser}} + j\frac{jY_c}{2}, \\ Y_\infty^2 &= Y_c Y_{ser}\left(1 + \frac{Y_c}{4Y_{ser}}\right). \end{aligned} \tag{B.27}$$

Let us calculate $Y_\infty \left(f_{\pi/2}\right)$, $Y_\infty \left(f_{2\pi/3}\right)$ and $Y_\infty \left(f_{ave}\right)$, where $f_{ave} = \left(f_{\pi/2} + f_{2\pi/3}\right)/2$. X_{ser} is linear with frequency. At $\pi-$ mode

$$jX_{ser}\left(\pi\right) + 2\frac{2}{jY_c} = 0, \quad X_{ser}\left(\pi\right) = \frac{4}{Y_c}.$$

Then

$$X_{ser}\left(\frac{\pi}{2}\right) = \frac{X_{ser}\left(\pi\right)}{2} = \frac{2}{Y_c},$$

$$f_{2\pi/3} = f_0 + \frac{3}{4}\left(f_\pi - f_0\right), \quad X_{ser}\left(\frac{2\pi}{3}\right) = \frac{3}{4}X_{ser}\left(\pi\right) = \frac{3}{Y_c},$$

$$X_{ser}\left(f_{ave}\right) = \frac{1}{2}\left(\frac{3}{Y_c} + \frac{2}{Y_c}\right) = \frac{5}{2Y_c}.$$

As a result,

$$
\begin{aligned}
jY_\infty\left(\frac{\pi}{2}\right) &= \frac{Y_c}{2}, \\
jY_\infty\left(\frac{2\pi}{3}\right) &= \frac{Y_c}{2\sqrt{3}}, \\
jY_\infty\left(f_{ave}\right) &= \sqrt{\frac{3}{5}}\frac{Y_c}{2}.
\end{aligned}
\tag{B.28}
$$

Appendix C

Ng and Ko method for an accelerator coupler design

The first computer simulation of coupling into a $2\pi/3$ mode of a travelling wave structure was performed by C.K. Ng and K. Ko [31]. I repeated their simulation for an example of a disk-loaded waveguide accelerator. The simulated structure is shown in figure C-1. The structure consists of two travelling-wave $2\pi/3$ cells and two coupling cells. The dimensions of TW cells were adjusted so that it has the frequency of 17.137 GHz (see table C.1). The microwaves at 17.137 GHz were feeded through one waveguide and the load was placed on the other waveguide. The iris opening of the coupling cell and the coupling cell diameter were varied until the VSWR close to 1 was obtained. The VSWR of 1.06 ($S_{11} = 2\%$) was achieved for the input cell dimensions shown in table C.1. For the coupling cell dimensions of table C.1 the flat field profile on the axis of the structure was obtained (figure C-1). The phase shift per travelling wave cell was close to 120^0.

Next, the tolerances were studied. First, the coupling cell radius was increased to $b = 6.76$ mm. Immediately the calculated VSWR increased to VSWR= 3. The field profile and the phase shift per TW cell also changes significantly (figure C-3(a)). However introducing significant ohmic losses in form of low wall conductivity $\sigma = 2 \cdot 10^7 \, (\Omega \cdot m)^{-1}$ did not produce a significant mismatch and disturb the field profile (figure C-3(b)). Finally, the dependence of the VSWR on the frequency was
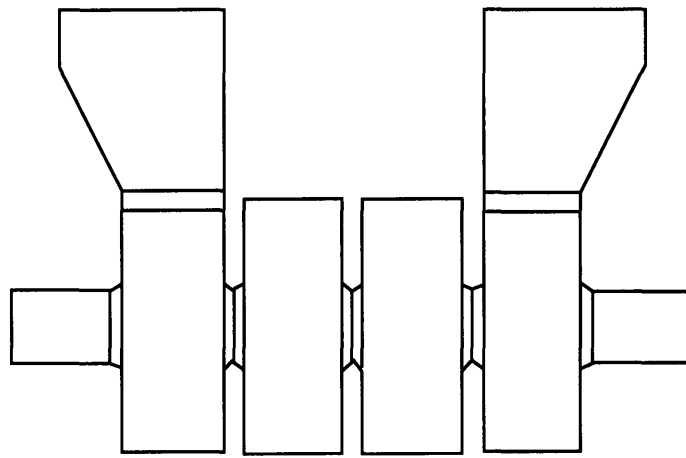
172

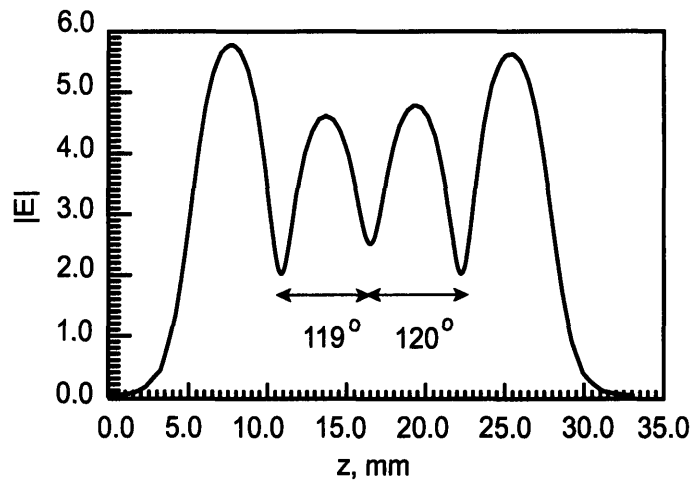Figure C-1: The geometry for the coupler simulation with Ng and Ko method.

Figure C-2: The on-axis electric field profile for the structure tuned to $VSWR = 1.06$ by Ng and Ko method. The phase shift per TW cell is shown with numbers.
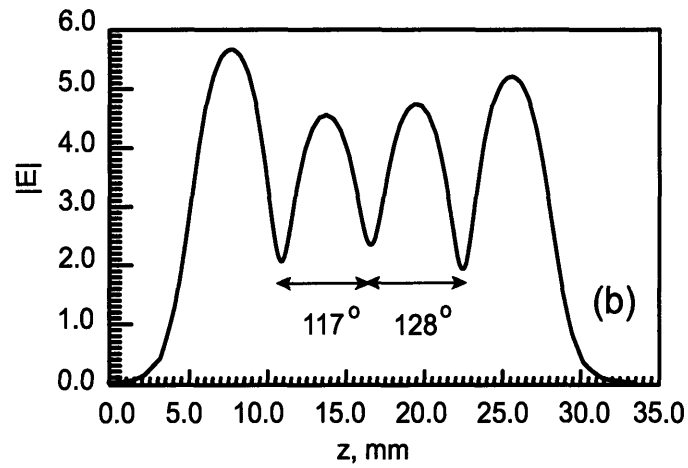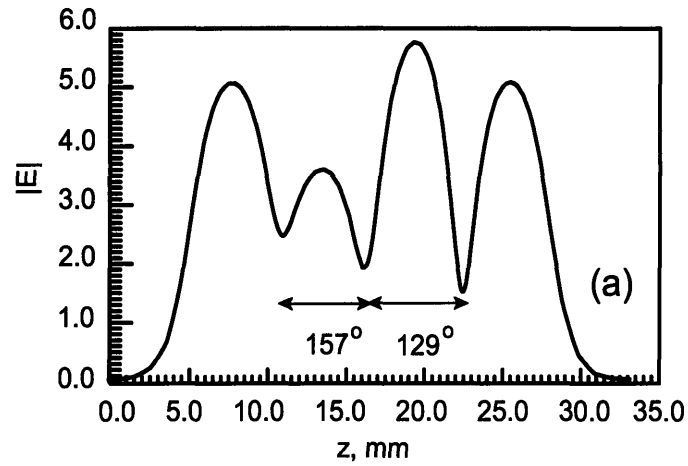
Figure C-3: The on-axis electric field profile and phase shift per TW cell for the Ng and Ko structure with a mismatched coupling cell ($b = 6.76$ mm) (a). The on-axis electric field profile and phase shift per TW cell for the Ng and Ko structure with the wall conductivity $\sigma = 2 \cdot 10^7 \, (\Omega \cdot m)^{-1}$ (b).
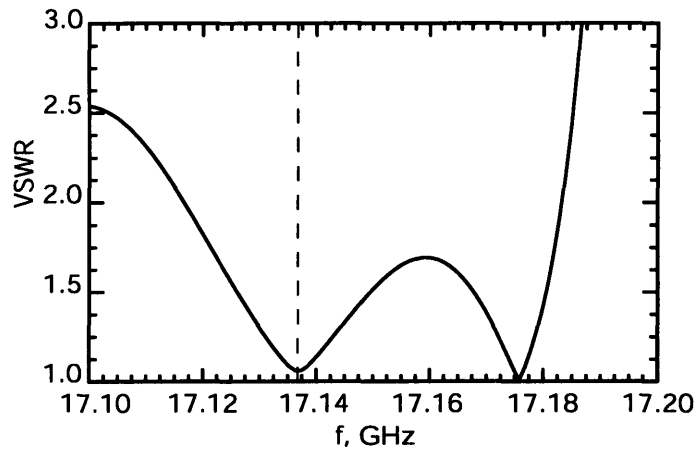
Figure C-4: The dependence of the VSWR in a lossless Ng and Ko structure on the frequency.

studied for a lossless structure (figure C-4). Similar dependencies were reported by Ng and Ko [31].

Table C.1: The dimension of a TW cell selected for the simulations and the dimensions of a coupler cell tuned with the Ng and Ko method.

TW cell radius	6.89 mm
TW cell length	5.83 mm
Iris radius	1.94 mm
Iris tip radius	0.48 mm
Coupling cell radius	6.75 mm
Coupling iris width	4.96 mm
Coupling iris height	0.48 mm

Appendix D

Pillbox coupler design with Kroll's method

A pillbox coupler was designed using Kroll's method, described in Chapter 5. The results agree perfectly with the coupler design using Ng and Ko method (see Appendix C), which means that both methods work. The modelled geometry is shown in figure D-1. Port was created at the cell #1 and the TM_{01} -mode of cylindrical waveguide was excited through the port. The matching load was placed at the end of the coupling waveguide. The symmetry plane was made an $H-$boundary. All other surfaces were made $E-$boundaries.

The port was excited at 17.137 GHz. The TM_{01} mode at cell #1 would couple with some reflection into a travelling wave $2\pi/3$ mode in the following cells. In cells #3 and #4 the Kroll's formulaes (5.6) and (5.7) are approximately valid. The reflection coefficient was calculated from the field profile in cells #3 and #4 using the equations (5.7). The parameters of the coupler cell, the coupler hole opening w and the coupler cell radius b, were then varied to minimize the reflection coefficient. A C++ subprogram was written for this optimization. The C++ subprogram followed the flow chart of figure 5-4. The optimization program ran for approximately 24 hours. The coupler was tuned to the low reflection of $|R| = 0.012$.

The magnitude of the electric field in a tuned structure is shown in color in figure D-2. Figure D-3 shows the on-axis distribution of the electric field magnitude.
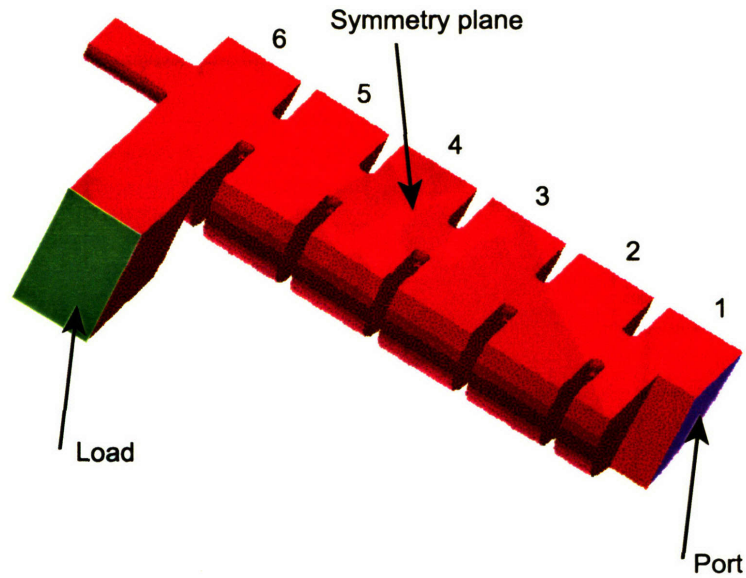
Figure D-1: The geometry for tuning a pillbox coupler with Kroll's method.

The field profile looks flat, which means that the coupler is tuned. The reflection coefficient, calculated using the equations (5.7) in different points of the structure on-axis is shown in figure D-4. The phase shift per cell, calculated using the equations (5.6) in different points of the structure on-axis is shown in figure D-5. The calculated reflection is almost independent of the point, where it is calculated. The phase shift per cell is very close to 120^0 in all the points in cells #3 and #4. This means that the solution converged well and the calculation is correct.

Tolerances, that is, the dependence of $|R|$ on w and b, were also calculated. This dependence is shown in figure D-6. It can be seen from the picture that the reflection from the coupler is much more sensitive to the radius of the coupler cell than to the size of the coupler hole.
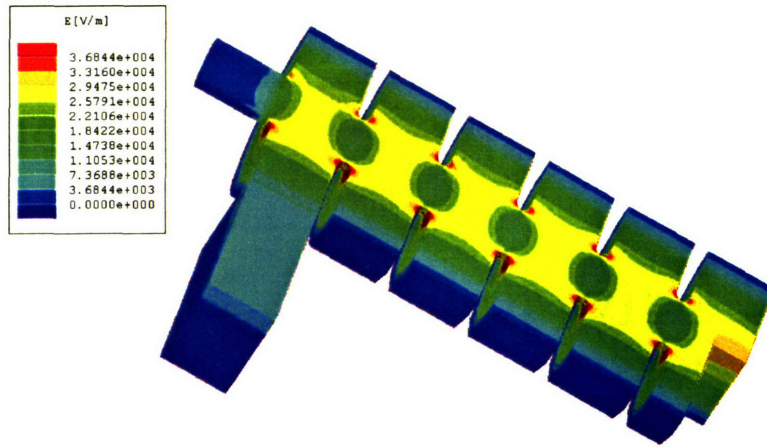
Figure D-2: The electric field magnitude in a TW structure with a tuned pillbox coupler.
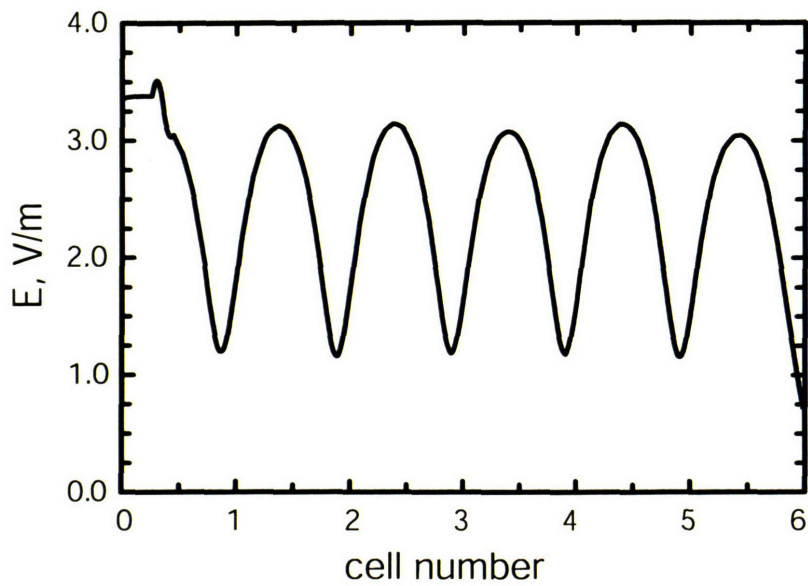

Figure D-3: The electric field distribution on-axis of a structure with a tuned pillbox coupler.
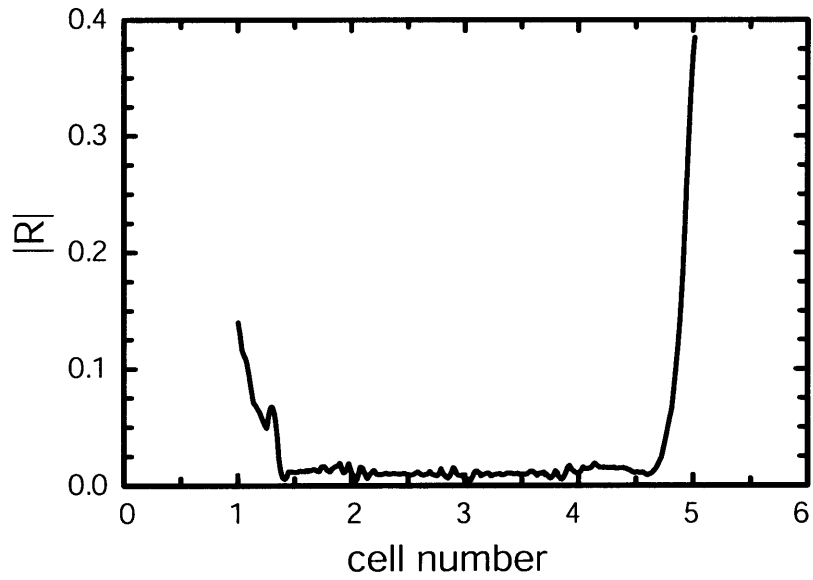
Figure D-4: The reflection coefficient calculated according to (5.7) in different points of the TW structure.
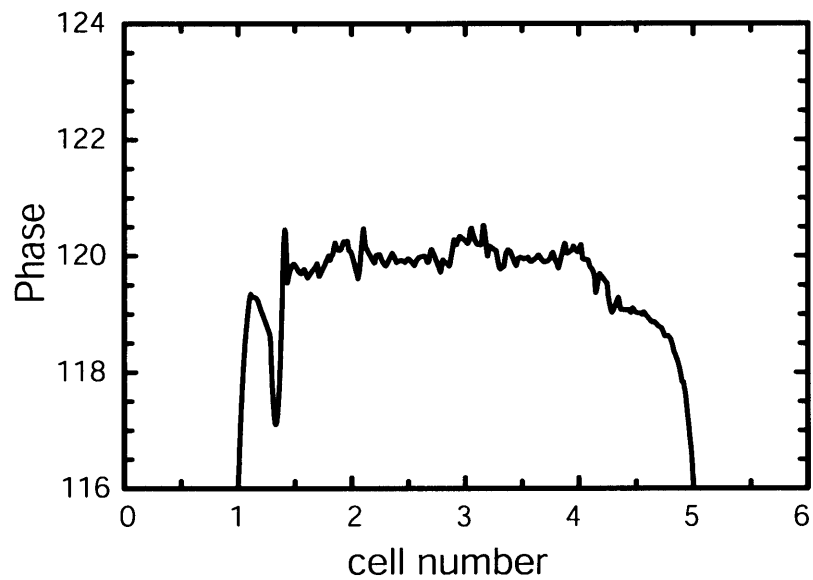

Figure D-5: The phase advance per cell calculated according to (5.6) in different points of the TW structure.
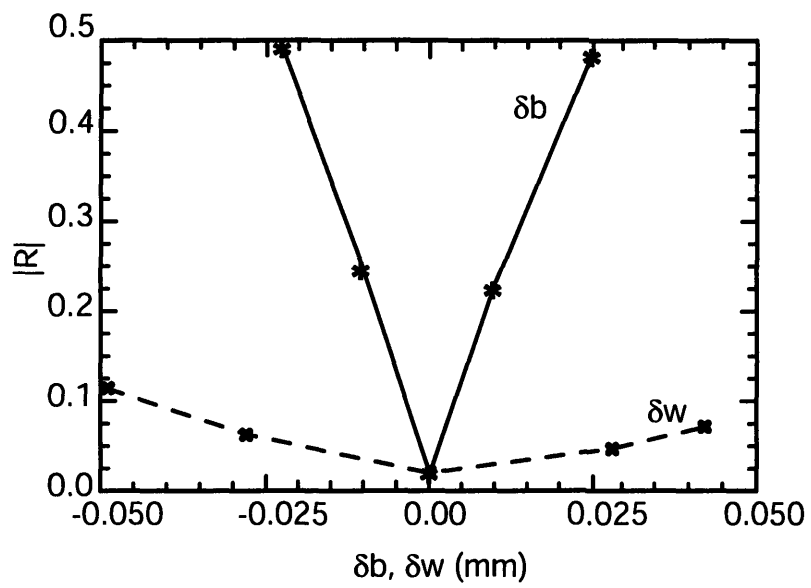
Figure D-6: Dependence of the reflection from a PBG coupler on the deviation of the coupler opening size w, and the coupling cell radius b from the optimized dimensions.

Bibliography

[1] E. Yablonovitch. *Phys. Rev. Lett.*, 58:2059, 1987.

[2] J.D. Joannopoulos, R.D. Meade, and J.N. Winn. *Photonic Crystals: Molding the Flow of Light.* Princeton Univ. Press, Princeton, 1995.

[3] M. Born and E. Wolf. *Principles of Optics.* Pergamon Press, Sixth edition, 1980.

[4] K. Bane and M. Sands. *SLAC-PUB-4441*, 1987.

[5] R.P. Borghi, A.L. Eldredge, G.A. Loew, and R.B. Neal. *in Advances in Microwaves*, volume 1. Academic Press, New York and London, 1966.

[6] D.L. Burke. *SLAC-R-526*, page 35, 1997.

[7] R.M. Jones, N.M. Kroll, R.H. Miller, R.D. Ruth, and J.W. Wang. *SLAC-PUB-7537*, 1997.

[8] C.M. Anderson and K.P Giapis. *Phys. Rev. Lett.*, 77:2949, 1996.

[9] H.-Y.-D. Yang. *IEEE Trans. MTT*, 44:2688, 1996.

[10] D.R. Smith, S. Schultz, N. Kroll, M. Sigalas, K.M. Ho, and C.M. Soukoulis. *Appl. Phys. Lett.*, 65:645, 1994.

[11] M.A. Shapiro, W.J. Brown, I. Mastovsky, J.R. Sirigiri, and R.J. Temkin. *Phys. Rev. Special Topics: AB*, 4:042001, 2001.

[12] J.R. Sirigiri, K.E. Kreischer, J. Machuzak, I. Mastovsky, M.A. Shapiro, and R.J. Temkin. *Phys. Rev. Lett.*, 86:5628, 2001.

[13] T. Suzuki and P.K.L. Yu. *Phys. Rev. B*, 57:2229, 1998.

[14] N.A. Nicorovici, R.C. McPhedran, and L.C. Botten. *Phys. Rev. E*, 52:1995, 1995.

[15] M. Qiu and S. He. *J. Appl. Phys*, 87:8268, 2000.

[16] S.G. Johnson and J.D. Joannopoulos. *Photonic Crystals: The Road from Theory to Practice.* Kluwer Academic Publishers, 2002.

[17] N. Kroll, D.R. Smith, and S. Schultz. *AIP Conference Proceedings*, 279:197, 1992.

[18] D. Li, N. Kroll, D.R. Smith, and S. Schultz. *AIP Conference Proceedings*, 398:528, 1997.

[19] D.R. Smith, D. Li, D.C. Vier, N. Kroll, and S. Schultz. *AIP Conference Proceedings*, 398:518, 1997.

[20] E.I. Smirnova, C. Chen, M.A. Shapiro, J.R. Sirigiri, and R.J. Temkin. *J. of Appl. Phys.*, 91(3):960, 2002.

[21] N.W. Ashcroft and N.D. Mermin. *Solid State Physics.* Jolt, Rinehart and Winston, New York, 1976.

[22] O. Madelung. *Introduction to Solid State Theory.* Springer, London, 1978.

[23] L.D. Landau, E.M. Lifshitz, and L.P. Pitaevskii. *Electrodynamics of Continuous Media.* Pergamon Press, Oxford, 1984.

[24] *Poisson Superfish.* Los Alamos Accelerator Code Group, Los Alamos, NM 87545, laacg1.lanl.gov.

[25] *High Frequency Structure Simulator.* Ansoft Corporation, Pittsburgh, PA 15219, www.hfss.com.

[26] K.L.F. Bane and Z. Li. *SLAC-PUB-8545*, 2000.

[27] Communication Power Industries, Inc., Palo Alto, CA 94303, www.cpii.com.

[28] J. Haimson, B. Mecklengurg, and B.G. Danly. *AIP Conference Proceedings*, 337:146, 1995.

[29] J. Haimson and B. Mecklengurg. *Proceedings of 1995 Particle Accelerator Conference*, 2:755, 1995.

[30] T.P. Wangler. *Principles of RF Linear Accelerators*, page 337. John Wiley and Sons Inc., New York, 1998.

[31] C.K. Ng and K. Ko. *SLAC-PUB-6086*, 1993.

[32] N.M. Kroll, C.K. Ng, and D.C. Vier. *SLAC-PUB-8614*, 2000.

[33] Custom Microwave, Inc., Longmont, CO 80501, www.custommicrowave.com.

[34] W.J. Brown. *Low Emittance Electron Beam Production and Characterization with a 17 GHz Photocathode RF Gun*, page 67. PhD Thesis, Massachusetts Institute of Technology, 2001.

[35] T.P. Wangler. *Principles of RF Linear Accelerators*, page 162. John Wiley and Sons Inc., New York, 1998.

[36] E. Westbrook. *SLAC-TN-63-103*, 1963.

[37] P.B. Wilson. *SLAC-PUB-7449*, 1997.

[38] T.S. Chu, F.V. Hartemann, B.G. Danly, and R.J. Temkin. *Phys. Rev. Lett.*, 72:2391, 1994.

[39] J. Haimson, B. Mecklenburg, and G Stowell. *Proceedings of the 2001 Particle Accelerator Conference*, 5:3948, 2001.

[40] S. Korbly, A.S. Kesar, M.A. Shapiro, and R.J. Temkin. *Proceedings of 2003 Particle Accelerator Conference*, page 2536, 2003.

[41] S.E. Korbly, A.S. Kesar, J.R. Sirigiri, and R.J. Temkin. *to appear in Phys. Rev. Lett.*, 2005.

[42] J. Haimson, B. Mecklengurg, G. Stowell, and B. Ishii. *AIP Conference Proceedings*, 647:810, 2002.

[43] T. Shintake, H. Matsumoto, N. Akasaka, M. Yoshida, C. Adolphsen, K. Jobe, D. McCormick, M. Ross, and T. Slaton. *Proceedings of 1999 Particle Accelerator Conference*, page 3411, 1999.

[44] I. Wilson, W. Wuensch, C. Achard, M. Dehler, E. Jensen, M. Luong, C. Adolphsen, M. Ross, T. Slaton, and D. McCormick. *SLAC-PUB-8941*, 2001.

[45] N. Baboi, R.M. Jones, J.W. Wang, G.B. Bowden, V.A. Dolgashev, J. Lewandowski, S.G. Tantawi, and P.B. Wilson. *SLAC-PUB-9472*, 2002.

[46] E.I. Smirnova, M.A. Shapiro, C. Chen, and R.J. Temkin. *AIP Conference Proceedings*, 647:383, 2002.

[47] R.F. Harrington. *Time-harmonic electromagnetic fields*, pages 381–386. McGraw-Hill Book Company Inc., New York, Toronto, London, 1961.

[48] J.C. Slater. *Microwave Electronics*, pages 112–131. D. Van Nostrand Company Inc., New York, Toronto, London, 1950.

[49] R.N. Ghose. *Microwave circuit theory and Analysis*, page 265. McGraw-Hill Book Company Inc., New York, Toronto, London, 1963.

[50] T.P. Wangler. *Principles of RF Linear Accelerators*, page 65. John Wiley and Sons Inc., New York, 1998.